Asymmetrical Operation of EHV Transmission Lines

Ansar Berdygozhin

Department of Electronic and Electrical Engineering
University of Strathclyde

This dissertation is submitted for the degree of
Doctor of Philosophy

University of Strathclyde July 2026

To my mother . . .

Declaration

Ansar Berdygozhin
July 2026

Acknowledgements

I would like to express my sincere gratitude to my supervisor, Dr David Campos-Gaona, for his continuous support, guidance, and encouragement throughout my PhD studies. He was always available to discuss my work, provided valuable comments and feedback, and guided me through the many challenges of doctoral research. I am especially grateful for his help in identifying the research direction of this thesis and for offering me the opportunity to work as a research assistant when my scholarship ended.

I am also grateful to Dr Abdou Sana, who responded promptly to my email and generously provided the simulation models from his PhD thesis.

My sincere thanks go to Professor Olimpo Anaya-Lara and Dr Adam Dyśko for their valuable comments, feedback, and academic guidance during my research. I would also like to thank Professor Graeme Burt for supporting my application to participate in the European Energy Research Alliance (EERA) Joint Programme on Smart Grids for PhD Candidates, which led to a Gold Award in Milan in March 2026.

I am grateful to Dr Hong Yue and Dr Reza Yazdanpanah for their willingness to discuss different ideas and for their support during my PhD.

Abstract

The increasing penetration of Renewable Energy Sources (RES) and Inverter-Based Resources (IBR) is changing the operational behaviour of modern power systems. As conventional synchronous generation is displaced, transmission networks are required to operate with reduced inertia, increased power-electronic interfacing, and greater sensitivity to major line outages. In this context, the complete disconnection of an Extra-High-Voltage (EHV) overhead transmission line following an asymmetrical fault may lead not only to the loss of load supply, but also to the disconnection of significant generation connected along the transmission corridor. Since single-phase and two-phase faults represent a large proportion of transmission-line faults, Asymmetric Operation (AO), in which a line remains in operation with one or two phase conductors open, may offer a means of maintaining partial power transfer during selected post-fault conditions.

This thesis presents a simulation-based investigation of different forms of AO in long EHV overhead transmission lines, with emphasis on electromagnetic modelling, converter-based sequence-current mitigation, and safety-related voltage assessment. First, a high-fidelity three-phase simulation model of a long overhead power transmission line is developed. The model explicitly represents electromagnetic coupling between conductors, ground wires, tower structures, and earth return paths, allowing zero-sequence current distribution and transient behaviour during AO to be studied more accurately than with conventional simplified π-section representations.

Second, a converter-based support strategy is developed using E-STATCOMs located at the line extremities. A filterless two-degree-of-freedom internal-model-control (2DF–IMC) approach is adapted for the detection and suppression of negative- and zero-sequence current components. The proposed control structure enables rapid sequence-current mitigation without relying on resonant filters or narrow-band signal-processing stages, while preserving the nominal positive-sequence operation of the converter-interfaced devices.

The proposed modelling and control framework is evaluated on a representative 500kV, 300km overhead transmission line under one-phase and two-phase asymmetric operating conditions. Simulation results indicate that, for the studied system and scenarios, AO can maintain controlled power transfer after selected asymmetrical faults when supported by appropriate converter-based sequence-current compensation. The results also show that negative- and zero-sequence currents can be substantially reduced, voltage profiles at the line terminals can remain within acceptable limits, and tower-tip voltages can satisfy the voltage-based safety criterion considered in this work. Cases with no pre-fault power restoration, partial restoration, and full restoration are also examined to assess the operational implications of different AO support levels.

The findings strongly suggest that AO may provide a potential resilience-enhancing operating option for future converter-dominated transmission systems. However, the study also shows that AO is not a universally applicable solution and would require additional converter capacity, control functionality, protection coordination, operational procedures, and techno-economic justification. Therefore, the contribution of this thesis is not to establish immediate practical deployment of AO, but to provide a physically grounded simulation framework and control methodology for assessing its technical potential.

Contents

List of Figures

List of Tables

Nomenclature

Roman Symbols

A_{bat} Exponential voltage

A, B, C, D Power-line parameters

B_{bat} Exponential capacity

C Capacitance

C_d^+, C_q^+, C_d^-, C_q^- Steady-state outputs of the positive- and negative-sequence d- and q-axis integral controllers

C_{dq}^+, C_{dq}^- Steady-state outputs of the combined positive- and negative-sequence dq-axis integral controllers

$\mathbf{C}$ Power line capacitance matrix

D_b Bundle diameter

D_{in} Distance between conductor i and conductor n

D_{out} Outer diameter of the power-line conductor

E_0 Constant battery voltage

E_z Electric field component (symmetrical with respect to x)

$F(\mu)$ Kernel function in Carson's integral

$F(s)$ Controller transfer function

G Constant, $G = 4.885 \times 10^{-4}$ Ω/km

GMR Geometric mean radius of conductor i

$G(s)$ Plant in s domain

$\mathbf{I}$	Unity matrix
i	Current (A)
$\tilde{i}$	Low-frequency current dynamics
K	Polarisation constant or polarisation resistance
$K(s)$	Auxiliary transfer function (used to shorten the expression)
$\mathbf{L}$	Power line inductance matrix
$\mathbf{l}$	Power line inductance vector
L_{Th}	Thévenin equivalent inductance of the 500 kV grid
M	Auxiliary coefficient (used to shorten the expression)
m	Modulation signal
$M'(s)$	Model of the improved transfer function of the plant
$M(s)$	Improved transfer function of the plant
N	Number of times the line of flux surrounds the conductor
N_c	Number of conductors in the power-line bundle
P	Active power
p	Probability
q	Extracted capacity
q_{max}	Maximum battery capacity
RD	Radius of conductor i
r_{dc}	DC resistance of the power-line conductor
$\mathbf{R}$	Power line resistance matrix
$\mathbf{r}$	Power line resistance vector
$R(s)$	Inner feedback loop
r_{Th}	Thévenin equivalent resistance of the 500 kV grid

S Distance between conductor i and image conductor j

S_1, S_2, S_3, S_4 Circuit breakers

T Thickness of the power-line conductor

$\mathbf{u}$ Output of a controller in vector form

V_{dc} VSC dc-link voltage

X_p Generic phase phasor of phase p, representing either voltage or current

x, y, z Coordinates

Y Admittance

Z Impedance

Z_c Power line surge impedance

$\mathbf{Z}$ Power line impedance matrix

Greek Symbols

α_{bw} Closed-loop bandwidth

α_{cr} Earth parameter in Carson's equation

β Auxiliary coefficient (used to shorten the expression)

δ Auxiliary coefficient (used to shorten the expression)

δ_v Grid voltage angle

η Auxiliary coefficient (used to shorten the expression)

γ Auxiliary coefficient (used to shorten the expression)

γ_{pr} Electromagnetic wave propagation constant

λ Flux linkage

μ_{cr} Integration variable

μ_r Relative permeability

ω Grid angular speed

Φ Magnetic flux

ρ Earth resistivity

σ Auxiliary coefficient (used to shorten the expression)

Superscripts

$*$ Control reference signal

$+$ Positive-sequence component or associated controller parameter

$-$ Negative-sequence component or associated controller parameter

o Zero-sequence component or associated controller parameter

Subscripts

$abc \rightarrow dq^-$ Park transformation from abc to the negative-sequence dq frame

$abc \rightarrow dq^+$ Park transformation from abc to the positive-sequence dq frame

$dq^+ \rightarrow abc$ Inverse Park transformation from the positive-sequence dq frame to abc

$dq^- \rightarrow abc$ Inverse Park transformation from the negative-sequence dq frame to abc

dq^+, d^+, q^+ Positive-sequence dq reference frame and its d- and q-axis components

dq^-, d^-, q^- Negative-sequence dq reference frame and its d- and q-axis components

1 Sending end

2 Receiving end

$2DFIMC$ Two-degrees-of-freedom internal model controller

ac Sinusoidal signal

$asym$ Asymmetrical

$calc$ Calculated value

dc Constant signal

eq Equivalent

f Filter, e.g., v_{fa}: phase-a voltage at the filter

g Grid wire

$g1, g2, \ldots, gn$ Ground wire(s)

gr Ground

i, j Index variables (e.g., i-th element, j-th column of a matrix)

m Maximum value

$meas$ Measured value

p Phase

PI Proportional integral controller

$posf$ Post-fault

$pref$ Pre-fault

r Receiving end

s Sending end

sh Shunt

sym Symmetrical

t Terminal

tw Tower

Other Symbols

a 120° rotating operator

e Base of the natural logarithm, $\simeq 2.718\ldots$

$\int_0^\infty$ Definite integral from 0 to ∞

j Unit imaginary number, $\sqrt{-1}$

s Laplace operator

Acronyms / Abbreviations

$3L4W$ three-leg four-wire

AO asymmetric operation

APF active power filter

$BESS$ battery energy storage system

DFT discrete Fourier transform

DG distributed generation

$DSSC$ distributed static series compensator

$E\text{-}STATCOM$ static synchronous compensator equipped with energy storage

EHV extra high voltage

EMT electromagnetic transient

$FACTS$ flexible AC transmission systems

FFR fast frequency response

FFT fast Fourier transform

GC grid code

GI generalised integrator

IBR inverter-based resources

IMC internal model control

IPC interphase power controller

LPF low-pass filter

MMC modular multilevel converter

$MSOGI$ multiple second-order generalized integrators

MV medium voltage

NPS national power system

$OPAO$ one-phase asymmetric operation

OPL overhead power line

PCC point of common coupling

PI proportional integral

PLL phase-locked loop

PP power plant

SC short circuit

$SDFT$ sliding discrete Fourier transform

SIL surge impedance loading

SO system operator

$SOGI$ second-order generalized integrator

$SPAR$ single pole automatic reclosure

SRF synchronous reference frame

SSI sinusoidal signal integrator

$STATCOM$ static synchronous compensator

$SWER$ single-wire earth return

THD total harmonic distortion

$TOPL$ transmission overhead power line

$TPAO$ two-phase asymmetric operation

TWE two wires earth

UHV ultra high voltage

VSC voltage source converter

Chapter 1

Introduction

The global shift from conventional thermal generation to Renewable Energy Sources (RES) is transforming the structure and operation of power systems worldwide. According to projections by the International Energy Agency (IEA), global electricity generation from RES is expected to increase by almost 90% by 2030 compared with 2023 [6]. At the same time, overall electricity demand is predicted to grow substantially, driven in part by the rapid expansion of data centres and large-scale artificial intelligence computational facilities.

The increasing penetration of RES introduces new operational requirements for transmission networks. Lines that were originally designed solely to supply load are now frequently connected to large wind and solar power plants, with substantial amounts of generation injected along their length. Consequently, the tripping of a single transmission line may disconnect both demand and generation, thereby heightening operational challenges and security-of-supply risks. At the same time, the displacement of conventional power plants equipped with robust synchronous generators reduces the available system inertia.

Historically, transmission systems were dominated by synchronous generators with large rotating masses, which inherently provided substantial inertia and enabled the network to withstand transmission-line outages with relatively contained dynamic consequences. The situation is markedly different today. As synchronous generation continues to decline, the overall system inertia is shrinking, and networks that were once considered highly robust are now operating much closer to their stability limits. In this low-inertia environment, the loss of a major power corridor can no longer be treated as a disturbance that the system will simply ride through; it requires active mitigation to avoid severe system-wide impacts.

Most newly installed RES take the form of Inverter-Based Resources (IBR), typically interfaced through Voltage Source Converters (VSC). Since the behaviour of VSCs is largely determined by their control algorithms, these units are increasingly expected to provide a broad range of ancillary services previously supplied by synchronous generators. Their high degree of controllability enables both conventional grid-support functions and new advanced services. Correspondingly, the reliance on power-electronic equipment and Flexible AC Transmission Systems (FACTS) is expected to grow, as these devices help maintain stability and voltage support in systems characterised by reduced mechanical inertia and faster dynamics [7].

1.1 The TOPL AO Layout Problem

Given that single-phase-to-ground, two-phase-to-ground, and phase-to-phase faults constitute the majority of fault events on Extra-High Voltage (EHV) Transmission Overhead Power Lines (TOPL), the Asymmetric Operation (AO) of power lines presents a potentially valuable means of maintaining continuity of supply. Early research in this area—most notably by A. Sana—explored the feasibility of AO and demonstrated its theoretical applicability [2, 8–10]. However, the modelling approach adopted in these pioneering studies was based on a simplified π-section transmission-line representation, which introduces several limitations.

Firstly, this model does not account for electromagnetic couplings between phases, as each phase is represented by an independent π-circuit. Overall, the suitability of this power-line model for AO studies is therefore questionable. In addition, it cannot provide a detailed analysis of zero-sequence current distribution paths. In practice, zero-sequence currents propagate through all available return routes, including shield/ground wires, tower structures, and ground. Secondly, the simplified model is unable to capture electromagnetic transients, which are essential for evaluating AO behaviour under realistic operating conditions. Moreover, the simulated line in Sana's work was directly connected to ideal voltage sources at both terminals, effectively guaranteeing stable current injection and thus not fully reflecting practical grid conditions [10].

Despite these limitations, the research provided important early insights and showed that AO could, in principle, be realised not only with power-electronic devices but also with passive filters. These findings highlight the need for more comprehensive line models capable of reflecting the true electromagnetic characteristics of long EHV transmission lines under AO, as well as a clear assessment of the implications of allowing the flow of zero-sequence currents in terms of capacity and safety to do so.

In the specific case of power electronics control for AO, there is the need for fast detection and compensation of sequence components, specially in the case where a fast transition is required from symmetrical to AO without power flow interruption.

This calls for the development of accurate, fast and robust power electronic control systems.

Given all of this, the research questions of this investigation are formulated as follows:

After considering in rigorous manner the electromagnetic coupling of transmission lines, is the asymmetric operation of an EHV long transmission power line realisable with one or two phases open when using two IBRs at the extremities?

What are the implications of allowing zero sequence flow in an power line corridor and what is the safest way to do so?

Is it possible to quickly detect and to control the current sequence components of an EHV long transmission line using a control system that does not conflict the nominal positive-sequence operation of IBRs?

To address the above questions, the research objectives of this thesis are formulated as follows:

- Develop an EHV overhead transmission-line model capable of accurately representing zero-sequence current distribution, the influence of opened phase(s), and electromagnetic transients.

- Design a fast and robust linear control method to enable the practical realisation of AO, and determine the best way to implement the resulting controllers in an EHV system using E-STATCOMs.

- Investigate whether the fast and robust filterless Synchronous Reference Frame (SRF)–based harmonic detection and suppression method first proposed by Campos-Gaona *et al.* [11] can be effectively adapted for current sequence components extraction and control.

- Demonstration of AO with one and two open phases, both without and with (partial or full) pre-fault power restoration using IBRs support. The demonstration must be carried out using realistic transmission power line representation and avoiding the use of the ideal power sources used in previous AO research work.

1.2 Contributions to the State of the Art

This thesis makes the following principal contributions:

- **Development of a comprehensive EMT simulation model of an EHV transmission line.**
  A detailed electromagnetic-transients-compatible simulation model of an EHV overhead transmission line was developed for the analysis of AO. The model represents zero-sequence current distribution through the relevant physical paths, including shield wires, tower structures, and ground, and accounts for the effects of opened phase(s) and electromagnetic coupling between healthy and disconnected conductors. In contrast to the simplified π-section representations commonly used in previous AO studies, the developed simulation model provides a more realistic basis for assessing AO behaviour under practical operating conditions.

- **Adaptation and design of advanced filterless controllers for AO.**
  An existing filterless SRF – based harmonic detection and suppression method was adapted and extended to enable fast extraction and mitigation of current sequence components. Building on this adapted method, novel fast and robust filterless controllers were developed to realise both Two-Phase Asymmetric Operation (TPAO) and One-Phase Asymmetric Operation (OPAO). The controllers suppress undesired sequence components without relying on low-pass filters, thereby significantly improving dynamic response and control robustness. Their performance was evaluated using a transmission line connected to the grid through a non-zero Thevenin impedance, providing a realistic representation of practical grid conditions. Given their linear characteristics and strong disturbance-rejection capabilities, these novel controllers can be integrated into the positive-sequence control methodologies of functional IBRs without affecting their positive-sequence operation.

- **Simulation-based assessment of AO with and without pre-fault power restoration, including voltage-based safety considerations.**
  A simulation-based AO assessment framework was developed to evaluate operation with one or two phases open, including scenarios with no power restoration, partial pre-fault restoration, and full pre-fault restoration using IBR support. The assessment considered voltage levels along the line as the main safety-related criterion. The simulation results indicate that, for the representative 500 kV, 300 km overhead transmission line studied, AO can be achieved in sim-

ulation while preserving operational feasibility and satisfying the voltage-based safety criterion considered in this work.

1.3 Structure of the Thesis

This thesis is organised into six chapters, followed by three appendices. The structure is designed to progress from the motivation and state of the art, through the development of the required models and controllers, to the demonstration and assessment of asymmetric operation (AO) of an extra-high-voltage (EHV) overhead power line under realistic conditions. The main chapters are structured as follows:

- **Chapter 2** reviews asymmetric operation of power networks. It defines symmetry in polyphase systems, outlines prerequisites for AO at HV/EHV/UHV levels, surveys practically realised medium-voltage asymmetric systems, and critically synthesises the literature on AO of transmission lines, including prior foundational work. The chapter also reviews sequence-component detection and control methods relevant to AO.

- **Chapter 3** develops the modelling and control framework for the converter-interfaced support device employed in this thesis. It presents the E-STATCOM (VSC-based) model, introduces the two-degrees-of-freedom internal model control (2DF–IMC) concept, and details the sequence-component detection and the design of positive-, negative-, and zero-sequence current controllers, including filterless operation and performance considerations.

- **Chapter 4** develops a three-phase transmission-line model suitable for AO studies. It establishes the theoretical basis for modelling electromagnetic coupling, zero-sequence return paths, and the influence of opened phase conductors. The proposed full (EMT-compatible) line model is compared against π-section alternatives in both steady-state and electromagnetic transient studies, and dedicated test cases are used to quantify the impact of model fidelity on AO-relevant responses.

- **Chapter 5** demonstrates asymmetric operation of a representative full EHV transmission line model. Two-phase AO and one-phase AO are assessed under scenarios without pre-fault power-flow restoration and with partial or full pre-fault restoration using inverter-based support at the line extremities. The chapter further evaluates operational and safety aspects of AO, including voltage stresses along the corridor.

- **Chapter 6** concludes the thesis by summarising how the research questions are answered, highlighting the practical significance and limitations of the proposed modelling and control framework, and outlining recommendations and directions for future work.

1.4 List of Publications

Journal papers

1. A. Berdygozhin and D. Campos-Gaona. Asymmetric operation of power networks, state of the art, challenges, and opportunities. Energies, 17(20), 2024. ISSN 1996-1073. doi: 10.3390/en17205021.

Conference papers

2. A. Berdygozhin, D. Akhmetbayev, and D. Campos-Gaona. Modelling stability improvement in kazakhstan's power system by using battery energy storage. 2021 56th International Universities Power Engineering Conference: Powering Net Zero Emissions, UPEC 2021 - Proceedings, 2021. doi: 10.1109/UPEC50034.2021.9548180. Conference name: 56th International Universities Power Engineering Conference, UPEC 2021.
3. A. Berdygozhin, B. Pepper, and D. Campos-Gaona. Asymmetric operation of power lines by using e-statcom and internal model controllers. In 2024 IEEE 15th International Symposium on Power Electronics for Distributed Generation Systems (PEDG), pages 1–6, 2024. doi: 10.1109/PEDG61800.2024.10667369.
4. A. Berdygozhin, D. Akhmetbayev, G. Ansabekova, and D. Campos-Gaona. Novel approach for asymmetrical operation of transmission lines using enhanced line model. 2025 IEEE Workshop on Electronic Power Grid (eGrid 2025), 2025. Poster presented at IEEE eGrid 2025 Workshop.

Other papers during PhD study

5. D. S. Akhmetbayev, A. R. Dzhandigulov, and A. Berdygozhin. Topological algorithm to form power of compensating devices of distribution networks. E3S Web of Conferences, 216, 2020. doi: 10.1051/e3sconf/202021601088. Conference name: 2020 Rudenko International Conference on Methodological Problems in Reliability Study of Large Energy Systems, RSES 2020.

Chapter 2

Asymmetric Operation of Power Networks

2.1 Introduction

The origin of AC power transmission can be traced back to 1886, when William Stanley demonstrated an electrical system with a loss of approximately 2%, operating at 500V in Great Barrington, Massachusetts, successfully transmitting power over a distance of 4,000ft [12]. This installation utilised single-phase transmission and was, by its nature, asymmetrical.

In 1895, Westinghouse Electric Corporation initiated the construction of 90°-shifted two-phase generators for the Niagara Falls power plant. The generated power was transmitted to Buffalo, NY, via an 11kV, 25-mile transmission line operating at 25Hz [13]. By this period, the symmetrical three-phase system had already been introduced and showcased at the 1891 Frankfurt International Electrotechnical Exhibition. Nevertheless, the owners of the Niagara Falls scheme initially favoured the two-phase system, as the comparative advantages between two-phase and three-phase technologies were not yet fully established. It was soon recognised that the three-phase system offered superior efficiency for AC machinery and power transmission, leading to its widespread adoption — a trend that continues today. However, a number of Medium-Voltage (MV) electric systems still operate in AO mode, and therefore merit a dedicated review, which is provided in this chapter.

Accordingly, this chapter outlines the general definition of symmetry, identifies the prerequisites for AO in power lines, and reviews the main publications and research contributions dedicated to AO of power transmission lines. Since AO operation relies on the suppression of current sequence components, methods for selective harmonic detection and associated control strategies are also examined, with particular attention given to harmonic convergence time, memory requirements, and computational burden.

2.2 Symmetry in electrical systems

Since the asymmetrical operation of power transmission lines deliberately departs from conventional symmetrical operating conditions, the concept of a symmetrical polyphase system must first be revisited. In theory, the phasors of a balanced symmetrical polyphase system are mathematically described as roots of unity on the complex plane. The formula for calculating their exact coordinates can be derived from the following expression:

$$1 = \mathbf{z}_k^n, \quad \mathbf{z} \in \mathbb{C}, \quad n \in \mathbb{N}, \quad k = 0, 1, ..., n-1, \tag{2.1}$$

which by De Moivre's formula becomes [14]

$$\mathbf{z}_k = \cos(\frac{2\pi k}{n}) - j\sin(\frac{2\pi k}{n}). \tag{2.2}$$

Here, the sign of the imaginary part is changed from positive to negative in comparison with the original mathematical form. This modification is introduced to follow the adopted electrical engineering convention for the phase sequence. The complex number $\mathbf{z}$ is then replaced by X, where X denotes a generic phasor quantity that may represent either a voltage or a current. To conform with electrical engineering notation, the numerical indices of $\mathbf{z}$ are also replaced by Latin phase labels, such as a, b, c, and so on. Therefore, Equation 2.2 can be rewritten as Equation 2.3. Thus, the first phasor, X_a, is always aligned with the positive real axis, while the remaining phasors are equally distributed around the unit circle according to Equation 2.3.

$$X_p = \cos\left(\frac{2\pi k}{n}\right) - j\sin\left(\frac{2\pi k}{n}\right), \tag{2.3}$$

where $p \in \{a, b, c, \ldots\}$ denotes the corresponding phase label, and each label p is associated with a numerical index $k = 0, 1, \ldots, n-1$. The parameters n and k are defined in Equation 2.1. Equation 2.3 defines a symmetrical phasor vector space with unit length. Using this equation, the corresponding phase phasors are obtained as points on the unit circle. For the three-phase balanced system, the phase phasors

X_a, X_b, and X_c have the following complex coordinates:

$$X_a = 1 + j0,$$
$$X_b = -\frac{1}{2} - j\frac{\sqrt{3}}{2},$$
$$X_c = -\frac{1}{2} + j\frac{\sqrt{3}}{2}.$$

Similarly, for the five-phase balanced system, the phase phasors X_a, X_b, X_c, X_d, and X_e have the following complex coordinates:

$$X_a = 1 + j0,$$
$$X_b = \frac{\sqrt{5}-1}{4} - j\frac{\sqrt{10+2\sqrt{5}}}{4},$$
$$X_c = -\frac{\sqrt{5}+1}{4} - j\frac{\sqrt{10-2\sqrt{5}}}{4},$$
$$X_d = -\frac{\sqrt{5}+1}{4} + j\frac{\sqrt{10-2\sqrt{5}}}{4},$$
$$X_e = \frac{\sqrt{5}-1}{4} + j\frac{\sqrt{10+2\sqrt{5}}}{4}.$$

Figure 2.1 illustrates the corresponding balanced symmetrical polyphase systems with three and five phasors on the complex plane.

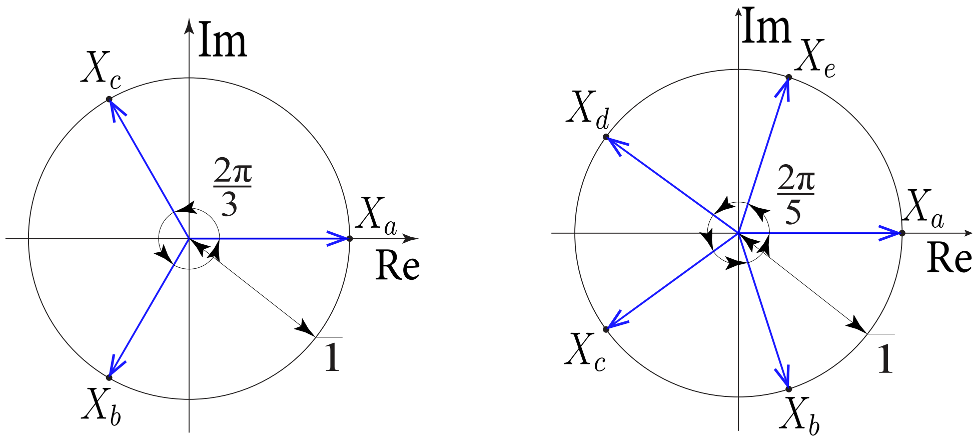

(a) Roots of unity for 3 phasors ($n = 3$).

(b) Roots of unity for 5 phasors ($n = 5$).

Figure 2.1 Balanced symmetrical polyphase systems' (unity length) phasors representation on the complex plane.

When the phasors are not equally spaced on the complex plane, or when their magnitudes are not equal, negative- and zero-sequence components may appear, and the positive-sequence component may change. For a three-phase system, the sequence components can be obtained as

$$\begin{bmatrix} X^{+} \\ X^{-} \\ X^{\mathrm{o}} \end{bmatrix} = \frac{1}{3} \begin{bmatrix} 1 & a & a^2 \\ 1 & a^2 & a \\ 1 & 1 & 1 \end{bmatrix} \begin{bmatrix} X_a \\ X_b \\ X_c \end{bmatrix}.$$

Thus, the general criteria for balanced symmetrical operation, expressed in terms of sequence components, require the negative- and zero-sequence components of both current and voltage to be equal to zero:

$$I^{-} = 0, \qquad I^{\mathrm{o}} = 0, \tag{2.4}$$

and

$$V^{-} = 0, \qquad V^{\mathrm{o}} = 0. \tag{2.5}$$

2.3 Practically realised medium-voltage asymmetric systems

Before considering AO of EHV OPLs, it is useful to review MV (2.4–69kV) electrical systems that inherently operate in an asymmetrical manner. This is relevant from two perspectives: (i) several MV systems with asymmetric operation already exist, and (ii) their long-term practical reliability provides confidence in AO concepts.

From a practical standpoint, if an AC transmission or distribution system requires a dedicated return conductor, or if the return current flows through the ground, such a configuration may be viewed as an asymmetric system. One of the major advantages of a symmetrical, balanced poly-phase system is the absence of return current, which eliminates the need for a separate return path. Nevertheless, several modern MV systems intrinsically operate in an asymmetrical fashion.

A well-known example is found in railway electrification, where electric locomotives draw power from overhead single-phase supply lines, with the return current flowing through the steel rails. Both AC and DC systems exist, with AC systems commonly operated at voltage levels such as 15kV/16.7Hz and 25kV/50Hz. Among these, the

25kV system is the most widespread, representing more than 50% of all electric traction networks worldwide [15]. Figure 2.2 schematically illustrates the power supply arrangement for an electric locomotive.

The global adoption of the 25kV system is attributed to its favourable compromise between equipment insulation requirements and transmission efficiency. While higher voltages can further reduce substation count and resistive losses (I^2R), such increases are constrained by insulation coordination and required clearances.

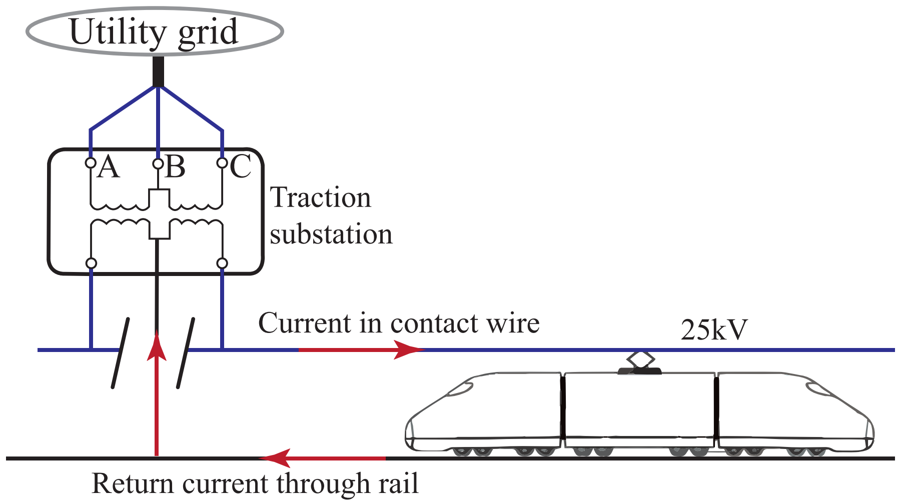

Figure 2.2 Electric locomotive powering schematic (adapted from [1]).

Another example of an inherently asymmetric system is the Single-Wire Earth Return (SWER) configuration, used extensively in rural distribution networks with sparse loads in countries such as New Zealand, Australia, several African nations, and parts of the USA (e.g., Alaska) [16]. First introduced in New Zealand in the 1920s, SWER systems expanded rapidly, with the combined length in New Zealand and Australia now exceeding 200,000km [17]. Their economic justification arises from the use of a single conductor, lightweight support structures, and rapid construction, all reducing capital expenditure.

However, safety considerations restrict the return current to 25A at 19.1kV, corresponding to a power rating of approximately 480kVA. In addition, the earth resistivity along the line must not exceed 1000Ωm, as higher values significantly reduce SWER efficiency. Other disadvantages include increased voltage drop and stronger electromagnetic interference with telecommunication lines compared to conventional three-phase distribution systems [17, 18].

Figure 2.3 shows a general SWER connection scheme. A key component is the isolating transformer, which steps down the voltage from a conventional three-phase MV network while providing galvanic isolation. Additional devices provide protection

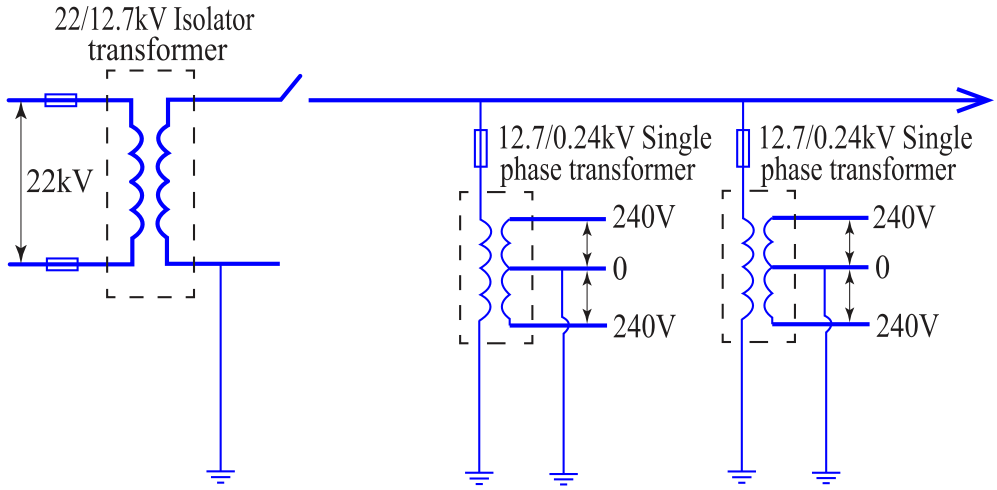

Figure 2.3 Typical SWER powering configuration.

and ensure a reliable earth return path. Notably, the grounding of the HV transformer must be separated from that of the LV transformer to avoid an unintended electrical connection between HV and LV systems.

Between the 1930s and 1950s, the USSR widely employed "Two-Wire Earth" (TWE) systems in rural three-phase MV distribution networks (6–10 kV) with isolated neutrals. Their main advantage was the reduction in conductor material. Figure 2.4 illustrates a typical TWE arrangement, in which the ground serves as the conductor for one phase and carries the corresponding phase current.

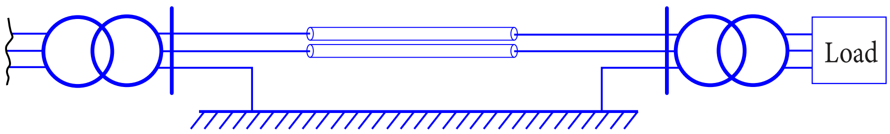

Figure 2.4 Typical "two-wire earth" (TWE) configuration.

Analysis in [19] shows acceptable current asymmetry (approximately 15%) for loaded TWE lines. However, unloaded 35kV lines can experience very high asymmetry (up to 150%) due to the Ferranti effect, leading to harmonic distortion and interference with communication lines. Consequently, [19] concluded that TWE should only be used at lower voltage levels (6–10kV).

More recently, [20] reported that TWE systems were abandoned primarily due to high grounding impedance at distribution substations (typically 4–5Ω at the time), which was unregulated. Modern standards (Regulations for Electrical Installation, Russia) now require grounding impedances below 0.5Ω, making TWE potentially viable again for 6–35kV distribution lines. Current asymmetry can also be reduced using filtering capacitors at the load, and earth current can be decreased when two parallel TWE lines are operated.

A further example of AO of a power linen arises when a phase is lost in a three-phase distribution system, or when the objective is to minimise investment in MV networks with isolated neutrals. In such cases, the transformer windings at both ends may be reconfigured into an open-Delta connection, as illustrated in Figure 2.5. This arrangement requires only two transformers connected in Delta, yet still provides symmetrical voltages, albeit with reduced power-transfer capability (approximately 57.8% of the original rating). In addition, the configuration inherently prevents the appearance of negative- and zero-sequence components, removing the need for supplementary compensating equipment. Such configurations have been documented since the early 20th century, when two-phase distribution systems were in operation [21, 22].

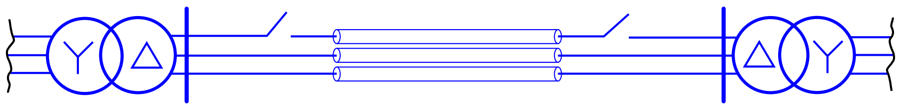

Figure 2.5 Power-line AO after a short circuit supported by Delta-connected transformers at both extremities.

In terms of applicability to HV/EHV power lines, the open-Delta configuration, despite its advantages, is not suitable for such systems for two main reasons: (i) HV/EHV transmission lines typically employ Y-connected transformers at both ends to enable protection relays to detect single-phase-to-ground faults via the neutral, (ii) Delta windings require higher insulation levels because the phase-to-phase voltage is greater than the phase-to-ground voltage.

Figure 2.6 summarises the key characteristics of different AO system types across MV and HV/EHV voltage levels. It distinguishes between MV systems that are currently in use, TWE systems that have been discontinued, and AO concepts for HV/EHV networks that are still under theoretical development.

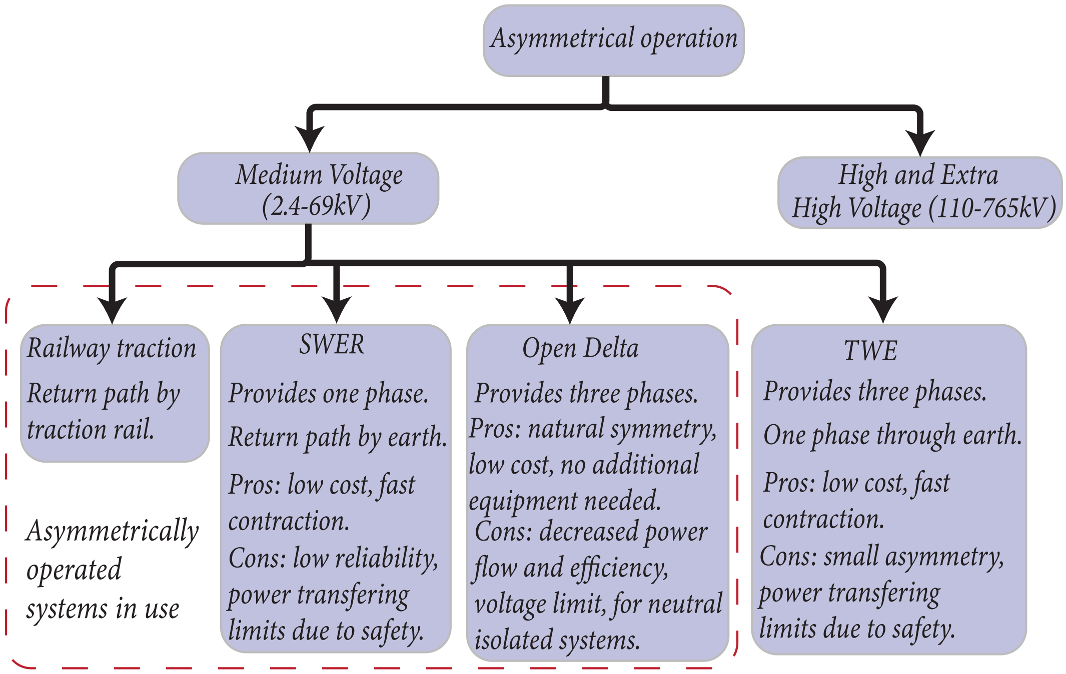

Figure 2.6 Summary of AO system types across voltage levels.

2.4 Prerequisites for AO of HV/EHV/UHV transmission lines

For a transmission line to remain symmetrical and balanced, the conditions expressed in (2.4) and (2.5) must be simultaneously satisfied at both terminals. Although these criteria apply to single- and multi-phase configurations, a single-phase system is inherently asymmetrical. In two-phase arrangements, symmetry is achieved only when the phase displacement between the two voltage phasors equals 180°. Since the phase-to-phase voltage in such a configuration is the phasor difference between the two phase voltages, a perfectly symmetrical two-phase system produces a phase-to-phase voltage equal to twice the individual phase magnitude. For a two-phase overhead power line, this higher conductor-to-conductor voltage directly increases the required electrical clearance and insulation level between the phase conductors. Consequently, two-phase balanced power transmission is generally impractical due to the substantially increased insulation demands.

If at least one of the left-hand-side terms in (2.4) or (2.5) deviates from zero, the system becomes unbalanced, and additional performance and power-quality issues may arise, particularly at the point of common coupling (PCC) of generation units and loads. However, the analysis of these unbalance-related performance and power-quality issues falls outside the scope of this thesis, as they are not typically critical at

EHV level and above. Furthermore, in the seminal AO studies [2, 9, 23, 10, 24], the voltages at both extremities of the transmission line are assumed to be constant and symmetrically balanced. This assumption is well justified for most high-voltage (HV; 110–230 kV) and, in particular, extra-/ultra-high-voltage (EHV/UHV; 230 kV and above) transmission systems, where busbar voltages are maintained close to nominal values by shunt reactors, on-load tap-changing transformers, STATCOMs, and other voltage-control equipment. Additionally, these node voltages are primarily dictated by prevailing power-flow conditions. Therefore, the case studies presented in this thesis also assume constant symmetrical voltages at the transmission-line extremities, reflecting typical operating conditions in EHV networks.

2.5 Review of A. Sana's contributions to power-line AO

Given that A.-R. Sana and his co-authors made the earliest and most influential modern contributions to the development of AO for power transmission lines, their work merits a detailed examination. Table 2.1 summarises, in chronological order, their key publications; the order presented does not necessarily correspond to the numbering in the reference list.

Their research builds on the foundations laid by the Prussian–American mathematician and electrical engineer C. P. Steinmetz, who, at the beginning of the twentieth century, established the fundamental principles for balancing three-phase loads using reactive-power injection [25]. These ideas were later generalised by Gyugyi *et al.* [26], who extended Steinmetz's approach to arbitrary, ungrounded three-phase loads.

The principal technical achievements of A. Sana and his collaborators can be summarised as follows.

They demonstrated that both a single HV transmission line and individual lines within a multi-line corridor can continue operating in AO mode after one or two phases are opened. Since AO of a single line is the most challenging configuration, this case is the primary focus of this Section and of the entire thesis.

A key requirement for maintaining AO is the suppression of negative- and zero-sequence currents at both extremities of the line. When these components are effectively mitigated, the sending- and receiving-end networks remain balanced and, as reported by the authors, approximately one-third and two-thirds of the pre-fault power can be transferred under OPAO and TPAO conditions, respectively. However, these results are revisited and re-analysed in Chapter 4.

Table 2.1 Summary of key works on AO of power transmission systems.

Type	Title	Year	Authors
Conf. paper	The exploitation of asymmetry in electric power transmission networks [2]	1998	A.-R. Sana, R. J. Marceau, C. Todde, X.-D. Do, J. Mahseredjian, and G. Joos
Conf. paper	An investigation into the compensation of asymmetric systems [8]	1999	C. Todde, R. J. Marceau, D. T. McGillis, S. Lefebvre, and A.-R. Sana
Conf. paper	On the asymmetrical operation of the transmission systems [9]	1999	A.-R. Sana, R. J. Marceau, D. T. McGillis, C. Todde, and X.-D. Do
Conf. paper	Asymmetrical operation of a corridor with one single line [27]	2000	A.-R. Sana, D. T. McGillis, R. J. Marceau, X.-D. Do, and G. Olivier
PhD thesis	Exploitation asymétrique des réseaux de transport d'énergie électrique [10]	2001	A.-R. Sana Supervisors: R. J. Marceau, D. T. McGillis, X.-D. Do
Conf. paper	The role of asymmetric operation in enhancing the flexibility of power system operation [23]	2003	R. J. Marceau, D. T. McGillis, and A.-R. Sana
Book	Asymmetric operation of AC power transmission systems [24]	2006	R. J. Marceau, D. T. McGillis, and A.-R. Sana

Figure 2.7 presents a conceptual representation of AO achieved through filters installed at both ends. Sana *et al.* showed that such filters can consist of either passive components (inductors and capacitors) or power-electronic devices. Their analytical formulations define the required sequence-current injections needed to suppress negative- and zero-sequence components under both TPAO and OPAO conditions. Although the use of FACTS devices for this purpose was proposed, detailed control strategies were not developed in the authors' works, and their design therefore constitutes one of the contributions of this thesis.

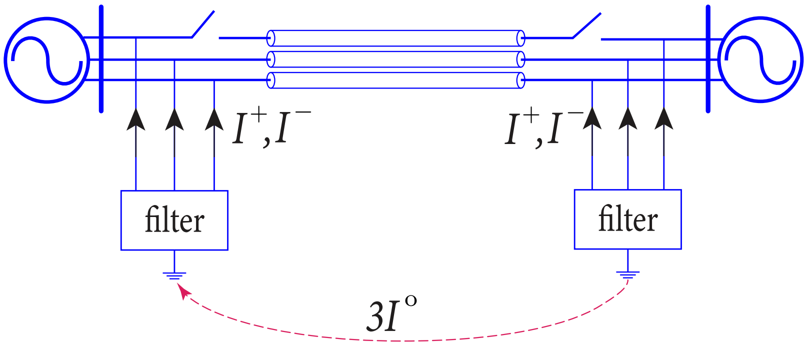

Figure 2.7 Conceptual representation of AO of a transmission line using filters at its extremities.

In their studies, a simplified π-section model was adopted, enabling direct computation of sequence currents using (this approach is critically evaluated in Chapter 4)

$$\begin{bmatrix} I^+ \\ I^- \\ I^o \end{bmatrix} = \frac{1}{3} \begin{bmatrix} 1 & a & a^2 \\ 1 & a^2 & a \\ 1 & 1 & 1 \end{bmatrix} \begin{bmatrix} I_a \\ I_b \\ I_c \end{bmatrix}.$$

For an open a-phase (taken as the reference), the phase currents become

$$I_a = 0, \qquad I_b = I_m a^2, \qquad I_c = I_m a,$$

which yields

$$\begin{bmatrix} I^+ \\ I^- \\ I^o \end{bmatrix} = \frac{1}{3} \begin{bmatrix} 2I_m \\ -I_m \\ -I_m \end{bmatrix}.$$

Similarly, when the a- and b-phases are open, the sequence currents become

$$I_a = 0, \qquad I_b = 0, \qquad I_c = I_m a,$$

$$\begin{bmatrix} I^+ \\ I^- \\ I^o \end{bmatrix} = \frac{1}{3} \begin{bmatrix} I_m \\ -I_m a^2 \\ -I_m a \end{bmatrix}.$$

This line of reasoning is valid only if each phase is treated as an independent electric circuit, as proposed by the authors, implying the absence of electromagnetic coupling between the phase conductors and between the conductors and the ground wires. Such an assumption is more suitable for short transmission lines, whose generic representation can be approximated by a simple rL impedance model. However, for medium-length and, in particular, long transmission lines—such as those considered in this thesis—the mutual electromagnetic couplings cannot be neglected. These aspects are examined in detail in Chapter 4.

Beyond the purely engineering aspects, Sana's doctoral work also included probabilistic and economic analyses to assess the feasibility of AO, demonstrating its applicability not only to single-line configurations but also to multi-line transmission corridors. He also showed that power-electronic filters can simultaneously suppress both negative- and zero-sequence currents, whereas passive filters typically require separate devices for each sequence network.

2.5.1 Zero-sequence current management

In the references listed in Table 2.1, no analysis of zero-sequence current distribution is presented, as the power-line model employed in those studies does not permit such an evaluation. In their conceptual approach, A. Sana *et al.* propose viewing each phase of a three-phase transmission line as an independent circuit. This perspective enables the implementation of passive- or power-electronic-based filters and facilitates zero-sequence compensation by calculating the sequence components at both extremities when one or two phases are open. However, this approach is not suitable for medium- or long-length transmission lines for the reasons discussed above.

The cited studies therefore suggest realising the zero-sequence current path through the shield wire or a dedicated grounding conductor, which in EHV/UHV overhead transmission lines is primarily intended for lightning protection. Nevertheless, the behaviour of a transmission line under AO must be assessed in terms of the *actual* zero-sequence current distribution paths and the influence of the open phase(s).

An alternative method for arranging the return path was initially proposed in [28] by the author of this thesis. The approach is inspired by practices employed in HVDC transmission systems, where the return current flows through earthing electrodes located at considerable distances (typically 10–45km) from the converter stations. Owing to the lower resistivity of deeper soil layers, deep electrodes provide more effective grounding [29, 30]. Furthermore, appropriate electrode design and geometry help minimise electrical hazards.

When grounding electrodes are used to carry zero-sequence current between compensators, several additional factors must be considered, including safety risks associated with elevated ground potentials, soil acidification, and long-term electrode corrosion. Monopolar and bipolar HVDC overhead lines have long utilised earth-return currents, which may offer insights for AC applications; however, AC systems introduce more stringent safety challenges due to alternating potentials and cyclic current reversals.

If ground currents circulate for extended periods, electrolysis may occur, degrading soil quality and potentially rendering land unsuitable for agricultural use [31]. Electrode corrosion is another important concern. References indicate that electrodes may degrade by approximately 20lb per DC ampere of continuous annual operation [30]. In asymmetrical AC systems, the zero-sequence current is alternating, which may further accelerate electrode degradation compared with DC operation.

In the meantime, the potential applicability of this technique to AC systems is supported by CIGRÉ recommendations [32], which specify that HVDC electrodes must be capable of carrying transient currents with magnitudes comparable to those on the main transmission line. As shown in the sample calculation in [32], the amplitude of transient currents flowing through HVDC electrodes exceeds the amplitude of the zero-sequence current under AO for a 500kV AC transmission line operating at 900MW surge impedance loading (SIL).

Although this approach shows promise, its practical implementation requires further detailed investigation, which lies beyond the scope of this thesis. Moreover, its deployment would necessitate additional capital expenditure. Therefore, throughout this thesis, the ground wires of the transmission lines are used as the return path for zero-sequence currents.

2.6 Other Literature on Power-Line AO Concepts

In [33], a comparison between symmetric and asymmetric operation of multiple parallel transmission lines is presented, including an economic assessment. Using the cost figures reported in [34]—20$/kVAr for series compensation and 8$/kVAr for shunt compensation—the authors concluded that, across all evaluated scenarios, the compensation requirements under AO result in higher overall costs than those associated with symmetrical operation. Consequently, for multi-line corridors, AO may not be economically advantageous when viewed purely from an investment perspective.

A related study in [35] analyses the post-fault operation of a transmission corridor following a phase-to-ground fault, comparing symmetrical and asymmetrical operating conditions. Through transient-stability simulations, the authors demonstrate that the use of Distributed Static Series Compensator (DSSC) modules can reduce investment costs while enhancing controllability of power flow, making them attractive for AO support. However, in both [33, 35], the compensation devices are treated as dedicated installations used solely to realise AO. With the increasing penetration of IBRs, this assumption becomes less representative of modern grids, since AO-related compensation could instead be provided as an ancillary service by the converters already present in the network, as discussed earlier in this chapter.

More recent publications [36, 37] revisit AO in the context of modern FACTS technologies. In [36], Assala *et al.* examine the use of an Interphase Power Controller (IPC 240) to support AO on a 30kV distribution line carrying a pre-fault active power of 3MW. A short-line model is adopted for the analysis. Since compensating negative- and zero-sequence currents does not fully restore the pre-fault power transfer, an additional scenario incorporating PV generation is considered. The results show that, without PV, the AO transfer capability is limited to approximately 2MW, whereas the inclusion of a PV source enables full restoration of the original 3MW power flow. Full restoration is desirable because it prevents broader system imbalances and avoids the need for corrective actions such as load shedding or generation redispatch.

In [37], Steva *et al.* analyse symmetric, TPAO, and OPAO operation of a 225kV, 168km-long transmission line. Two IPC 240 devices installed at the line extremities, together with a STATCOM at the receiving end, are used to compensate the asymmetry. The STATCOM contributes to reducing phase-to-phase voltage disparities and increases the receiving-end voltage magnitude, bringing it closer to nominal conditions. It also enhances active power transfer capability. The IPC 240 devices are shown to balance voltages and currents at the extremities even with two phases open. However, a key drawback is the requirement for centralised coordination between the two IPC units, necessitating reliable communication infrastructure.

It should be noted that both studies [36, 37] employ the simplified π-section line representation, and therefore do not capture zero-sequence current distribution or the electromagnetic interactions between phase conductors, shield wires, and tower-ground return paths. As a result, their conclusions, while informative, do not fully reflect AO behaviour on medium- and long-length EHV transmission lines.

2.7 Why Asymmetric Operation could be Beneficial for OPLs

Single-phase-to-ground, phase-to-phase, and double-phase-to-ground faults constitute the majority of fault events in EHV transmission networks. Consequently, the AO of power lines offers a promising means of enhancing system reliability, flexibility, survivability, and overall security of supply. By enabling continued operation when one or more phases are opened, AO allows the transmission line to remain energised with a reduced but non-zero power-transfer capability, thereby avoiding complete circuit outage and mitigating the impact of common fault contingencies on the wider network.

Based on real fault statistics, the authors of [38] provide field data which demonstrate that the proportion of single-phase-to-ground faults increases with both the voltage level and the physical dimensions of the transmission line. For instance, this fault type accounts for approximately 60% of all reported faults at 220 kV, rising to 97% at 750 kV. In contrast, the success rate of Single-Pole Automatic Reclosures (SPAR) decreases with increasing voltage level: it is reported as 72% at 330 kV and only 52% at 750 kV. Hence, for EHV and UHV transmission lines, there is effectively a 50% probability of successful SPAR operation. In the remaining cases, the tripping of a single phase results in the disconnection of the entire line. As discussed in [38], the reduction in SPAR effectiveness is associated with a decrease in specific tripping events at higher voltage levels, making non-clearable faults more prevalent.

The adoption of AO can substantially mitigate these issues. If SPAR is unable to restore the faulted phase, the affected phase may be isolated and the line operated under TPAO, thereby maintaining reduced, but non-zero, power transfer (assuming no energy-storage support). In the case of phase-to-phase or double-phase-to-ground faults, a similar strategy can be employed by isolating the faulted phases and implementing OPAO. Conversely, if the line is fully tripped, subsequent contingencies may lead to power-system splitting, load shedding, or even large-scale blackouts.

This risk is particularly pronounced in systems with long (>240 km), unreserved or insufficiently reserved single-circuit transmission corridors, where the N–1 security criterion is poorly satisfied (i.e., the loss of a single element such as a transmission line or transformer cannot be accommodated without load shedding or significant generation redispatch). Such configurations exist, for example, in Brazil and Kazakhstan, where bulk power is transferred over a limited number of long-distance lines connecting remote generation centres to major load areas. A similar situation may also arise within parts of the National Power System (NPS) in many countries, where tripping a backbone EHV transmission line is not usually a critical event under normal conditions but may nonetheless lead to adverse operational consequences. Notably, there are many countries have committed to increasing the penetration of RES, which further underscores the relevance of AO as a reliability- and resilience-enhancing strategy.

Moreover, in countries with large geographical areas, it is common for electric power transmission to rely on several series-connected transmission lines, often with intermediate branching points (illustrated by dashed lines), as shown in Figure 2.8. Under conventional operating practices, the tripping of a single line within such a series results in the loss of the entire transmission path. However, in some cases, one of these series-connected lines can be considered as a transmission link between two power subsystems, since each terminal node may have its own power injection. In such circumstances, AO enables the affected line to continue operating with one or two open phases, thereby preserving the transfer of electric power.

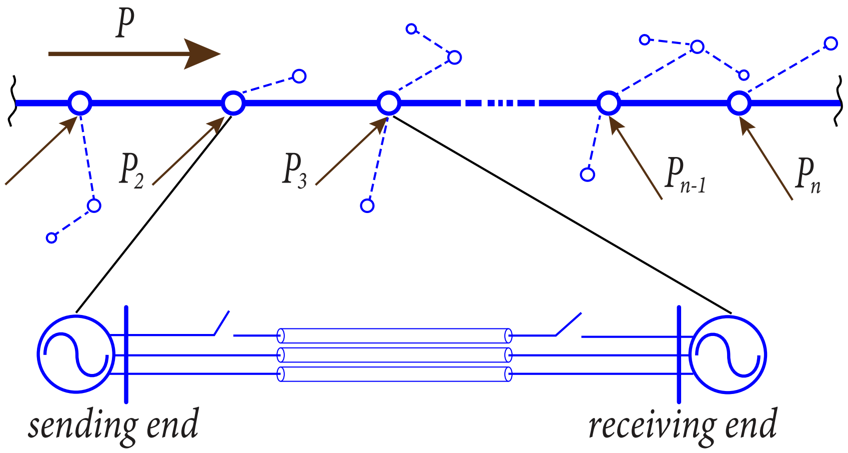

Figure 2.8 Electric power transmission via power lines connected in series and an example of a single line with an open phase.

For example, Kazakhstan has committed to increasing the share of RES from the current value of approximately 6% to 10% by 2030, with a long-term target of 50% by 2050 [39]. This transition is expected to increase the overall vulnerability of the power system. Consequently, the Kazakh power grid requires higher levels of flexibility, robustness, and resilience. Owing to the country's vast geographical area, which is the ninth largest globally, the uneven distribution of energy resources, and the densely populated southern region, the North–South transmission system forms the backbone of Kazakhstan's NPS. This system transfers electricity from the major Power Plants (PP) located in the northern zone to consumers in the south.

This system comprises three 500kV transmission corridors extending over more than 1000km and consisting of multiple series-connected power lines and generation units along the route. Two of these corridors run in close proximity through Central Kazakhstan, while the third traverses East Kazakhstan, as illustrated in Figure 2.9. Despite the redundancy provided by these circuits, the Southern zone continues to experience a substantial power deficit, rendering the NPS highly vulnerable to the loss of any one of these critical transmission corridors. This vulnerability is further exacerbated by the strict frequency-deviation limit (±10 mHz dead zone) imposed by the Russian System Operator (SO) [40]. Collectively, these factors constrain the level of RES penetration that can be reliably accommodated by NPS operators.

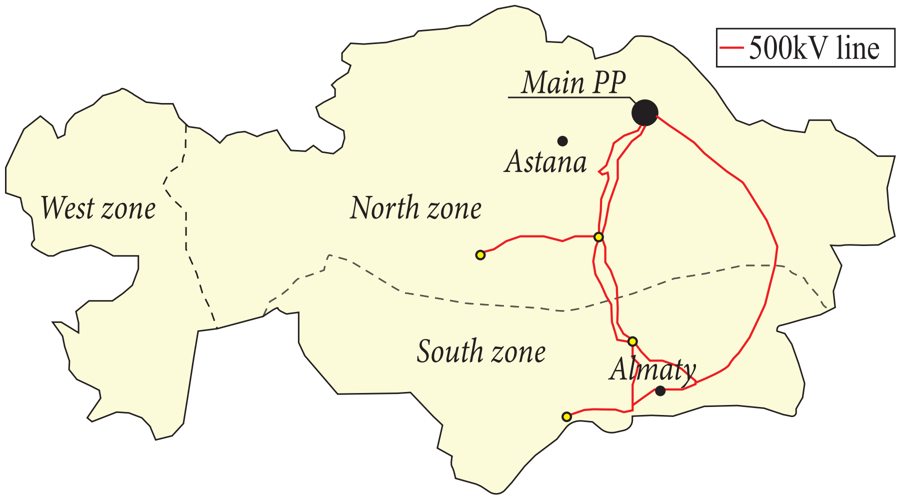

Figure 2.9 Simplified North-South electric power transmission network of Kazakhstan National Power System (PP - power plants, the system operator divides the NPS into three zones).

Another scenario in which AO is advantageous arises when a transmission path consists of a double-circuit arrangement or a limited number of parallel lines. In this context, AO allows the remaining healthy phases or circuits to carry a controlled portion of the power flow, thereby enhancing overall system reliability and improving the security of supply [9].

The improvement of power system reliability with AO is mainly associated with the higher successful operational probability of power lines. Figure 2.10a illustrates the logical reliability scheme for conventional symmetrical operation of a three-phase power line, where p is the successful operation probability of one phase conductor. In classical three-phase operation, the line can transmit power only if all three phase conductors remain in service. Therefore, the tripping of one or two faulted phase conductors, when automatic reclosure cannot restore them, leads to the disconnection of the entire power line. From the reliability point of view, the three phase conductors are therefore represented as series-connected elements: the failure of any single element causes the failure of the whole line. Consequently, the successful operation probability of the line is calculated as

$$p_{sym} = p \cdot p \cdot p = p^3. \tag{2.6}$$

If the electric power transmission path consists of several series-connected power lines (Figure 2.8), the resulting probability decreases further because the successful operation of the whole transmission path requires the successful operation of every line in the series.

In contrast, under AO, the loss of one or two phase conductors does not necessarily lead to the loss of the power line or the whole transmission path. The line may continue operating in an asymmetrical mode as long as at least one phase conductor remains available. Therefore, the phase conductors can be represented by a parallel reliability scheme, as shown in Figure 2.10b. In this case, the unsuccessful operation of the line occurs only when all three phase conductors are unavailable simultaneously. Thus, the successful operation probability of the power line is calculated as

$$p_{asym} = 1 - (1 - p)^3. \tag{2.7}$$

Figure 2.11 compares the successful operation probabilities of symmetrical operation and AO for p ranging from 0.4 to 1, together with their difference, p_{dif}. Considering the reduced effectiveness of SPAR at higher transmission voltage levels in EHV/UHV Overhead Power Lines (OPL), as demonstrated by the field data discussed above [38], AO can provide a significant reliability improvement compared with traditional symmetrical operation.

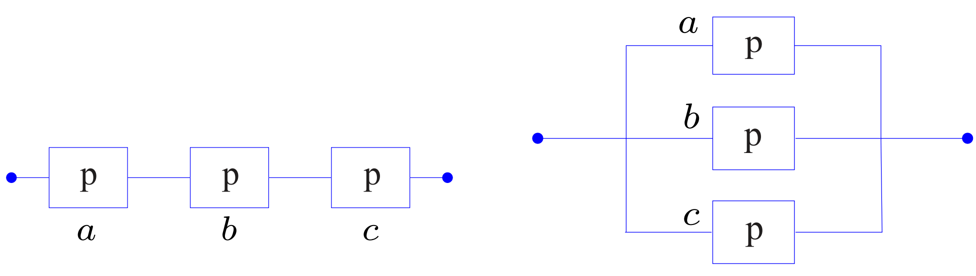

(a) Symmetrical operation probability: $A \cap B \cap C,\ p_{\text{sym}} = p^3$

(b) AO probability: $A \cup B \cup C,\ p_{\text{asym}} = 1 - (1 - p)^3$

Figure 2.10 Logic schemes of the probability of power-line tripping [2]: (a) symmetrical operation, (b) asymmetrical operation.

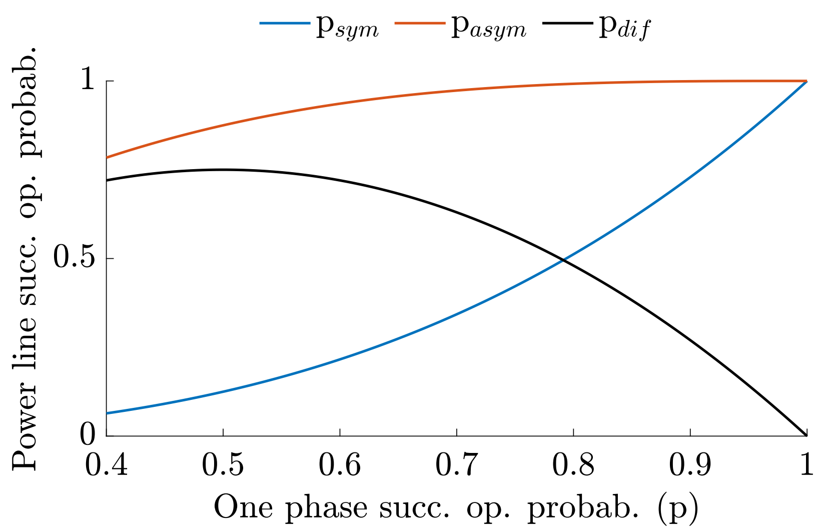

Figure 2.11 Successful OPL probability in symmetric and AO.

2.8 Sequence components detection and control

As mentioned earlier, AO of a power line requires the suppression of negative- and zero-sequence currents at the OPL terminals. Although the main objective of this work is not harmonic filtering, the detection and control of sequence components are closely related to the methods commonly used for harmonic mitigation. This relationship arises because three-phase harmonic components can also be classified according to their sequence type, namely positive, negative, or zero sequence. Consequently, many harmonic detection and control techniques can be adapted for the detection and suppression of negative- and zero-sequence current components during AO.

Moreover, most research papers address harmonic detection and control as a broader problem that also includes sequence-component extraction and compensation. For this reason, this section reviews harmonic detection and control methods as a general methodological basis for detecting and compensating selected sequence components of current, with subsequent application to AO.

Harmonics detection methods

Harmonic-suppression in practice consists of two key steps: (i) detecting the required components, and (ii) generating control actions using a dedicated controller. Figure 2.12 shows commonly used detection techniques. These are generally grouped into frequency-domain and time-domain methods [41].

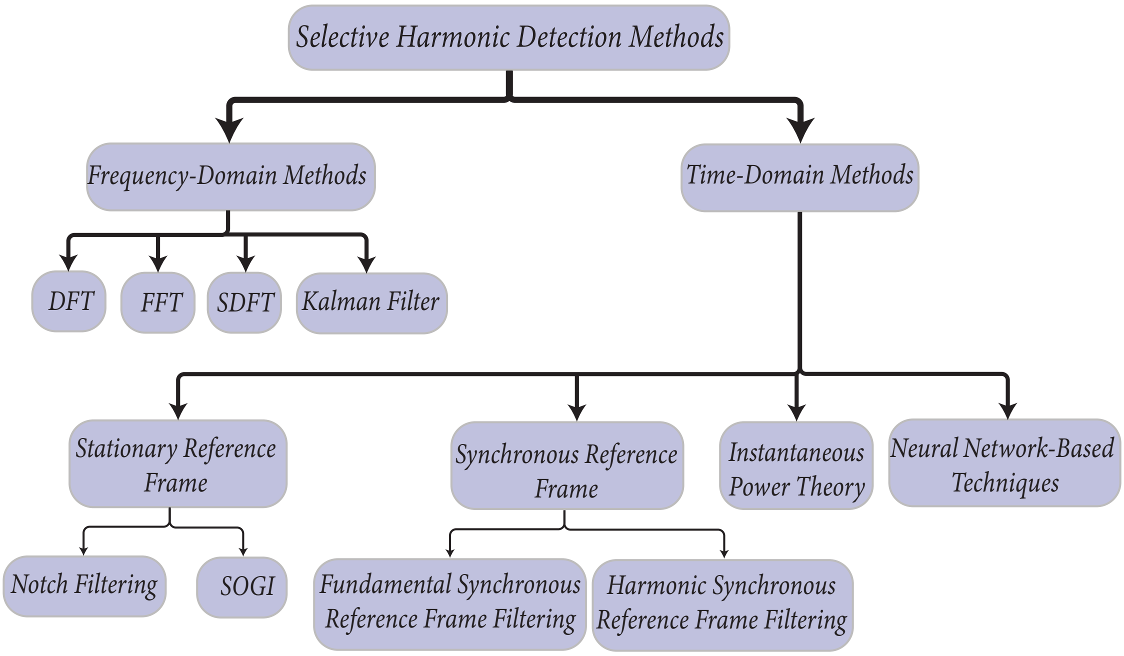

Figure 2.12 Classification of common harmonic detection techniques.

The most widely used harmonic detection frequency-domain techniques are the Discrete Fourier Transform (DFT) and the Fast Fourier Transform (FFT) [42]. The DFT maps sampled time-domain signals into the frequency domain and provides the magnitude and phase of the spectral components up to the Nyquist frequency, including the fundamental component. The FFT computes the same transform with a substantially reduced computational burden, provided that its algorithmic constraints are satisfied [43].

For real-time control applications, the DFT is often reformulated into a sliding implementation, commonly referred to as the Sliding Discrete Fourier Transform (SDFT). In this approach, the frequency-domain coefficients are updated recursively as the analysis window advances with each new sample, thereby avoiding repeated full-window evaluations. This structure enables efficient online tracking of selected harmonic components while maintaining a fixed observation window.

Non-Fourier frequency-domain estimators have also been applied to harmonic extraction, for example, Kalman filter-based tracking [44]. Benchmark studies report that such estimators generally require a minimum of one fundamental cycle (20ms at 50Hz) to converge, impose larger memory requirements, and incur higher computational cost [41, 43]. These attributes limit their suitability for real-time control of fast-acting power-electronic compensators, particularly VSC-interfaced FACTS systems in AO scenarios. Nonetheless, they remain valuable for harmonic metering, network monitoring, and offline analysis.

In the time domain, harmonic filtering approaches span multiple categories, including: (i) stationary reference-frame filters (frequently implemented in the $\alpha\beta$ frame); (ii) synchronous reference-frame (SRF) schemes formulated in the dq frame; (iii) hybrid or mixed-frame realisations; (iv) instantaneous power theory, i.e., p–q theory; and (v) data-driven approximators such as artificial neural networks (ANNs). In the context of AO support to EHV OPLs using IBRs, harmonic detection and control must integrate with existing control loops; therefore, linear controllers are prioritised in this thesis. A further limitation of advanced optimal or data-driven synthesis methods (e.g., MPC, ANN-based control) is the increased difficulty of conducting analytical stability assessment for IBRs at the grid scale.

The simplest harmonic detection method in the stationary frame is the network-frequency notch filter, tuned to the nominal grid frequency. By imposing strong rejection at the fundamental, the filter output emphasises the non-fundamental components of the signal, which can then be post-processed to infer its harmonic content — a principle commonly referred to in the power-quality literature as *fundamental notch filtering*. A more structured and widely adopted family of stationary-frame harmonic extractors is based on the Second-Order Generalised Integrator (SOGI), also termed the Sinusoidal Signal Integrator (SSI) [45, 46]. Individual SOGI units are typically configured as narrowband resonators, each tuned to specific harmonic orders for selective estimation and compensation — most often the 5th and 7th. Unlike wide-rejection notch filters, a single tuned SOGI produces estimates only for its design-centre frequencies and does not provide access to the full set of harmonic and interharmonic components present in the signal.

To enhance multi-harmonic estimation fidelity, the Multiple SOGI (MSOGI) structure employs several single-frequency SOGI resonators in parallel [46]. In MSOGI implementations, estimated harmonic components are exchanged between subsystems through internal feedback paths, where each resonator subtracts the harmonic estimates produced by neighbouring subsystems from its local input channel. This reduces inter-resonator leakage and improves tuned-frequency selectivity.

Some other time-domain harmonic detection methods include Akagi's instantaneous p–q power theory [47] and special power theory based approaches. Such methods are commonly applied for power-quality improvement. Comparisons reported in [43] emphasise that the requirement for additional filtering stages (e.g., LPFs) is a key limitation when p–q theory is used, primarily due to the extra delay introduced, which presents a disadvantage in terms of achievable detection speed.

Harmonics control methods

Among linear controllers, the most widely adopted strategies for current suppression in VSCs are based on the SRF and the Generalised Integrator (GI) approaches. Both methods have been developed to overcome the inherent limitations of the conventional Proportional–Integral (PI) controller, as explained below.

The transfer function of the PI controller is given by

$$F_{\mathrm{PI}}(s) = k_p + \frac{k_i}{s}. \tag{2.8}$$

If current of a three-phase VSC connected to the grid, represented by Equation 3.8, is controlled without applying the Park transformation, the corresponding single-phase control circuit is illustrated in Figure 2.13. The closed-loop reference-tracking transfer function of this circuit can then be expressed as

$$\frac{i(s)}{i^*(s)} = \frac{k_p s + k_i}{\dfrac{L_f}{(V_{dc}/2)} s^2 + \left(k_p + \dfrac{r_f}{(V_{dc}/2)}\right) s + k_i}. \tag{2.9}$$

The corresponding closed-loop gain and phase shift are

$$|G_0(\omega)| = \sqrt{\frac{k_i^2 + (k_p\omega)^2}{\left(k_i - \frac{2L_f}{V_{dc}}\omega^2\right)^2 + \omega^2\left(k_p + \frac{2r_f}{V_{dc}}\right)^2}}, \tag{2.10}$$

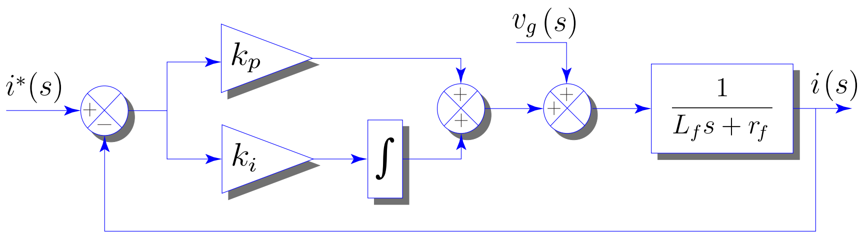

Figure 2.13 Current control loop for a VSC.

$$\varphi = \arctan\left(\frac{k_p\omega}{k_i}\right) - \arctan\left(\frac{\omega\left(k_p + 2r_f/V_{dc}\right)}{k_i - \left(2L_f/V_{dc}\right)\omega^2}\right), \tag{2.11}$$

Since the optimal frequency response is achieved when the gain equals unity and the phase shift is zero, Equations 2.10 and 2.11 satisfy these conditions only at $\omega = 0$. Therefore, a PI controller eliminates the steady-state error exclusively for DC references. When sinusoidal components are present, the steady-state error cannot be fully eliminated and, moreover, increases with frequency.

SRF-based control: The SRF approach is described in detail in Section 3.3, as it is employed in this research. In its second step, the method applies Park transformation to map AC variables into the rotating dq frame, where they appear as DC-type quantities. PI controllers can then regulate these components with zero steady-state error. However, for harmonic suppression, each targeted harmonic requires a dedicated dq frame and an additional Low-Pass Filter (LPF), as illustrated in Figure 2.15. Although effective, this results in significant computational effort and introduces delays in detection and compensation [48, 49].

Proportional–Resonant (PR) control: To overcome the computational burden of multiple SRFs, stationary-frame GI-based controllers have been proposed. The most common is PR controller. Its transfer function is

$$F_{PR}(s) = k_p + \frac{2k_i s}{s^2 + \omega^2}, \tag{2.12}$$

where the resonant term yields infinite gain at ω_0, ensuring zero steady-state error in tracking sinusoidal signals at that frequency. The PI controller may be considered a special case of the PR controller when $\omega = 0$.

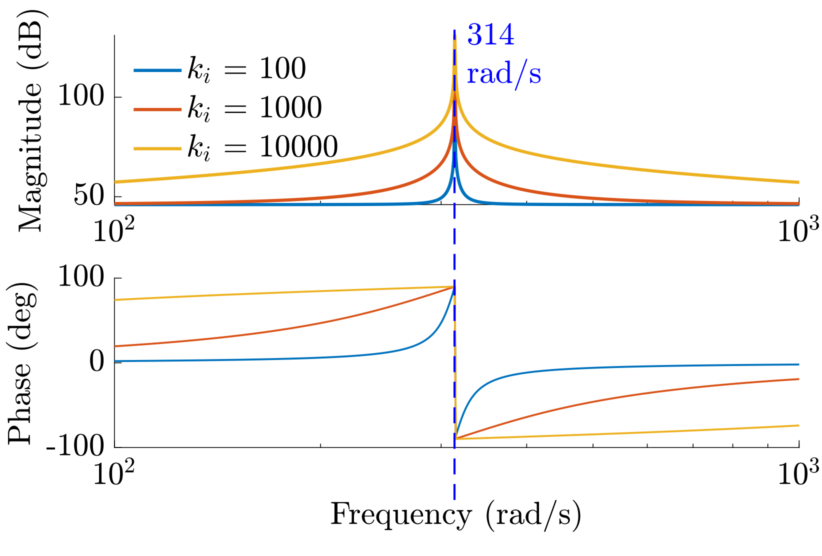

Figure 2.14 Typical Bode plot of the PR controller.

Despite its advantages, the PR controller exhibits a narrow resonant band, making it sensitive to grid-frequency deviations and challenging to tune [50]. Figure 2.14 illustrates a typical Bode plot of the PR controller for $\omega = 2\pi \times 50$ rad/s and different values of k_i. Non-ideal PR controllers employing the SOGI extend the bandwidth at the cost of a residual steady-state error [51].

Analysis of the 2DF-IMC technique for fast harmonic current mitigation:

To address the combined limitations of SRF and PR-based methods in active power filters, Campos-Gaona *et al.* [11] proposed the Two Degrees of Freedom Internal Model Control (2DF-IMC) to suppress higher harmonics. This method eliminates the need for LPFs in the closed loop controller structure, thereby significantly improving harmonic detection and suppression speed. Whereas Campos-Gaona *et al.* demonstrated in [11] harmonic mitigation in active power filters, this thesis extends the approach to the suppression of sequence components. Specifically, two E-STATCOMs are deployed at the terminals of the EHV OPL to suppress negative- and zero-sequence currents under balanced and constant voltages, thus enabling AO. In this framework, the negative-sequence current is treated as a harmonic in the negative SRF, facilitating accurate detection and effective compensation.

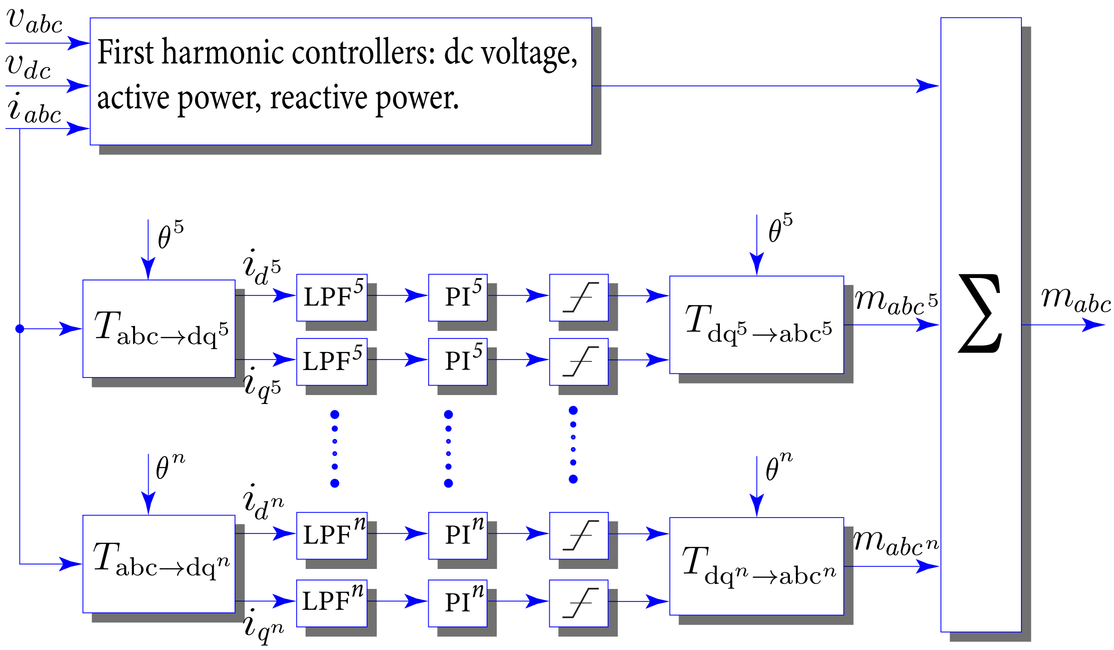

Figure 2.15 Conventional SRF-based controllers.

2.9 Conclusion

This chapter reviewed the key challenges facing modern power networks and presented the case for AO as a viable means of enhancing reliability and security of supply. It demonstrated that faults on long EHV/UHV transmission lines, and the subsequent disconnection of phase conductors, pose increasing risks to national renewable-energy integration strategies. The ability of AO to preserve most of the active power flow following a permanent or transient phase outage was shown to be highly beneficial for strengthening grid resilience and ensuring continuity of supply.

The chapter also highlighted historical and contemporary cases of asymmetric power transfer, including legacy AC transmission schemes and open-phase transformer configurations that remain operational today. While the pioneering contributions of AO researchers were summarised, their methodological limitations were critically assessed, particularly the inability of the simplified π-section line model to represent electromagnetic couplings between healthy and disconnected conductors, shield wires, and tower-ground return paths.

In addition, existing control methodologies for IBRs were examined in the context of AO applicability. Frequency-domain and time-domain harmonic suppression techniques were reviewed, with discussion of their suitability for real-time control. It was further shown that SRF control, implemented through a 2DF-IMC structure, enables selective harmonic mitigation without the need for LPFs. This “filterless” characteristic eliminates measurement delays, thereby improving achievable estimation and control bandwidth. Among the assessed options, the SRF-based 2DF-IMC approach exhibits superior response speed for fast power-electronic devices.

Overall, the synthesis of historical AO concepts, foundational research, and modern filterless SRF-based control approaches establishes a strong basis for further investigation of AO-enabled power lines. The topic offers substantial scope for future contributions across FACTS devices.

The next chapter details the IBR device and its control architecture used to realise AO of an EHV overhead transmission line, including system modelling and controller design. The SRF method is applied to detect current sequence components, and the corresponding sequence-component controllers are validated.

Chapter 3

E-STATCOM modelling and Control for Fast Control and Mitigation of Sequence Components

3.1 E-STATCOM Modelling

Static Synchronous Compensators (STATCOM) have established themselves over the past decades as reliable and robust technologies for regulating voltage levels in EHV power systems through the injection or absorption of reactive power. When a STATCOM is equipped with an energy storage system to provide ancillary services such as inertial response or Fast Frequency Response (FFR), it is referred to as an E-STATCOM [52].

Some authors, for example T. Engelbrecht *et al.* in [53], employ the energy source of an E-STATCOM as supercapacitors, thereby distinguishing it from Battery Energy Storage Systems (BESS). In this thesis, however, batteries are employed as the energy source of the E-STATCOM. The rationale is twofold. First, batteries integrated into E-STATCOMs at the extremities of OPLs are not required to store large amounts of energy, as would typically be expected from a BESS, in order to perform two-phase or one-phase AO, provided that the pre-fault power flow is not fully restored. Secondly, no universally accepted classification exists, and in most cases the term 'energy storage' is used generically to encompass a variety of technologies.

The focus of this thesis is on AO as an ancillary service that could be delivered by transmission-level converter-based installations equipped with suitable control capability. If partial restoration of the pre-fault power flow is required, an appropriate dc power source is also necessary. The E-STATCOM is used as the representative

IBR platform because it combines the fast controllability of a STATCOM with the possibility of active-power injection through its dc-side energy source.

In this work, the E-STATCOM is therefore considered as a conceptual and technically suitable VSC-based platform for implementing AO. Nevertheless, the AO control methods proposed in this thesis are generalisable to other VSC-based IBRs, provided that they have sufficient current rating and suitable control capability.

Accordingly, this section is structured into two subsections. The first describes the power electronic interface between the energy storage system and the grid, while the second focuses on the representation of the energy storage itself.

3.1.1 Three-phase Voltage Source Converter

A variety of power electronic converters with different topologies for STATCOMs exist. The most common topologies include the three-phase two-level, three-level, and Modular Multilevel Converter (MMC). Increasing the number of levels reduces the presence of higher-order harmonics produced by high-frequency switching.

When Total Harmonic Distortion (THD) is not the primary focus of the study, as is the case here, the averaged two-level VSC model can be adopted instead of a detailed switching model. As demonstrated by Yazdani and Iravani [3], the averaged model reproduces the same dynamic behaviour while excluding the high-frequency switching components.

Since the zero-sequence current must be suppressed and so controlled, the dc-link of the power electronic structure is divided into two. This topology is commonly referred to as the three-leg four-wire (3L4W) converter. Figure 3.1 illustrates this topology including an AC-side inductance, which serves two purposes:

(i) attenuation of higher-order harmonics,

(ii) creation of a controllable power angle δ between the grid and the VSC, thereby enabling active power exchange.

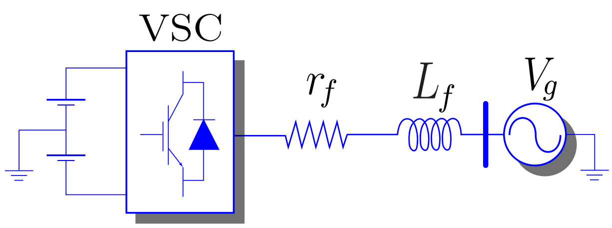

Figure 3.1 Single-line representation of a three-phase (3L4W) VSC connected to the grid with a filter.

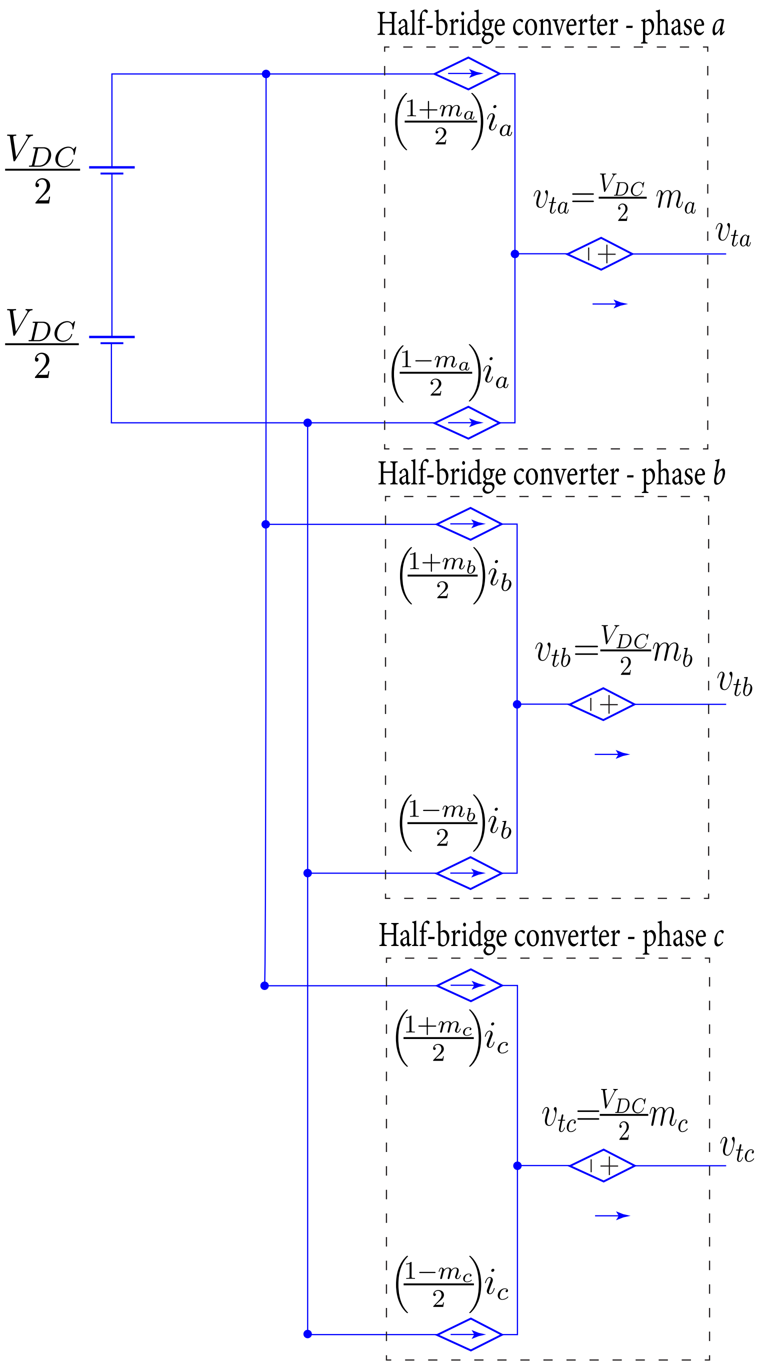

Figure 3.2 Average-value equivalent circuit of a two-level VSC, adapted from [3].

Figure 3.2 illustrates the averaged equivalent circuit of a VSC, which is composed of three half-bridge converters, one per phase. Neglecting the parasitic on-state resistances, the configuration reduces to an ideal three-phase VSC, with the corresponding terminal voltages defined as

$$v_{ta} = \frac{V_{dc}}{2}\, m_a, \tag{3.1a}$$

$$v_{tb} = \frac{V_{dc}}{2}\, m_b, \tag{3.1b}$$

$$v_{tc} = \frac{V_{dc}}{2}\, m_c. \tag{3.1c}$$

The modulation signals for each phase can be expressed as

$$\begin{aligned} m_a &= \hat{m}\, \cos(\omega t), \\ m_b &= \hat{m}\, \cos\!\left(\omega t - \tfrac{2\pi}{3}\right), \\ m_c &= \hat{m}\, \cos\!\left(\omega t - \tfrac{4\pi}{3}\right). \end{aligned} \tag{3.2}$$

The instantaneous power balance between the dc and ac sides of the ideal converter is then obtained as

$$V_{dc}\, i_{dc} = v_{ta}\, i_a + v_{tb}\, i_b + v_{tc}\, i_c. \tag{3.3}$$

From Equations 3.1–3.3, alternative dynamic models in the dq or $\alpha\beta$ reference frames may be systematically derived [3].

3.1.2 Battery modelling

As discussed previously, a variety of energy storage technologies can serve as the energy source for an E-STATCOM. In this study, a lithium-ion battery is employed, as this technology is more flexible in providing ancillary services to the grid, [54], and is presently the fastest-growing across different applications owing to its high efficiency and scalability [55]. For the simulations presented in Chapter 5, the battery is represented by a SIMULINK block, with its parameters provided in the Appendix C.3, and is characterised by the following equations [56, 4]:

Discharge Model ($\tilde{i} > 0$)

$$f_1(q, \tilde{i}, i) = E_0 - K \cdot \frac{q_{max}}{q_{max} - q} \cdot i - K \cdot \frac{q_{max}}{q_{max} - q} \cdot q + A_{bat} \cdot \exp(-B_{bat} \cdot q). \tag{3.4}$$

Charge Model ($\tilde{i} < 0$)

$$f_2(q, \tilde{i}, i) = E_0 - K \cdot \frac{q_{max}}{q + 0.1 \cdot q_{max}} \cdot i - K \cdot \frac{q_{max}}{q_{max} - q} \cdot q + A_{bat} \cdot \exp(-B_{bat} \cdot q). \tag{3.5}$$

The corresponding equivalent circuit of the battery block is illustrated in Figure 3.3.

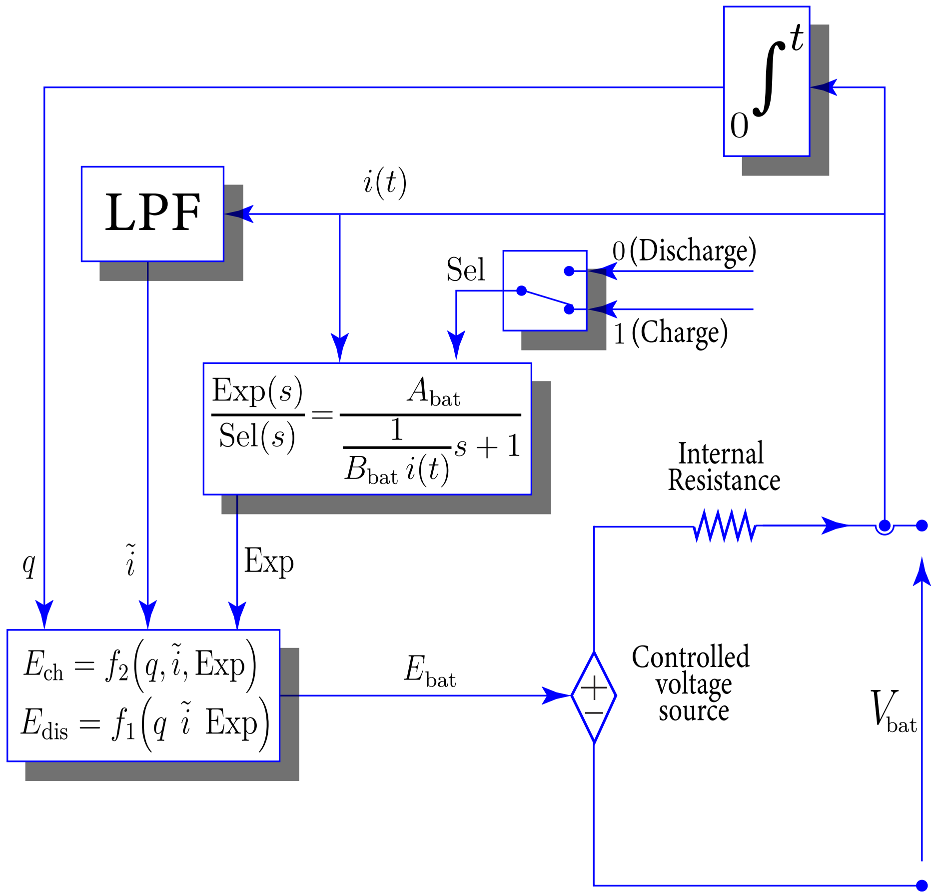

Figure 3.3 Equivalent circuit representation of the lithium-ion battery block [4].

The battery model has the next **limitations** and **assumptions**:

Model limitations

- The open-circuit voltage of the battery is assumed to range from a minimum of 0V up to a maximum of $2E_0$.
- The battery capacity is considered to vary between a minimum of 0Ah and a maximum of q_{max}.

Model assumptions

- The internal resistance remains constant throughout charging and discharging cycles, independent of current magnitude.
- Model parameters are obtained from discharge characteristics, with the same behaviour assumed for both charging and discharging processes.

- The effective capacity of the battery does not depend on current amplitude (i.e., the Peukert effect is neglected).
- Battery self-discharge is not explicitly included; it may be approximated by introducing a large parallel resistance across the battery terminals.
- The battery is assumed to be free from memory effects.

3.1.3 Three-phase VSC connected to the grid modelling

When a source-agnostic three-phase VSC average model is connected to the grid, as represented in Figure 3.1, its dynamics can be expressed as

$$\begin{bmatrix} v_{ta} \\ v_{tb} \\ v_{tc} \end{bmatrix} - \begin{bmatrix} v_{ga} \\ v_{gb} \\ v_{gc} \end{bmatrix} = r_f \begin{bmatrix} i_{fa} \\ i_{fb} \\ i_{fc} \end{bmatrix} + L_f \frac{d}{dt} \begin{bmatrix} i_{fa} \\ i_{fb} \\ i_{fc} \end{bmatrix}. \tag{3.6}$$

which, considering the duty-cycle–modulation–*dc*-link voltage relationship, can be rewritten as

$$\frac{V_{dc}}{2} \begin{bmatrix} m_a \\ m_b \\ m_c \end{bmatrix} - \begin{bmatrix} v_{ga} \\ v_{gb} \\ v_{gc} \end{bmatrix} = r_f \begin{bmatrix} i_{fa} \\ i_{fb} \\ i_{fc} \end{bmatrix} + L_f \frac{d}{dt} \begin{bmatrix} i_{fa} \\ i_{fb} \\ i_{fc} \end{bmatrix}. \tag{3.7}$$

In compact matrix form, this can be written as

$$\frac{V_{dc}}{2} \mathbf{m}_{abc} - \mathbf{v}_{gabc} = r_f \mathbf{i}_{fabc} + L_f \frac{d\mathbf{i}_{fabc}}{dt}. \tag{3.8}$$

Taking into account Equation B.2, Equation 3.8 can be rewritten as

$$\frac{V_{dc}}{2} \mathbf{m}_{abc} - \mathbf{v}_{gabc} = r_f \mathbf{i}_{fabc} + L_f \frac{d}{dt} (T^{-1}_{abc \to dq^+} \mathbf{i}_{fdqo}). \tag{3.9}$$

By applying the derivative product rule,

$$L_f \frac{d}{dt} (T^{-1}_{abc \to dq^+} \mathbf{i}_{fdqo}) = L_f \frac{d}{dt} (T^{-1}_{abc \to dq^+}) \mathbf{i}_{fdqo} + L_f T^{-1}_{abc \to dq^+} \frac{d}{dt} (\mathbf{i}_{fdqo}) \tag{3.10}$$

and since

$$\frac{d}{dt}T^{-1}_{abc\to dq^+} = T^{-1}_{abc\to dq^+}W, \quad W = \begin{bmatrix} 0 & -\omega & 0 \\ \\ \omega & 0 & 0 \end{bmatrix}, \tag{3.11}$$

Equation 3.9 can be rewritten, taking into account Equations (3.10-3.11), as

$$\frac{V_{dc}}{2}\mathbf{m}_{abc} - \mathbf{v}_{gabc} = r_f\mathbf{i}_{fabc} - L_f T^{-1}_{abc\to dq^+}W\mathbf{i}_{fdqo} + L_f T^{-1}_{abc\to dq^+}\frac{d}{dt}(\mathbf{i}_{fdqo}). \tag{3.12}$$

Multiplying both sides of Equation 3.12 by $T_{abc\to dq^+}$ gives

$$\frac{V_{dc}}{2}\mathbf{m}_{dq0} - \mathbf{v}_{gdq0} = r_f\mathbf{i}_{fdq0} + L_f W\mathbf{i}_{fdqo} + L_f\frac{d}{dt}(\mathbf{i}_{fdqo}). \tag{3.13}$$

Since $\dot{\theta} = \omega_g$, the expanded form of Equation 3.13, with the zero-sequence component eliminated and the terms rearranged, is obtained as

$$\begin{aligned} \frac{V_{dc}}{2}m_d - v_{gd} &= r_f i_{fd} + L_f\frac{di_{fd}}{dt} - \omega_g L_f i_{fq}, \\ \frac{V_{dc}}{2}m_q - v_{gq} &= r_f i_{fq} + L_f\frac{di_{fq}}{dt} + \omega_g L_f i_{fd}. \end{aligned} \tag{3.14}$$

Equation 3.14 represents the dq-axis form of Equation 3.7, which enables control to be performed in the SRF. The last terms on the right-hand side are the cross-coupling components, which indicate the interdependence between d and q components.

3.2 The 2DF-IMC controller

As the advantageous features of the 2DF–IMC stem directly from its design, a brief review of its theoretical foundation is provided. First, the 2DF–IMC belongs to the family of robust controllers and, therefore, ensures steady-state set-point tracking while maintaining stability even under variations in plant parameters. Second, it eliminates the need for low pass filters, as will be demonstrated in Section 3.5, thereby enabling a filterless approach that significantly accelerates the detection and suppression of current-sequence components. Third, owing to its structure, the 2DF–IMC exhibits strong disturbance-rejection capability, thereby enhancing dynamic performance and improving overall robustness.

In general, the Internal Model Control (IMC) strategy is based on the “internal model” principle, which states that effective plant control can be achieved only if the controller incorporates, either explicitly or implicitly, a representation of the controlled plant. A detailed description of the IMC structure and configuration is provided in [57, 58].

In order to ensure a realisable control, the IMC design procedure incorporates a LPF $L(s)$ in cascade with the IMC. Without this filter the IMC transfer function, which is selected as the inverse of the transfer function to control, would involve pure differentiators. The filter is expressed as

$$L(s) = \left(\frac{\alpha_{bw}}{s + \alpha_{bw}}\right)^n, \quad n \in \mathbb{N} \tag{3.15}$$

where the order of the filter, n, is selected according to the order of the plant $G(s)$.

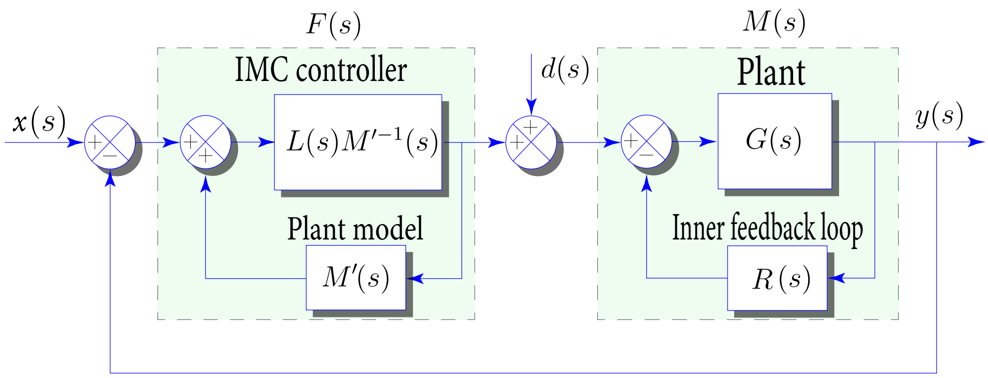

Figure 3.4 2DF-IMC configured as a PI controller.

Since, in principle, all plant parameters are incorporated within the IMC structure, the closed-loop bandwidth α_{bw} remains the only tuning parameter of the controller.

Figure 3.4 illustrates the IMC structure modified to explicitly separate the controller and plant sections within the closed-loop system. With this arrangement, the IMC behaves similarly to a PI controller when applied to first-order plants. Furthermore, Figure 3.4 depicts an inner feedback loop with gain $R(s)$ in the plant, which introduces a second degree of control freedom. This additional control action accelerates the natural response of the plant by shifting its pole further into the left half-plane of the complex domain. As a result, the disturbance-rejection capability of the plant is considerably enhanced. Importantly, this property is independent of the set-point tracking function of the controller.

The disturbance-rejection capability of the 2DF-IMC is specifically tailored to eliminate dc disturbances with zero steady-state error. This property is fundamental to enabling a filterless realisation of the SRF controller. As will be discussed in Section 3.5, removing the LPFs from the conventional SRF structure introduces ac harmonic components into the control loop. However, the 2DF-IMC effectively mitigates this harmonic contamination within the dc domain.

By introducing a feedback loop with gain $R(s)$, the transfer function of the improved plant becomes

$$M(s) = \frac{G(s)}{1 + G(s)R(s)} = \frac{1}{[G(s)]^{-1} + R(s)}, \tag{3.16}$$

where $M(s)$ denotes the improved transfer function of the plant.

Since the current sequence components suppression is realised by controlling current in $L_f r_f$ filter which is a first order plant, the corresponding IMC sequence transfer functions can be derived in a generalised form. Considering $M'(s)$ as the model of $M(s)$, the IMC transfer function $F(s)$ can be expressed as

$$F(s) = \frac{L(s)\,[M'(s)]^{-1}}{1 - L(s)\,M'(s)\,[M'(s)]^{-1}} = \frac{\alpha_{bw}}{s}[M'(s)]^{-1}. \tag{3.17}$$

A practical way to define $R(s)$ as a function of α_{bw} is to ensure that the plant's disturbance rejection matches the closed-loop dynamics of the controller as closely as possible. This alignment minimises the discrepancy between the plant's natural rejection and the controller's intended performance, thereby reducing control effort, improving robustness to parameter variations, and ensuring that disturbances are consistently attenuated across the system bandwidth. For the first-order plant shown in Figure 3.4, this condition can be readily satisfied.

$$\frac{y(s)}{d(s)} = \frac{M(s)}{1 + F(s)M(s)} = \frac{M(s)}{1 + \left(\frac{\alpha_{bw}}{s}\right)\,M(s)\,[M'(s)]^{-1}} = \left(\frac{s}{s + \alpha_{bw}}\right)\frac{1}{[G(s)]^{-1} + R(s)}, \tag{3.18}$$

$R(s)$ can be chosen in such a way that

$$\frac{y(s)}{d(s)} = \left[\left(\frac{s}{s + \alpha_{bw}}\right)\frac{K(s)}{s + \alpha_{bw}}\right] = K(s)\left[\frac{1}{(s + \alpha_{bw})^2}\right]. \tag{3.19}$$

Finally, the relationship between the rise time T_r and the closed-loop bandwidth of the controller is given by $\alpha_{bw} \approx 2.2/T_r$ [rad].

3.3 Sequence components detection

In this thesis the SRF method is employed to detect the negative-sequence current. The SRF used for negative-sequence detection rotates in the opposite direction to that used for positive-sequence detection. Hence, the positive- and negative-sequence current components are detected using θ and $-\theta$, respectively. As the sequence detection is realised in an EHV system, the three-phase voltage is assumed to be balanced and stable, and therefore the angle θ can be obtained from a three-phase PLL.

Figure 3.5 presents a vector diagram illustrating the detection of the positive- and negative-sequence components.

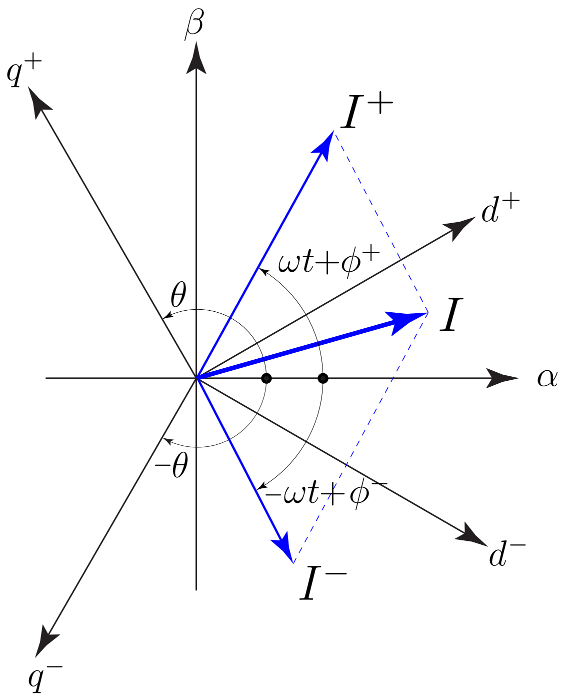

Figure 3.5 Sequence components detection by SRFs.

skipping intermediate calculations

When one of the phases in a three-phase system becomes open, sequence-component currents emerge. Equation 3.20 represents the instantaneous phase currents composed of positive- and negative-sequence components. The zero-sequence current is not included, as it remains unchanged after the transformation and represents the common-mode component.

$$\mathbf{i}_{abc} = \begin{bmatrix} i_a \\ i_b \\ i_c \end{bmatrix} = \begin{bmatrix} I_m^+ \sin(\omega t + \phi^+) + I_m^- \sin(\omega t + \phi^-) \\ I_m^+ \sin(\omega t - \frac{2\pi}{3} + \phi^+) + I_m^- \sin(\omega t + \frac{2\pi}{3} + \phi^-) \\ I_m^+ \sin(\omega t + \frac{2\pi}{3} + \phi^+) + I_m^- \sin(\omega t - \frac{2\pi}{3} + \phi^-) \end{bmatrix} = \begin{bmatrix} i_a^+ \\ i_b^+ \\ i_c^+ \end{bmatrix} + \begin{bmatrix} i_a^- \\ i_b^- \\ i_c^- \end{bmatrix}. \tag{3.20}$$

The dq currents in the positive-sequence reference frame, $\mathbf{i}_{dq^+}$, skipping intermediate calculations can be written as (the detailed derivation of $T_{abc \to dq^+}$ is shown in the Appendix B).

$$\mathbf{i}_{dq^+} = T_{abc \to dq^+}\,\mathbf{i}_{abc} = \begin{bmatrix} i_{d^+} \\ \\ i_{q^+} \end{bmatrix} = \begin{bmatrix} I_m^+ \cos(\phi^+) - I_m^- \cos(2\omega t + \phi^-) \\ \\ I_m^+ \sin(\phi^+) + I_m^- \sin(2\omega t + \phi^-) \end{bmatrix} = \begin{bmatrix} i_{dc.d^+} + i_{ac.d^+} \\ \\ i_{dc.q^+} + i_{ac.q^+} \end{bmatrix} \tag{3.21}$$

The terms $i_{dc.d^+}$ and $i_{dc.q^+}$ in Equation 3.21 represent the dc components (constants), which are determined by the positive-sequence current amplitude and its initial phase. In contrast, the second terms, $i_{ac.d^+}$ and $i_{ac.q^+}$, are sinusoidal quantities oscillating at twice the fundamental frequency (2ω), corresponding to the negative-sequence current amplitude and its initial phase. Therefore, the dc components are associated with the fundamental (positive-sequence) current, whereas the ac components correspond to the negative-sequence contribution at double the fundamental frequency.

The dq currents in the negative-sequence reference frame, i_{dq^-}, can be obtained by applying the negative-sequence Park transformation, $T_{abc \to dq^-}$, which is defined using the negative angle $-\theta$, to the phase currents. The detailed derivation of $T_{abc \to dq^-}$ is provided in Appendix B.

$$\mathbf{i}_{dq^-} = T_{abc \to dq^-}\,\mathbf{i}_{abc} = \begin{bmatrix} i_{d^-} \\ \\ i_{q^-} \end{bmatrix} = \begin{bmatrix} -I_m^- \cos(\phi^-) + I_m^+ \cos(2\omega t + \phi^+) \\ \\ I_m^- \sin(\phi^-) + I_m^+ \sin(2\omega t + \phi^+) \end{bmatrix} = \begin{bmatrix} i_{dc.d^-} + i_{ac.d^-} \\ \\ i_{dc.q^-} + i_{ac.d^-} \end{bmatrix} \tag{3.22}$$

In contrast to the positive-sequence transformation given in Equation 3.21, the terms $i_{dc.d^-}$ and $i_{dc.q^-}$ in Equation 3.22 represent the dc components (constants), which are determined by the negative-sequence current amplitude and its initial phase. Conversely, the second terms, $i_{ac.d^-}$ and $i_{ac.q^-}$, are sinusoidal quantities oscillating at twice the fundamental frequency (2ω), corresponding to the positive-sequence current amplitude and its initial phase. Therefore, in this transformation, the dc components are associated with the negative-sequence current, whereas the ac components correspond to the positive-sequence contribution at double the fundamental frequency.

SRF-based sequence components detection example

To evaluate the performance of the current sequence-component detection method, a simple circuit was used, as shown in Figure 3.6, where the a-phase was opened to introduce asymmetry. Table 3.1 lists the circuit parameters and the measured sequence components obtained from the embedded *Sequence Analyzer* block in Simulink.

Figure 3.7 shows the resulting i_{dq^+} and i_{dq^-} waveforms. Subplots (a) and (b) correspond to i_{d^+} and i_{q^+}, respectively, while Subplots (c) and (d) correspond to i_{d^-} and i_{q^-}. The curves demonstrate the expected behaviour: the dc components represent the i_d and i_q currents aligned with their respective reference angles (θ^+ or θ^-), whereas the ac components correspond to the opposite-sequence currents oscillating at twice the fundamental frequency. The analytically obtained waveforms from Equations 3.21 and 3.22 (dashed red lines) overlap with the simulation results, confirming the correctness of the derived expressions. The components i_{d^+} and i_{q^+} were calculated using θ^+, and i_{d^-} and i_{q^-} were calculated using θ^-. When the magnitudes are determined as $\sqrt{i_d^2 + i_q^2}$ for the positive and negative sequences, the resulting values match those reported in Table 3.1, validating the adopted technique for current sequence-component detection. It is evident that in order to perform typical vector control in either the positive- or negative-sequence dq values, a LPF of reduced bandwidth is needed to isolate the dc components of the signals. This invariably reduces the speed of response of a close loop system. Notwithstanding, the use of LPF in the control structure can be avoided if 2DF-IMC is used. The reasons for this are analysed in detail in the next section.

Table 3.1 Circuit parameters and measured current sequence components.

Voltage (kV)	Load (MW)	I^+ (A)	I^- (A)
500	700	$762\angle 19.55°$	$381\angle -160.5°$

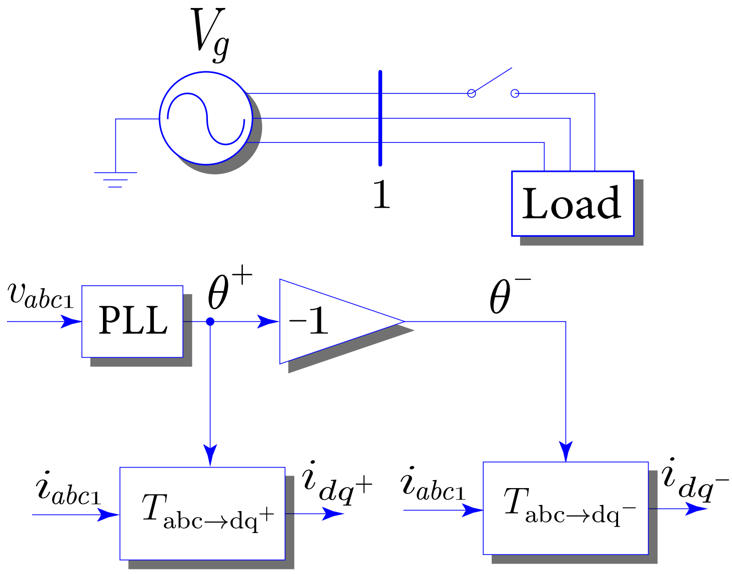

Figure 3.6 Positive- and negative-sequence dq currents detection.

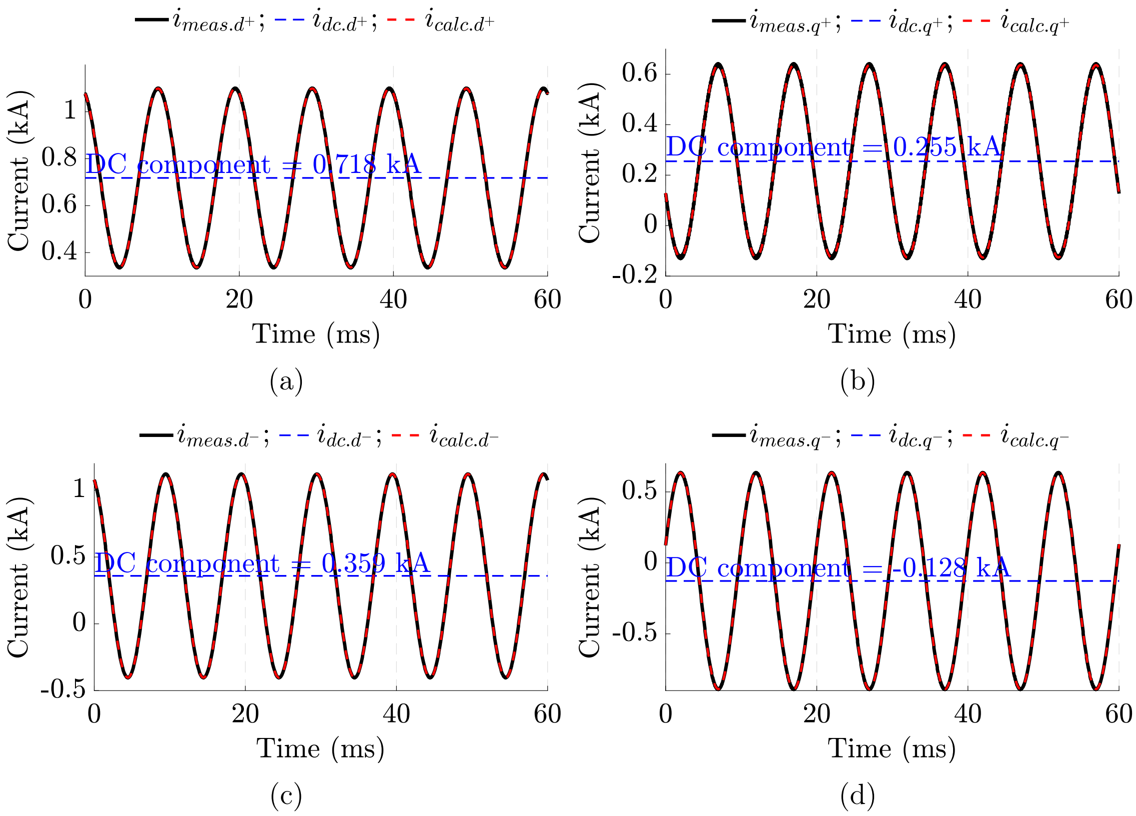

Figure 3.7 Positive- and negative-sequence dq currents. Subfigures (a) and (b) show i_{d^+} and i_{q^+}, respectively, while subfigures (d) and (e) show i_{d^-} and i_{q^-}.

3.4 Design of sequence-component controllers

This section presents the design of the 2DF-IMC for each current sequence component of the E-STATCOM connected to the grid, as illustrated in Figure 3.1. This configuration enables full control of the sequence components and, consequently, facilitates the realisation of OPL AO, which will be demonstrated in Chapter 5.

Equation 3.14 represents the general form of the relationship, where the current components i_{fd} and i_{fq} comprise all sequence components:

$$\begin{aligned} i_{fd} &= i_{fd^+} + i_{fd^-} + i^{\mathrm{o}}_{fd}, \\ i_{fq} &= i_{fq^+} + i_{fq^-} + i^{\mathrm{o}}_{fq}. \end{aligned} \tag{3.23}$$

Since the control of each sequence component is implemented separately, the resulting modulation signals for the E-STATCOM must be combined as

$$\mathbf{m}_{abc} = \mathbf{m}^+_{abc} + \mathbf{m}^-_{abc} + \mathbf{m}^{\mathrm{o}}_{abc}. \tag{3.24}$$

3.4.1 Positive-sequence current control

The positive-sequence form of Equation 3.14 becomes

$$\begin{aligned} \frac{V_{dc}}{2} m_{d^+} - v_{d^+} &= r_f i_{fd^+} + L_f \frac{di_{fd^+}}{dt} - \omega L_f i_{fq^+}, \\ \frac{V_{dc}}{2} m_{q^+} - v_{q^+} &= r_f i_{fq^+} + L_f \frac{di_{fq^+}}{dt} + \omega L_f i_{fd^+}. \end{aligned} \tag{3.25}$$

After applying the Laplace transform and rearranging Equation 3.25, the following transfer functions are obtained:

$$\begin{aligned} \frac{i_{fd^+}(s)}{(V_{dc}/2)\, m_{d^+}(s) - v_{d^+}(s) + \omega L_f i_{fq^+}(s)} &= \frac{1}{L_f s + r_f}, \\ \frac{i_{fq^+}(s)}{(V_{dc}/2)\, m_{q^+}(s) - v_{q^+}(s) - \omega L_f i_{fd^+}(s)} &= \frac{1}{L_f s + r_f}. \end{aligned} \tag{3.26}$$

Since v^+_{dq} and $i^+_{fdq}\omega L_f$ are known quantities, they can be treated as disturbances and eliminated by means of feedforward compensation. Accordingly, the positive-sequence current controller, derived in accordance with Equation 3.17, is expressed as

$$F^+(s) = \alpha^+_{bw} L_f + \frac{\alpha^+_{bw}(r_f + R^+)}{s} = k^+_p + k^+_i \frac{1}{s}, \tag{3.27}$$

and

$$R^+ = \alpha^+_{bw} L_f - r_f. \tag{3.28}$$

The inner loop R^+ in Equation 3.28 is determined such that the disturbance-rejection dynamics are as fast as the closed-loop set-point dynamics. Table 3.2 lists the calculated parameters of the positive-sequence controller for the E-STATCOM with parameters given in Appendix C.3. Figure 3.8 illustrates the control circuits of the positive-sequence current control.

Table 3.2 Controller parameters for positive-sequence current control

t_r^+ (ms)	α_{bw}^+ (rad/s)	k_p^+	k_i^+	R^+
4	550	0.233	128.38	0.232

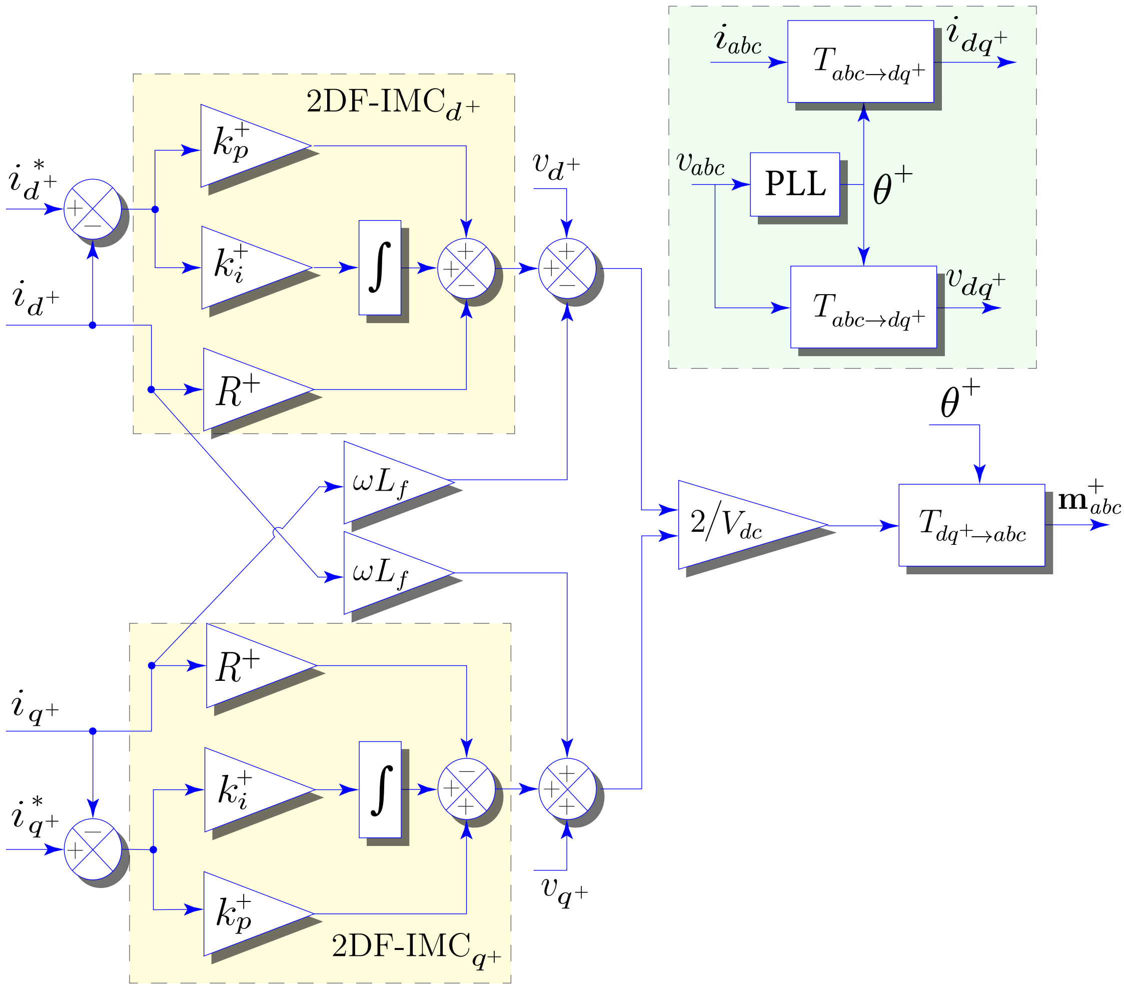

Figure 3.8 E-STATCOM positive-sequence current control.

Figure 3.9 presents the performance of the positive-sequence current control. Subfigures (a)–(c) illustrate the response to the i_d reference component, whereas (d)–(f) illustrate the response to the i_q reference component. Subplots (a) and (d) show the 10 kA reference step applied at 205 ms (black lines) and the corresponding feedback responses (blue lines) of the i_d and i_q components, respectively. When the positive-sequence current controller operates independently, the rise time (from 10 to 90%) of the final value, Δt, matches the t_r^+ value listed in Table 3.2, thereby confirming the proper tuning of the 2DF-IMC. Subplots (b) and (e) present the E-STATCOM output phase currents, while (c) and (f) display the sequence currents for i_d and i_q, respectively. The small delay observable in Subplots (c) and (f) can be attributed to (i) the delay introduced by the sequence-analysis algorithm and (ii) the triggering of the negative-sequence component.

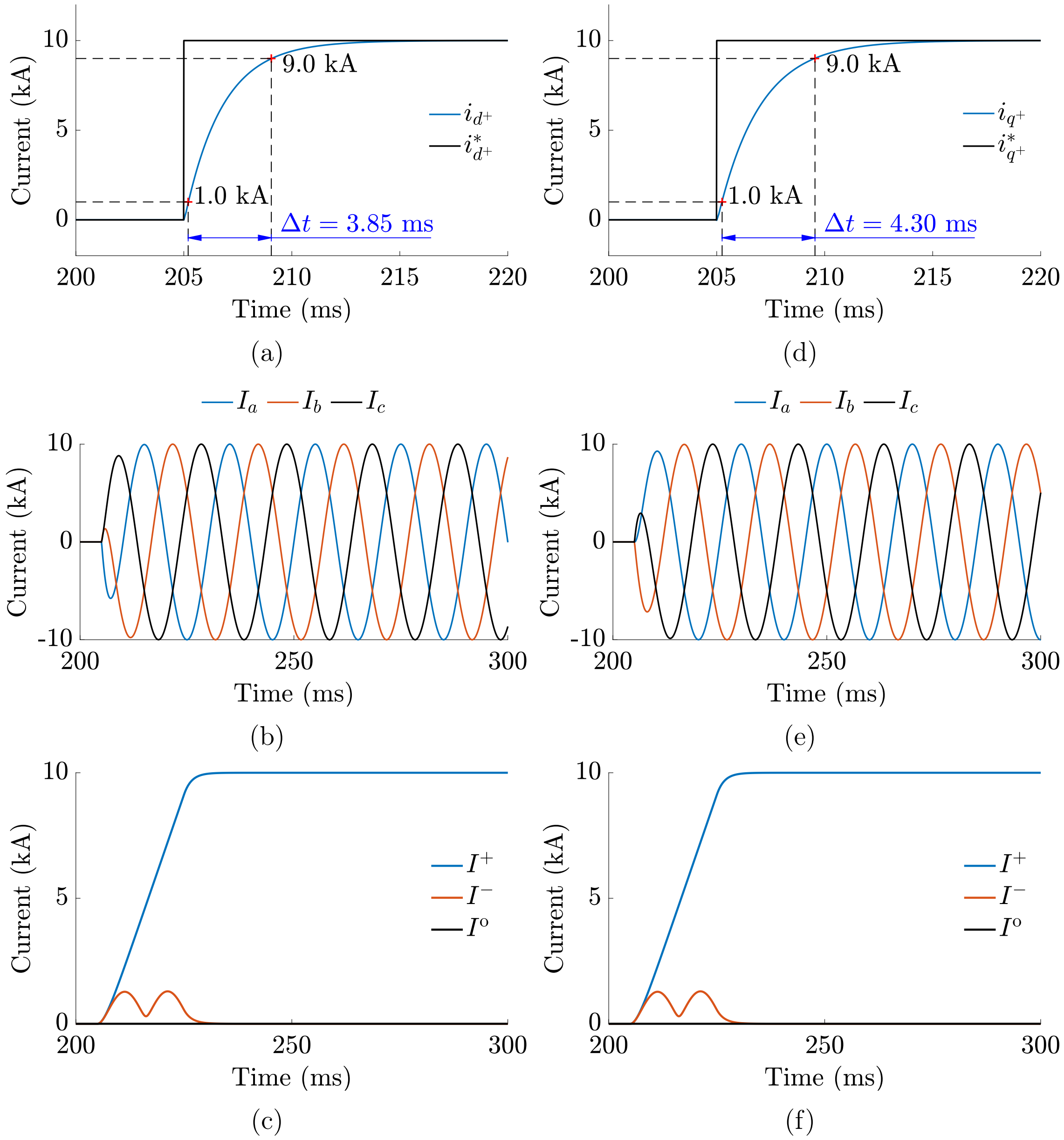

Figure 3.9 Injection of positive-sequence current. Subfigures (a)–(c) illustrate the response to the i_d reference component, whereas (d)–(f) illustrate the response to the i_q reference component. Specifically, (a) and (d) show the reference and measured currents, (b) and (e) present the phase currents, and (c) and (f) display the sequence component currents.

3.4.2 Negative-sequence current control

To achieve effective suppression of unbalanced components, the control of the negative-sequence current is developed in a manner analogous to that of the positive sequence. The governing equations are derived from Equation 3.14, whose negative-sequence form is expressed as

$$\begin{aligned} \frac{V_{dc}}{2} m_{d^-} - v_{d^-} &= r_f i_{fd^-} + L_f \frac{di_{fd^-}}{dt} - \omega L_f i_{fq^-}, \\ \frac{V_{dc}}{2} m_{q^-} - v_q^- &= r_f i_{fq^-} + L_f \frac{di_{fq^-}}{dt} + \omega L_f i_{fd^-}. \end{aligned} \tag{3.29}$$

Applying the Laplace transform to Equation 3.29 yields

$$\begin{aligned} \frac{i_{fd^-}(s)}{(V_{dc}/2)\, m_{d^-}(s) - v_{d^-}(s) + \omega L_f i_{fq^-}(s)} &= \frac{1}{L_f s + r_f}, \\ \frac{i_{fq^-}(s)}{(V_{dc}/2)\, m_{q^-}(s) - v_{q^-}(s) - \omega L_f i_{fd^-}(s)} &= \frac{1}{L_f s + r_f}. \end{aligned} \tag{3.30}$$

Since the feedforward compensation has already been introduced in the positive-sequence loop, the negative-sequence dynamics can be simplified as follows:

$$\begin{aligned} \frac{i_{fd^-}(s)}{m_{d^-}(s)} &= \frac{2}{V_{dc}} \frac{1}{L_f s + r_f}, \\ \frac{i_{fq^-}(s)}{m_{q^-}(s)} &= \frac{2}{V_{dc}} \frac{1}{L_f s + r_f}. \end{aligned} \tag{3.31}$$

The corresponding 2DF-IMC is then formulated as

$$F^-(s) = \alpha_{bw}^- L_f + \frac{\alpha_{bw}^-(r_f + R^-)}{s} = k_p^- + k_i^- \frac{1}{s}, \tag{3.32}$$

where the gain of the inner feedback loop is defined by

$$R^- = \alpha_{bw}^- L_f - r_f. \tag{3.33}$$

The parameters of the negative-sequence controller, computed according to the design procedure described earlier, are summarised in Table 3.3. These values ensure an appropriate trade-off between dynamic response and disturbance rejection.

Table 3.3 Controller parameters for negative-sequence current control

t_r^- (ms)	α_{bw}^- (rad/s)	k_p^-	k_i^-	R^-
8	275	0.117	32.10	0.115

The overall control structure implementing the negative-sequence current regulation is illustrated in Figure 3.10.

To evaluate the controller performance, the steady-state and transient responses of the negative-sequence currents are shown in Figure 3.11. Subfigures (a)–(c)

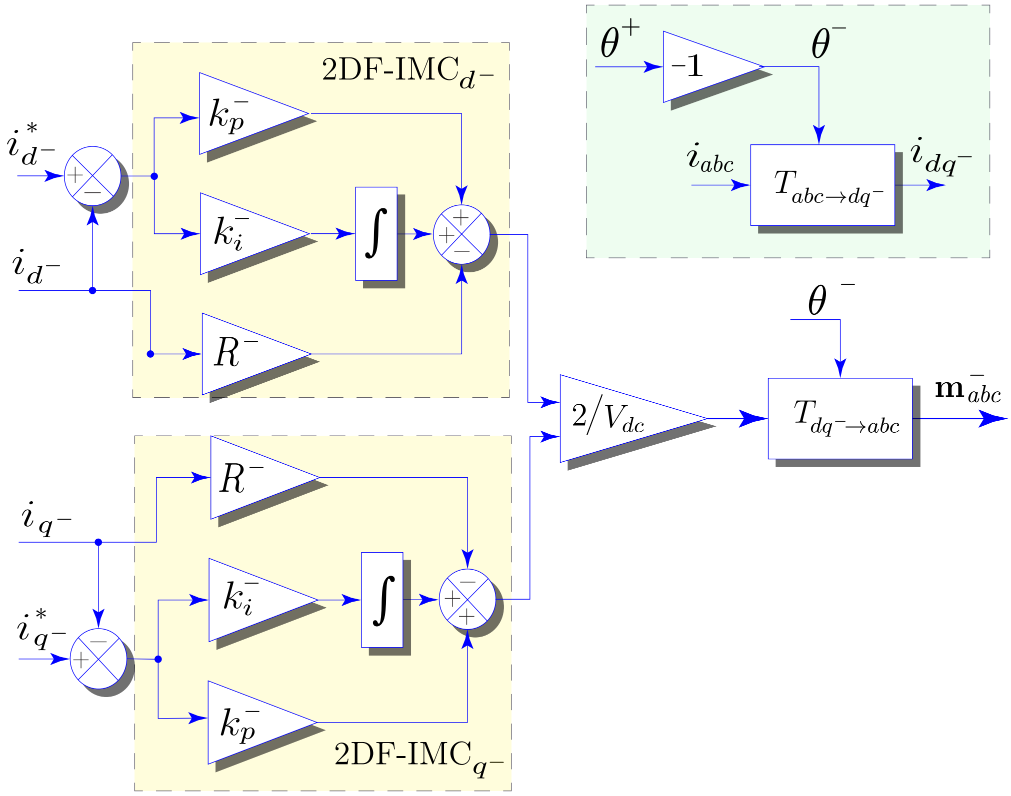

Figure 3.10 E-STATCOM negative-sequence current control.

illustrate the response to the i_d reference component, whereas (d)–(f) illustrate the response to the i_q reference component when the same reference as that used in the positive-sequence controller validation step (10 kA at 205 ms) is applied. The results demonstrate accurate reference tracking and effective injection of the negative-sequence current into the grid.

It is important to note that the negative- and positive-sequence controllers operate concurrently and therefore mutually influence each other. As a result, the rise time of the negative-sequence response in Subplots (a) and (d) does not precisely coincide with the t_r^- value listed in Table 3.3; nonetheless, the expected correlation remains evident. Subplots (b) and (e), which represent the E-STATCOM output phase currents, clearly exhibit the negative-sequence a–c–b phase order. Subplots (c) and (f) show the sequence currents, whose rise times correlate with those observed in Subplots (b) and (e) for the i_d and i_q reference components, respectively.

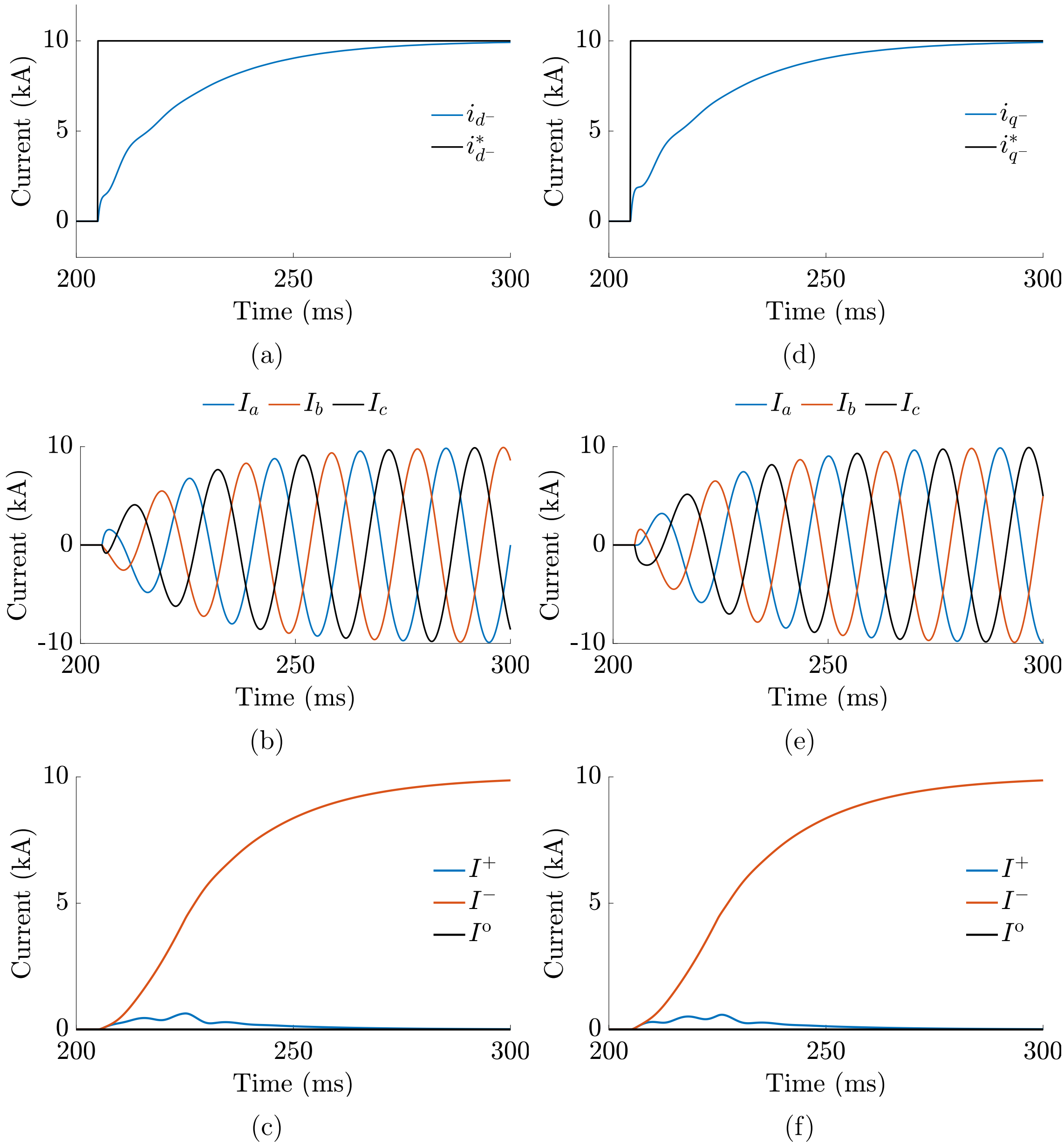

Figure 3.11 Injection of negative-sequence current. Subfigures (a)–(c) illustrate the response to the i_d reference component, whereas (d)–(f) illustrate the response to the i_q reference component. Specifically, (a) and (d) show the reference and measured currents, (b) and (e) present the phase currents, and (c) and (f) display the sequence-component currents.

3.4.3 Zero-sequence current control

By definition, the zero-sequence current is equal to the sum of the three phase currents:

$$i^{\mathrm{o}} = i_a + i_b + i_c. \tag{3.34}$$

To enable the use of the dq-based current control method, an orthogonal sinusoid is obtained by means of the All-Pass Filter (APF), expressed as

$$APF = \frac{\omega - s}{\omega + s}. \tag{3.35}$$

Following a procedure similar to that used for Equations 3.25 and 3.29, the zero-sequence voltage equation in the dq reference frame can be written as

$$\begin{aligned} \frac{V_{dc}}{2} m_d^{\text{o}} - v_d^{\text{o}} &= r_f i_{fd}^{\text{o}} + L_f \frac{di_{fd}^{\text{o}}}{dt} - \omega L_f i_{fq}^{\text{o}}, \\ \frac{V_{dc}}{2} m_q^{\text{o}} - v_q^{\text{o}} &= r_f i_{fq}^{\text{o}} + L_f \frac{di_{fq}^{\text{o}}}{dt} + \omega L_f i_{fd}^{\text{o}}. \end{aligned} \tag{3.36}$$

After applying the Laplace transform and eliminating the terms v_{dq}^{o} and $i_{fdq}^{\text{o}} \omega L_f$, the simplified transfer functions become

$$\begin{aligned} \frac{i_{fd}^{\text{o}}(s)}{m_d^{\text{o}}(s)} &= \frac{2}{V_{dc}} \frac{1}{L_f s + r_f}, \\ \frac{i_{fq}^{\text{o}}(s)}{m_q^{\text{o}}(s)} &= \frac{2}{V_{dc}} \frac{1}{L_f s + r_f}. \end{aligned} \tag{3.37}$$

Accordingly, the 2DF-IMC for the zero-sequence current control is defined as

$$F^{\text{o}}(s) = \alpha_{bw}^{\text{o}} L_f + \frac{\alpha_{bw}^{\text{o}}(r_f + R^{\text{o}})}{s} = k_p^{\text{o}} + k_i^{\text{o}} \frac{1}{s}, \tag{3.38}$$

where the gain of the inner feedback loop is given by

$$R^{\text{o}} = \alpha_{bw}^{\text{o}} L_f - r_f. \tag{3.39}$$

The computed parameters of the zero-sequence 2DF-IMC are summarised in Table 3.4.

Table 3.4 Controller parameters for zero-sequence current control

t_r^{o} (ms)	α_{bw}^{o} (rad/s)	k_p^{o}	k_i^{o}	R^{o}
8	275	0.117	32.10	0.115

The corresponding control structure implementing the zero-sequence current regulation is illustrated in Figure 3.12.

The steady-state and transient responses of the zero-sequence currents are shown in Figure 3.13 to assess the controller's dynamic performance. Subfigures (a)–(c) present the response of the i_d component, while (d)–(f) show the response of the

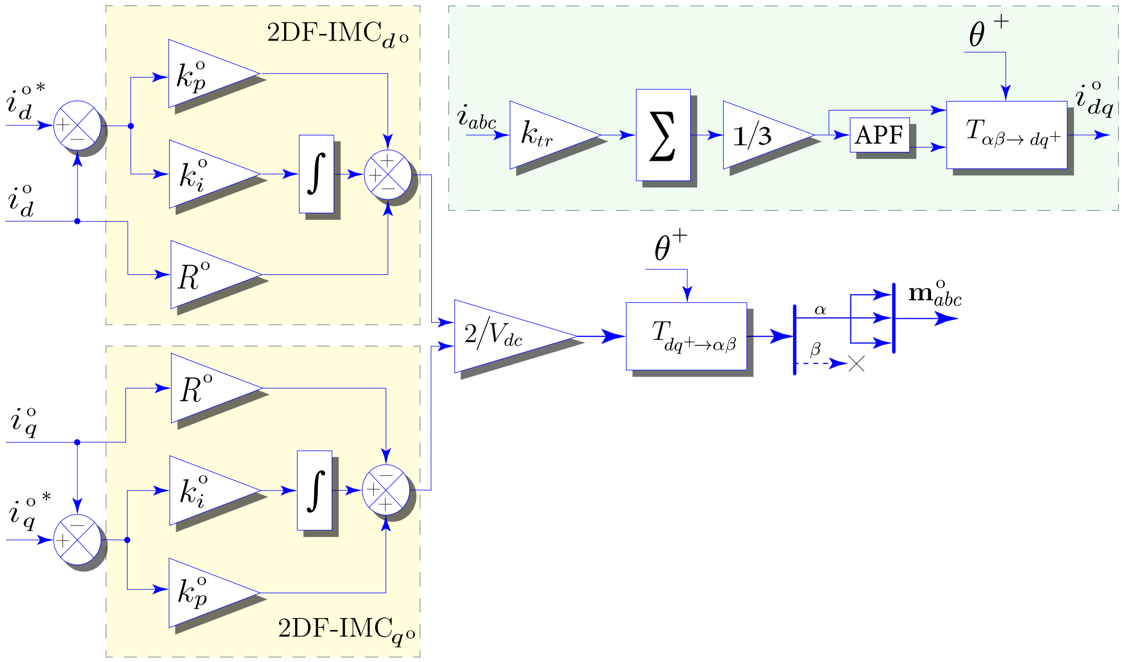

Figure 3.12 E-STATCOM zero-sequence current control.

i_q component, both obtained under the same reference conditions as those used for validating the other sequence controllers (step, 10 kA at 205 ms).

The small overshoot and oscillatory behaviour observed in Subplots (a) and (d) can be attributed to the highly sensitive nature of the zero-sequence current. Nevertheless, the error is eliminated within a short period (approximately 30 ms), and subsequent reference tracking remains accurate. The output phase currents of the E-STATCOM, shown in Subplots (b) and (e), overlap completely, confirming the pure zero-sequence current injection into the grid. Subplots (c) and (f) present the sequence currents, whose rise times correlate with those observed in Subplots (b) and (e) for the reference i_d and i_q components, respectively. The sequence components displayed in Subplots (c) and (f) also confirm the presence of pure zero-sequence current injection.

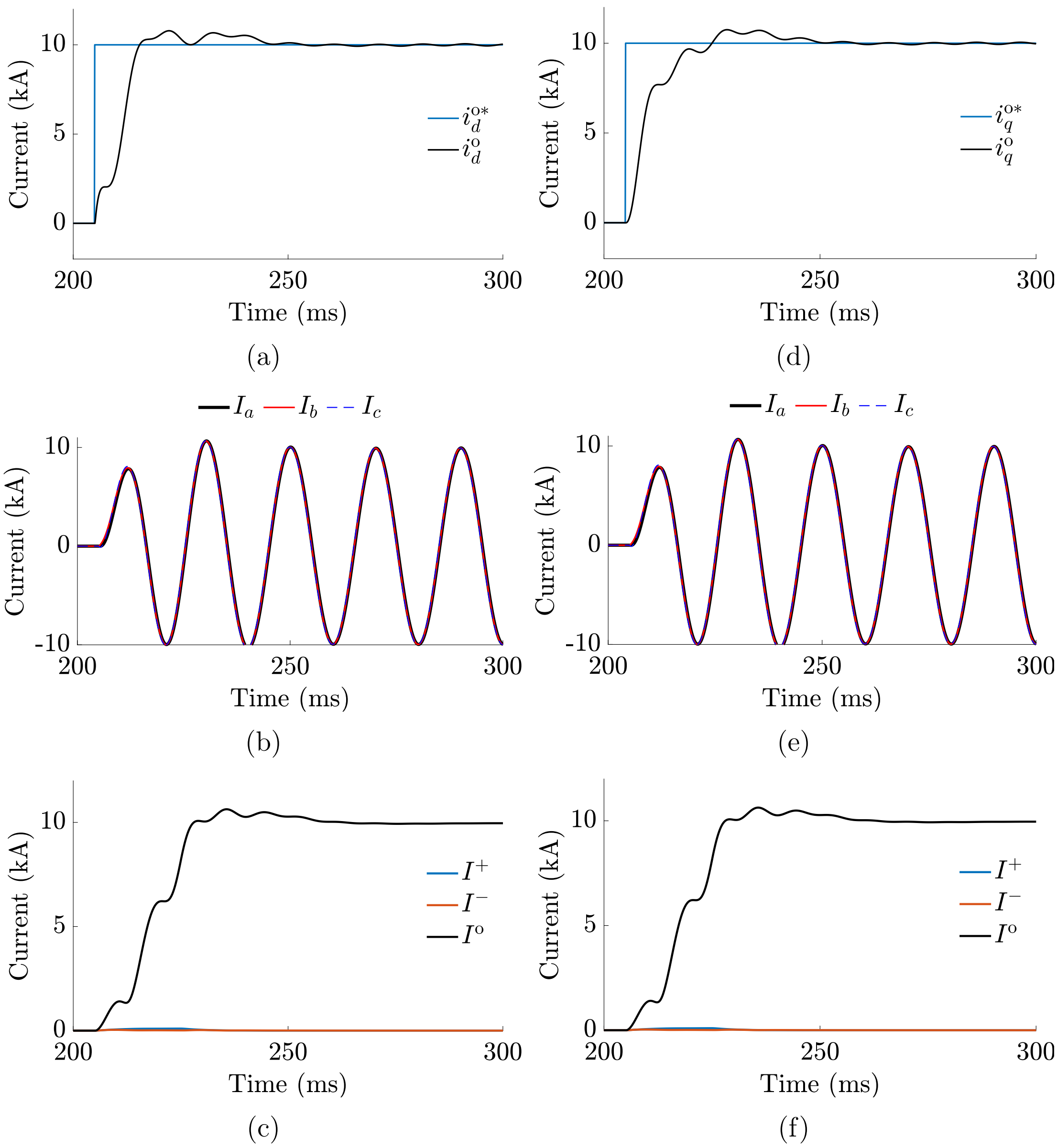

Figure 3.13 Injection of zero-sequence current. Subfigures (a)–(c) illustrate the response to the i_d^o reference component, whereas (d)–(f) illustrate the response to the i_q^o reference component. Specifically, (a) and (d) show the reference and measured currents, (b) and (e) present the phase currents, and (c) and (f) display the sequence component currents.

3.5 Current sequence-component 2DF-IMC filterless operation

To realise AO by suppressing current sequence components, all *dq*-sequence controllers operate in parallel. In this configuration, the zero-sequence *dq* controller regulates the common component using a feedback signal that contains only the zero-sequence part.

Therefore, it does not interact with the positive- or negative-sequence controllers and functions independently, so no further analysis of the zero-sequence control loop is required. In contrast, the positive- and negative-sequence controllers interact with each other as described below.

After the unfiltered signals are transformed through the Park transformation, as defined by Equations 3.21 and 3.22, the resulting quantities are applied to the respective 2DF-IMC controllers. In the steady state, when the sequence components are completely suppressed, the dc terms vanish, leaving only the ac components. Assuming a zero reference and according to Figure 3.8, the output of the positive-sequence 2DF–IMC dq controllers can be expressed as

$$\mathbf{u}_{dq}^{+} = \begin{bmatrix} i_{d^+}\, F_d^+ \\ i_{q^+}\, F_q^+ \end{bmatrix} = \begin{bmatrix} k_p^+\, i_{ac.d^+} + k_i^+ \int i_{ac.d^+}\, dt - R^+\, i_{ac.d^+} \\ k_p^+\, i_{ac.q^+} + k_i^+ \int i_{ac.q^+}\, dt - R^+\, i_{ac.q^+} \end{bmatrix} \tag{3.40}$$

The solution of Equation 3.40, omitting the intermediate calculations and taking into account the integrator control actions in the steady state, C_d^+ and C_q^+, is given as follows:

$$\mathbf{u}_{dq}^{+} = \begin{bmatrix} I_m^- M^+ \cos(\gamma_{dq^+} - \beta^+) + C_d^+ \\ -I_m^- M^+ \sin(\gamma_{dq^+} - \beta^+) + C_q^+ \end{bmatrix} \tag{3.41}$$

Where,

$$M^+ = \sqrt{(k_p^+ + R^+)^2 + \left(\frac{k_i^+}{2\omega}\right)^2}, \quad \gamma_{dq^+} = 2\omega t + \phi^-, \quad \beta^+ = \tan^{-1}\frac{k_i^+/(2\omega)}{k_p^+ + R^+}$$

This solution shows that the oscillating components i_{dAC}^+ and i_{qAC}^+, identified in Equation 3.21, propagate through the 2DF–IMC positive-sequence dq controllers, undergoing modifications in amplitude, by M^+, and in phase, by β^+.

Assuming a zero reference, and as illustrated in Figure 3.10, the steady-state output of the negative-sequence 2DF–IMC dq controllers is given by

$$\mathbf{u}_{dq^-} = \begin{bmatrix} i_{d^-}\, F_d^- \\ i_{q^-}\, F_q^- \end{bmatrix} = \begin{bmatrix} k_p^-\, i_{ac.d^-} + k_i^- \int i_{ac.d^-}\, dt - R^-\, i_{ac.d^-} \\ k_p^-\, i_{ac.q^-} + k_i^- \int i_{ac.q^-}\, dt - R^-\, i_{ac.q^-} \end{bmatrix} \tag{3.42}$$

Following the same procedure as for the positive-sequence case (Equation 3.41), and omitting the intermediate steps while considering the integrator control actions in the steady state, C_d^- and C_q^-, the negative-sequence controller output can be expressed as

$$\mathbf{u}_{dq}^{-} = \begin{bmatrix} -I_m^{+} M^{-} \cos(\gamma_{dq^-} - \beta^{-}) + C_d^{-} \\ -I_m^{+} M^{-} \sin(\gamma_{dq^-} - \beta^{-}) + C_q^{-} \end{bmatrix} \tag{3.43}$$

where

$$M^{-} = \sqrt{(k_p^{-} + R^{-})^2 + \left(\frac{k_i^{-}}{2\omega}\right)^2}, \quad \gamma_{dq^-} = 2\omega t + \phi^{+}, \quad \beta^{-} = \tan^{-1}\frac{k_i^{-}/(2\omega)}{k_p^{-} + R^{-}}.$$

This result indicates that the oscillating components $i_{ac.d^-}$ and $i_{ac.q^-}$, identified in the signals obtained from Equation 3.22, propagate through the 2DF–IMC negative-sequence dq controllers, undergoing changes in both amplitude, by M^{-}, and phase, by β^{-}.

If the feedforward compensation terms, v_{dq} and $i_{dq}\,\omega L$, are omitted to evaluate the overall performance of the system, Equations 3.41 and 3.43 are then transformed back to the abc domain from the dq^{+} and dq^{-} reference frames by using inverse Park transformations, $T^{-1}_{abc\to dq^+}$ and $T^{-1}_{abc\to dq^-}$. The transformed matrices can be split to two for the analysis purposes

$$\mathbf{u}_{abc}^{+} = T^{-1}_{abc\to dq^+}\,\mathbf{u}_{dq}^{+} = C_{dq}^{+}\begin{bmatrix} \cos(\theta - \delta^{+}) \\ \cos(\theta - \delta^{+} - 2\pi/3) \\ \cos(\theta - \delta^{+} + 2\pi/3) \end{bmatrix} - I_m^{-} M^{+} \begin{bmatrix} \sin(\theta + \phi^{-} - \beta^{+}) \\ \sin(\theta + \phi^{-} - \beta^{+} + 2\pi/3) \\ \sin(\theta + \phi^{-} - \beta^{+} - 2\pi/3) \end{bmatrix} \tag{3.44}$$

$$\mathbf{u}_{abc}^{-} = T^{-1}_{abc\to dq^-}\,\mathbf{u}_{dq}^{-} = C_{dq}^{-}\begin{bmatrix} \cos(\theta - \delta^{-}) \\ \cos(\theta - \delta^{-} + 2\pi/3) \\ \cos(\theta - \delta^{-} - 2\pi/3) \end{bmatrix} + I_m^{+} M^{-} \begin{bmatrix} \sin(\theta + \phi^{+} - \beta^{-}) \\ \sin(\theta + \phi^{+} - \beta^{-} + 2\pi/3) \\ \sin(\theta + \phi^{+} - \beta^{-} - 2\pi/3) \end{bmatrix} \tag{3.45}$$

Where, $\theta = \omega t$,

$$C_{dq}^{+} = \sqrt{(C_d^{+})^2 + (C_q^{+})^2}, \quad \text{and} \quad \delta^{+} = \tan^{-1}\frac{C_q^{+}}{C_d^{+}}$$

$$C_{dq}^{-} = \sqrt{(C_d^{-})^2 + (C_q^{-})^2}, \quad \text{and} \quad \delta^{-} = \tan^{-1}\frac{C_q^{-}}{C_d^{-}}$$

The signals $\mathbf{u}_{abc}^{+}$ and $\mathbf{u}_{abc}^{-}$ are, in fact, unscaled modulation signals (by a factor of $2/V_{dc}$). As seen from Equations 3.44 and 3.45, they contain both positive- and negative-sequence components. The positive-sequence *dq* controllers generate the intended positive-sequence *abc* signals through the integrator control action. However, because the input signal is unfiltered, negative-sequence components are also present and propagate through the controller, giving rise to additional *abc* signal components.

The negative-sequence controller, analogous to the positive-sequence one, produces both positive- and negative-sequence signals. Consequently, the remaining portion of the negative-sequence control action is produced by the integrators within the negative-sequence controller. The appearance of positive-sequence terms is attributed to the filterless nature of the input signal, which allows the positive-sequence components to propagate through the controller.

Therefore, each modulation signal comprises both positive- and negative-sequence components, whose superposition forms the overall modulation pattern required for the converter to generate the corresponding sequence components (with feedforward compensation). The described behaviour is illustrated in Figure 3.14.

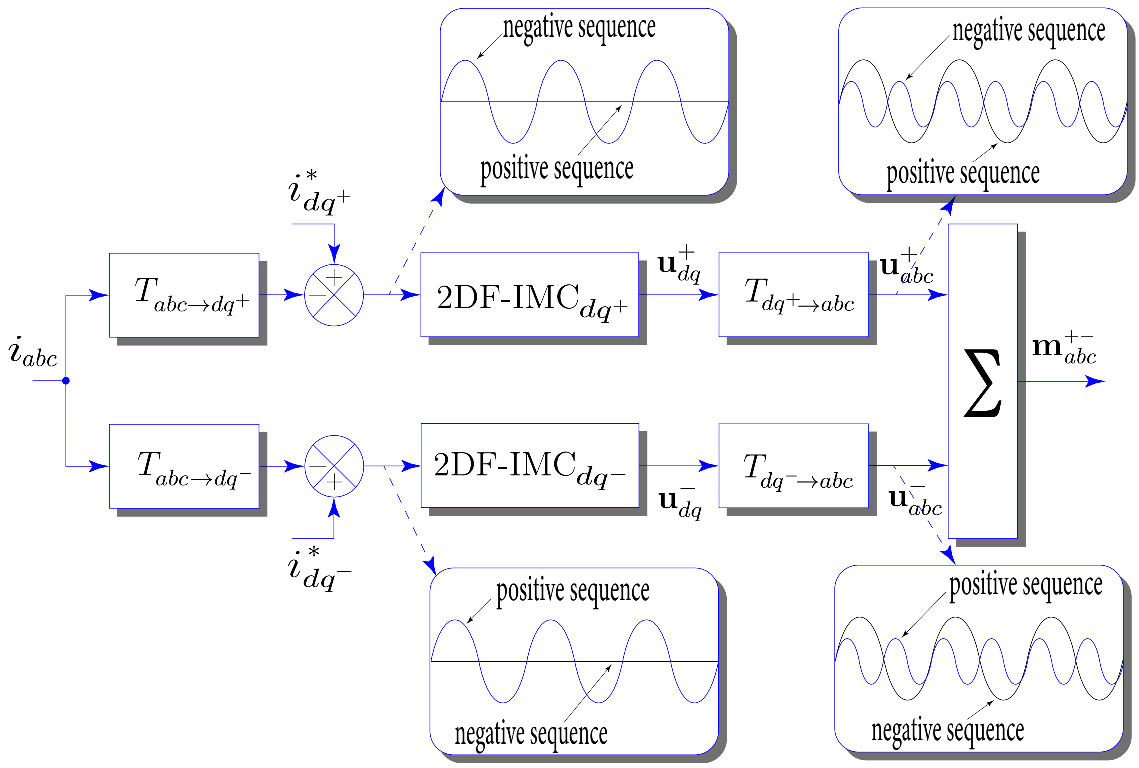

Figure 3.14 Filterless current control loops for the positive and negative sequences.

Overall, when filters are not employed and the signals are allowed to propagate, the positive- and negative-sequence controllers "see" and respond to disturbances originating from the opposite controller. In this case, the negative-sequence signal that passes through the positive-sequence *dq* controller, then through the plant, is interpreted by the negative-sequence *dq* controllers as a disturbance. Similarly, the positive-sequence signal that propagates through the negative-sequence dq controller and reaches the plant is perceived as a disturbance by the positive-sequence dq controllers. Since the disturbance propagates only through the feedback loop, this behaviour was validated by removing the reference input when forming the error signal. The current sequence components were suppressed in the same manner as when reference signals were applied.

As shown above, the propagating signals of the opposite sequence are also modified by the controllers and consequently participate in the control process. This interaction is an unavoidable characteristic arising from the parallel and simultaneous operation of the sequence controllers. However, this feature does not adversely affect the overall sequence-component suppression performance.

Comparison of PI and 2DF–IMC controllers for sequence suppression

A properly tuned PI controller has the same reference-tracking transfer function as the 2DF–IMC:

$$\frac{Y(s)}{R_{ef}(s)} = \frac{F(s)G(s)}{1+F(s)G(s)} = \frac{\alpha_{bw}}{s+\alpha_{bw}}. \tag{3.46}$$

Moreover, if it is used instead of the 2DF–IMC and the dq signals are left unfiltered, equations similar to Equations 3.44 and 3.45 can be derived. In this case, the opposite-sequence signals also propagate through the PI controller, albeit with certain modifications. The fast and efficient performance of the 2DF–IMC control, however, is primarily attributed to its superior disturbance-rejection capability, which is analysed below.

Considering the plant $G_p(s) = 1/(L_f s + r)$ under control, a PI controller tuned according to the technical optimum (pole–zero cancellation) can be expressed as

$$F_{PI}(s) = \frac{k_p s + k_i}{s} = \frac{\alpha_{bw}\,(L_f s + r_f)}{s}, \tag{3.47}$$

where α_{bw} sets the closed-loop dynamics. With unit feedback, the disturbance rejection transfer function becomes

$$\frac{Y(s)}{D(s)} = \frac{F_{PI}(s)\,G(s)}{1+F_{PI}(s)\,G(s)} = \frac{1}{L_f s + r_f}\,\frac{s}{s+\alpha_{bw}}. \tag{3.48}$$

For the 2DF–IMC, the disturbance rejection transfer function taking into account Equation 3.18 and 3.28 can be rewritten as

$$\frac{Y(s)}{D(s)} = \frac{F_{2DFIMC}(s)\,G(s)}{1+F_{2DFIMC}(s)\,G(s)} = \frac{1}{L_f s + (r_f + R)}\,\frac{s}{s+\alpha_{bw}} = \frac{1}{L_f(s+\alpha_{bw})}\,\frac{s}{s+\alpha_{bw}} \tag{3.49}$$

Since, for IBR systems, the Lr-connection link to the grid satisfies $\alpha_{bw} \gg r_f/L_f$, the pole in Equation 3.49 is located significantly further to the left on the complex plane than the pole of the transfer function in Equation 3.48. Therefore, the disturbance-rejection response of the 2DF–IMC controller is considerably faster than that of the conventional PI controller.

Figure 3.15 illustrates the performance of the 2DF–IMC and technically optimum PI controllers in suppressing the current sequence components for the E-STATCOM connected between the load and the grid, with the parameters shown in Table 3.5 (see Figure 3.6). The a-phase is opened at t_1, and the E-STATCOM is enabled at t_2. For the 2DF–IMC, it takes approximately 70 ms to suppress the sequence components, whereas the technically optimum PI controller requires several seconds to achieve the same effect.

In the context of AO of an TOPL, such response time is critical, since the equipment located at the substations at the TOPL extremities cannot remain connected for such an extended period while the asymmetry persists. Consequently, the asymmetry must be eliminated as rapidly as possible.

Table 3.5 Circuit parameters and measured current sequence components.

Voltage (kV)	V_{dc} (kV)	Load (MW)	t_1 (ms)	t_2 (ms)
20	50	700	100	205

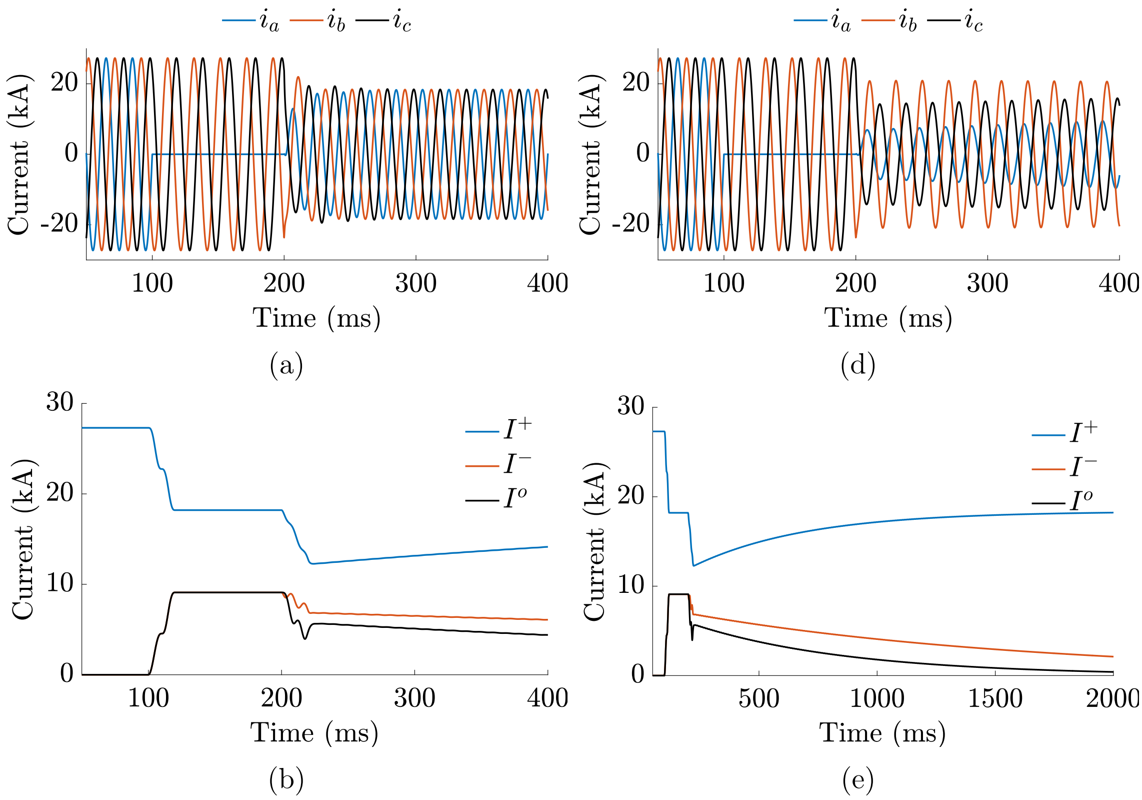

Figure 3.15 Performance of the 2DF–IMC and PI controllers. Subfigures (a) and (b) show the phase currents and the corresponding sequence components obtained using the 2DF–IMC controller, respectively. Subfigures (d) and (e) present the phase currents and sequence components obtained using the technically optimum PI controller, respectively.

3.6 Conclusion

This chapter has established the converter-level modelling and control framework required for fast mitigation of current sequence components using an E-STATCOM, with the specific objective of enabling AO as a practicable ancillary service.

First, an EMT-compatible, source-agnostic E-STATCOM representation was formulated using an average-value three-phase VSC model and an explicit dc-side energy source. The averaged VSC description captures the relevant electromagnetic time-scale dynamics without introducing switching-frequency artefacts, while the split dc-link (3L4W) configuration provides the structural means to suppress and control the zero-sequence current. The resulting grid-interface dynamics were expressed in the abc and synchronously rotating reference frame, leading to a first-order current plant with cross-coupling terms, which forms the basis for systematic controller synthesis. A lithium-ion battery model was then adopted as a representative DC power source; its role in this thesis is not bulk energy shifting, but the provision of a controllable active-power channel that supports sequence-current injection during AO transients.

Secondly, the 2DF–IMC concept was introduced and tailored to the E-STATCOM current plant. By explicitly shaping the disturbance-rejection pathway via the additional degree of freedom, the 2DF–IMC enables aggressive attenuation of disturbances in the dc domain whilst preserving robust set-point tracking. This property is essential in the present context because sequence-component control in the SRF is naturally formulated in terms of dc quantities, yet practical sequence detection introduces oscillatory terms (notably at twice the fundamental frequency) when signals are left unfiltered.

Thirdly, an SRF-based sequence detection method was detailed for positive- and negative-sequence currents, with analytical expressions demonstrating how the opposite sequence appears as a 2ω oscillation in the selected frame. This analysis motivated the filterless control philosophy adopted in the chapter: rather than reducing bandwidth through low-pass filtering to isolate dc components, the 2DF–IMC structure is leveraged to tolerate harmonic contamination while maintaining fast dynamic response.

On this basis, independent 2DF–IMC current controllers were designed for the positive-, negative-, and zero-sequence components, with appropriate feedforward compensation to decouple known voltage and cross-coupling terms. The parallel operation of the sequence loops and the superposition of modulation signals were formalised, and the inevitable interaction between the positive- and negative-sequence loops under filterless operation was shown to be benign with respect to overall suppression performance. Finally, a comparative assessment against a technically optimum PI controller demonstrated that the principal advantage of the proposed approach lies in disturbance rejection: for the same nominal closed-loop tracking dynamics, the 2DF–IMC achieves substantially faster elimination of sequence components (order-of-tens-of-milliseconds in the demonstrated case), whereas the PI-based solution may require seconds, which is incompatible with AO protection and equipment withstand constraints.

The control framework developed here is converter-centric and intentionally generalisable to any VSC-based IBR that can exchange active power via a physical dc source. However, the required sequence-current references, the achievable mitigation performance, and the resulting stresses on substation and line equipment depend fundamentally on the network model to which the E-STATCOM is connected. In particular, AO studies are sensitive to: (i) unbalanced series coupling between phase and shield/earth return paths, and (ii) the distribution and circulation of zero-sequence current along the OPL, neither of which is captured adequately by the simple π-section model representation commonly adopted in prior AO work.

Accordingly, Chapter 4 develops a three-phase simulation OPL model suitable for AO analysis, including a rigorous treatment of self and mutual impedances (with explicit consideration of earth return and the influence of ground/shield conductors). This enhanced plant representation provides the electrical environment in which the sequence-component controllers designed in Chapter 3 will be deployed. The combination of (i) fast, filterless sequence-current control at the terminals and (ii) an AO-capable line model enables meaningful assessment of the technical applicability of AO, zero-sequence current pathways, and mitigation requirements under realistic EHV conditions in the subsequent analysis and case studies.

Chapter 4

Development and Analysis of a Three-Phase Power Line Simulation Model for AO

4.1 Introduction

As highlighted in [59], modelling AO requires the development of a power line model capable of capturing unbalanced operation and zero-sequence current distribution. The latter is not a straightforward matter. For example, during the 1970s and 1980s, substantial research efforts were devoted by the electrical engineering research community to the analysis of short-circuit current distribution under single-phase-to-ground fault conditions, leading to valuable insights [60–63]. Addressing this issue was essential for the design of substation grounding systems, safety assessments, and other critical applications.

To date, AO modelling has commonly relied on the simple π-circuit model [24], which is inadequate for analysing zero-sequence current distribution. More broadly, its suitability as a representative OPL model for simulating AO conditions remains questionable.

This chapter provides a concise theoretical foundation for the derivation of power line impedance, presents a detailed formulation of the full OPL model for AO analysis developed in this thesis, and discusses its benefits and limitations.

4.2 Theoretical basis

4.2.1 OPL series impedance

The inductive reactance, encompassing both self and mutual components, is intrinsically dependent on the total magnetic fields enveloping a given conductor. As illustrated in Figure 4.1, conductors numbered *1* through n generate magnetic flux lines as a consequence of the currents passing through them.

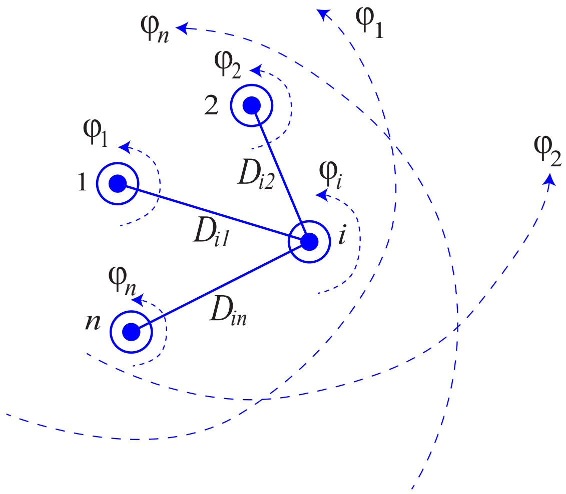

Figure 4.1 OPL wires magnetic field.

If the total sum of currents flowing through conductors from the first to the n-th wire equals zero, the total magnetic flux linked to conductor i can be formulated as follows:

$$\lambda_i = N \cdot \Phi = 2 \times 10^{-7} \cdot \left(I_1 \ln \frac{1}{D_{i1}} + I_2 \ln \frac{1}{D_{i2}} + \cdots + I_i \ln \frac{1}{\mathrm{GMR}_i} + \cdots + I_n \ln \frac{1}{D_{in}} \right) \tag{4.1}$$

where GMR_i is the geometric mean radius of conductor i.

The inductance of conductor i comprises two components: the self-inductance of conductor i and the mutual inductance between conductor i and the remaining $n-1$ conductors. According to its formal definition,
self-inductance:

$$L_{ii} = \frac{\lambda_{ii}}{I_i} = 2 \cdot 10^{-7} \cdot ln \frac{1}{GMR_i} \tag{4.2}$$

mutual inductance:

$$L_{in} = \frac{\lambda_{in}}{I_n} = 2 \cdot 10^{-7} \cdot ln\frac{1}{D_{in}}. \tag{4.3}$$

In practical applications, particularly for EHV power lines, simplified models are often employed for steady-state operation simulations, such as power flow analyses. These simplifications involve combining the mutual and self-inductances. Consequently, Equations 4.2 and 4.3 are merged to yield the phase inductance, as expressed in Equation 4.4.

$$L_i = 2 \cdot 10^{-7} \cdot ln\frac{D_{eq}}{GMR_i} \tag{4.4}$$

where

$$D_{\text{eq}} = \sqrt[3]{D_{ab} \cdot D_{bc} \cdot D_{ca}} \tag{4.5}$$

This approach is based on the following assumptions:

1. The power line is fully transposed (depending on its length).
2. The phases are equally loaded.
3. Three phase voltages and currents are balanced.

In general, these assumptions hold true for EHV transmission power lines. However, if an untransposed power line is considered or if a power line operates in AO, alternative methods must be employed. Three fundamental methodologies—Carson's, Rüdenberg's, and Deri's—are employed for determining the series impedance of power transmission lines while accounting for the influence of the ground. These approaches diverge based on the configuration of the conductors and the electrical characteristics of the ground [64–66]. A common assumption across all three theories is that the highest density of alternating current within the ground is concentrated directly beneath the transmission line, diminishing rapidly both laterally and with depth. Furthermore, each method treats the ground as a conductive medium with its own intrinsic electrical parameters, implying that its series impedance is non-zero [67].

The pioneering and still widely used Carson's equations were developed in 1926 [64]. This method is based on analysing a single phase and its return path through the ground, which is represented as the 'image' of the original wire, as shown in Figure 4.2. The image is located at the same distance below the ground surface as the wire's height above it and has the same diameter.

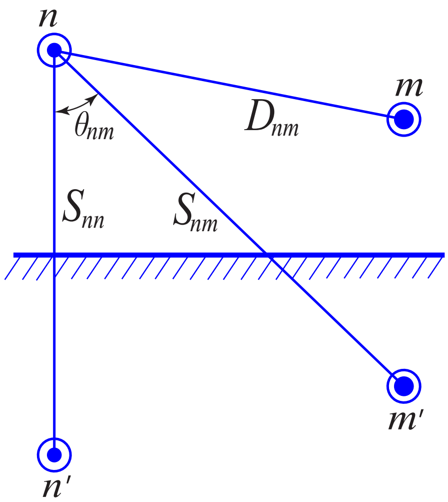

Figure 4.2 Conductors and images

Using this approach, the author solves in [64] the wave integral given in Equation 4.6 through an infinite series expansion. The explicit derivation of Equation 4.6 and an analysis of the underlying assumptions are provided in [68].

$$E_z = -\int_0^\infty F(\mu_{cr})\,\cos(x\mu_{cr})\,e^{y\sqrt{\mu_{cr}^2+\mathrm{j}\alpha_{cr}}}\,d\mu_{cr}, \qquad y \leq 0 \tag{4.6}$$

Equation 4.6 is developed based on the assumptions originally presented by Wise in [69]:

1. The Earth's relative permeability is unity.
2. The wave propagates at the speed of light without attenuation.
3. The frequency is sufficiently low such that polarisation currents can be neglected.

Although Equation 4.6 was originally solved using an infinite series expansion, in practical applications only the first few terms are typically retained, as they provide a sufficiently accurate solution. Moreover, [70] demonstrates that the modified, simplified form of Carson's equations yields a fidelity within 1% error when applied to ground resistivity values in the range of 10 Ω m to 1000 Ω m. Consequently, the solution to Equation 4.6 can be expressed in terms of self and mutual impedances as follows:

$$Z_{ii} = r_i + 4\omega\sigma_{ii}G + j\Big(X_i + 2\omega G\cdot\ln\frac{S_{ii}}{RD_i} + 4\omega\eta_{ii}G\Big) \quad \Omega/\mathrm{km} \tag{4.7}$$

$$Z_{ij} = 4\omega\sigma_{ij}G + j\Big(2\omega G \cdot \ln\frac{S_{ij}}{D_{ij}} + 4\omega\eta_{ij}G\Big) \quad \Omega/\text{km} \tag{4.8}$$

$$X_i = 2\omega G \cdot \ln\frac{R_{Di}}{\text{GMR}_i} \quad \Omega/\text{km} \tag{4.9}$$

$$\sigma_{ij} = \frac{\pi}{8} - \frac{1}{\sqrt{3}}k_{ij}\cos(\theta_{ij}) + \frac{k_{ij}^2}{16}\cos(2\theta_{ij}) \cdot \Big(0.6728 + \ln\frac{2}{k_{ij}}\Big) \tag{4.10}$$

$$\eta_{ij} = -0.386 + \frac{1}{2} \cdot \ln\frac{2}{k_{ij}} + \frac{1}{\sqrt{3}}k_{ij}\cos(\theta_{ij}) \tag{4.11}$$

$$k_{ij} = 8.565 \times 10^{-4} \cdot S_{ij} \cdot \sqrt{\frac{f}{\rho}} \tag{4.12}$$

Equations 4.7-4.12 result in the impedance matrix 4.13, which represents a system comprising *1* to n phases and *g1* to *gm* ground or shield wires.

$$\mathbf{Z} = \left[\begin{array}{ccc|ccc} Z_{11} & \dots & Z_{1n} & Z_{1g1} & \dots & Z_{1gm} \\ \vdots & \ddots & \vdots & \vdots & \ddots & \vdots \\ Z_{n1} & \dots & Z_{nn} & Z_{ng1} & \dots & Z_{ngm} \\ \hline Z_{g11} & \dots & Z_{g1n} & Z_{g1g1} & \dots & Z_{g1m} \\ \vdots & \ddots & \vdots & \vdots & \ddots & \vdots \\ Z_{gm1} & \dots & Z_{gmn} & Z_{mg1} & \dots & Z_{gmgm} \end{array}\right], \quad \mathbf{Z} \in \mathbb{C}^{(n+m)\times(n+m)} \tag{4.13}$$

Equation 4.12 quantifies the effect of ground resistivity, ρ, on power line impedance, which is particularly relevant when analysing AO.

The subsequent step in common practice involves reducing the rows and columns corresponding to the ground wire(s). This is achieved by applying Kron reduction to the impedance matrix, $\mathbf{Z}$ (4.13), to reduce it to $n \times n$ size. Such an approach is logical, as considering the circuit depicted in Figure 4.3 for a three phase power line with a ground wire leads to the derivation of Equation 4.14. For a three-phase power

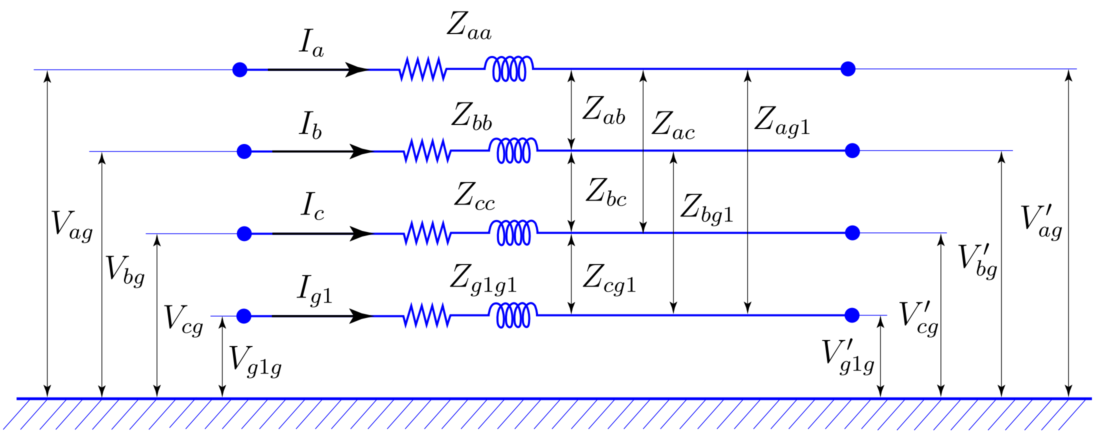

Figure 4.3 Three-phase with one ground wire line segment

line segment with one ground wire *g1*

$$\begin{bmatrix} V_{ag} \\ V_{bg} \\ V_{cg} \\ V_{g1g} \end{bmatrix} = \begin{bmatrix} V'_{ag} \\ V'_{bg} \\ V'_{cg} \\ V'_{g1g} \end{bmatrix} + \begin{bmatrix} Z_{aa} & Z_{ab} & Z_{ac} & Z_{ag1} \\ Z_{ba} & Z_{bb} & Z_{bc} & Z_{bg1} \\ Z_{ca} & Z_{cb} & Z_{cc} & Z_{cg1} \\ Z_{g1a} & Z_{g1b} & Z_{g1c} & Z_{g1g1} \end{bmatrix} \begin{bmatrix} I_a \\ I_b \\ I_c \\ I_{g1} \end{bmatrix} \tag{4.14}$$

The further rearrangement of Equation 4.14 yields

$$\begin{bmatrix} \mathbf{V}_{abc} \\ \mathbf{V}_{g1} \end{bmatrix} = \begin{bmatrix} \mathbf{V'}_{abc} \\ \mathbf{V'}_{g1} \end{bmatrix} + \begin{bmatrix} \mathbf{Z}_{ij} & \mathbf{Z}_{ig1} \\ \mathbf{Z}_{g1j} & \mathbf{Z}_{g1g1} \end{bmatrix} \begin{bmatrix} \mathbf{I}_{abc} \\ \mathbf{I}_{g1} \end{bmatrix} \tag{4.15}$$

Hence,

$$\mathbf{V}_{abc} = \mathbf{V'}_{abc} + \mathbf{Z}_{ij}\mathbf{I}_{abc} + \mathbf{Z}_{ig1}\mathbf{I}_{g1} \tag{4.16}$$

and, assuming that the shield wire(s) are grounded, $\mathbf{V}_{g1} = \mathbf{V'}_{g1} = \mathbf{0}$. Solving Equation 4.15 for $\mathbf{I}_{g1}$ gives

$$\mathbf{I}_{g1} = -\mathbf{Z}_{g1g1}^{-1}\mathbf{Z}_{g1j}\mathbf{I}_{abc} \tag{4.17}$$

This methodology differs from that presented in classical power system analysis textbooks, such as [71], where the voltage matrix equation is typically formulated with reference to the 'neutral/ground' conductor. Rather Equation (4.18) is derived with reference to Figure 4.4, under the assumption that $I_{g1} = -(I_a+I_b+I_c)$. Consequently, the dimensionality of the impedance matrix in Equation (4.18) matches the number of phase conductors, and although the neutral current does not appear explicitly, the impedance of the neutral wire is inherently embedded within the matrix elements, thereby influencing the overall voltage drop equations.

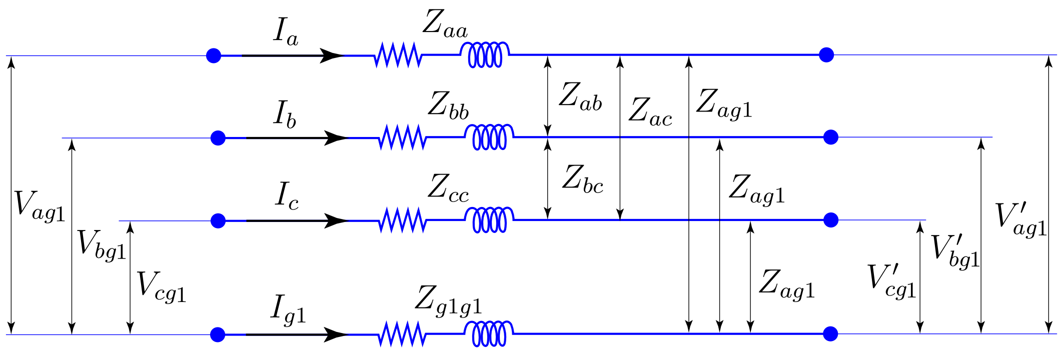

Figure 4.4 Three-phase with one ground wire segment.

It is important to note that the impedance matrix in Equation (4.18) is not equivalent to that in Equation (4.14), as the voltage formulations differ between the two approaches.

$$\begin{bmatrix} V_{ag1} \\ V_{bg1} \\ V_{cg1} \end{bmatrix} = \begin{bmatrix} V'_{ag1} \\ V'_{bg1} \\ V'_{cg1} \end{bmatrix} + \begin{bmatrix} Z_{aa}+Z_{g1g1}-2Z_{ag1} & Z_{ab}+Z_{g1g1}-2Z_{ag1} & Z_{ac}+Z_{g1g1}-2Z_{ag1} \\ Z_{ba}+Z_{g1g1}-2Z_{bg1} & Z_{bb}+Z_{g1g1}-2Z_{bg1} & Z_{bc}+Z_{g1g1}-2Z_{bg1} \\ Z_{ca}+Z_{g1g1}-2Z_{cg1} & Z_{cb}+Z_{g1g1}-2Z_{cg1} & Z_{cc}+Z_{g1g1}-2Z_{cg1} \end{bmatrix} \begin{bmatrix} I_a \\ I_b \\ I_c \end{bmatrix} \tag{4.18}$$

A further simplification of the impedance matrix, following Kron reduction in Equation (4.14) or Equation (4.18), can be achieved by assuming equal self- and mutual impedances; that is, $Z_s = Z_{aa} = Z_{bb} = Z_{cc}$ and $Z_m = Z_{ab} = Z_{ba} = Z_{bc} = Z_{cb} = Z_{ac} = Z_{ca}$. The notation, together with the subsequent rearrangement, yields Equation (4.19). The equal self- and mutual-impedance assumptions are generally valid for fully transposed and symmetrically constructed overhead lines.

$$\begin{bmatrix} V_{ag1} - V'_{ag1} \\ V_{bg1} - V'_{bg1} \\ V_{cg1} - V'_{cg1} \end{bmatrix} = \begin{bmatrix} Z_s & Z_m & Z_m \\ Z_m & Z_s & Z_m \\ Z_m & Z_m & Z_s \end{bmatrix} \begin{bmatrix} I_a \\ I_b \\ I_c \end{bmatrix} \tag{4.19}$$

In the case of an untransposed OPL, the impedance matrix remains symmetrical; however, the main diagonal and off-diagonal elements are not equal.

Here, the impedance matrix has equal diagonal elements and identical off-diagonal elements, reflecting the assumed symmetry.

Thus, owing to the differences in the voltage formulations in Equations 4.14 and 4.18, the resulting impedance matrices are not identical. It is also important to note that, in practice, perfect symmetry of a transmission line is unattainable—even under the outlined assumptions—owing to inherent asymmetries in the resistance, inductance, and capacitance matrices. Further sources of asymmetry in OPL parameters include environmental factors (such as weather-induced variability and non-uniform soil resistivity) and structural differences arising from tower geometry. Nonetheless, these influences fall outside the scope of the present thesis and are therefore excluded from the subsequent analysis.

4.3 Full TOPL simulation model

If the zero-sequence currents are to be assessed, none of the methods provided in Subsection 4.2.1 are appropriate, as they involve a reduced impedance matrix and do not treat the ground wire(s) as separate conductors. Therefore, the full (unreduced) impedance matrix must be employed when AO is used.

In this thesis, the OPL under consideration is a long-length (300km), fully transposed extra-high voltage (EHV, 500kV) line. The modelling approach involves calculating the impedance matrix and manually implementing the transposition within the simulation model developed in MATLAB&Simulink.

For a 500kV transmission power line with two ground wires, the impedance matrix is expressed as:

$$\mathbf{Z} = \begin{bmatrix} Z_{aa} & Z_{ab} & Z_{ac} & Z_{ag1} & Z_{ag2} \\ Z_{ba} & Z_{bb} & Z_{bc} & Z_{bg1} & Z_{bg2} \\ Z_{ca} & Z_{cb} & Z_{cc} & Z_{cg1} & Z_{cg2} \\ Z_{g1a} & Z_{g1b} & Z_{g1c} & Z_{g1g1} & Z_{g1g2} \\ Z_{g2a} & Z_{g2b} & Z_{g2c} & Z_{g2g1} & Z_{g2g2} \end{bmatrix}, \quad \mathbf{Z} \in \mathbb{C}^{5\times5} \tag{4.20}$$

The impedance matrix, $\mathbf{Z}$, can be expressed as the sum of two matrices, as provided by certain power line parameter calculation tools such as MATLAB&Simulink [72]:

$$\mathbf{Z} = \mathbf{R} + j\omega\mathbf{L}, \quad \mathbf{R}, \mathbf{L} \in \mathbb{R}^{5\times5} \tag{4.21}$$

This matrix along with capacitance matrix can represent a model of a power line segment to simulate AO. Figure 4.5 represents full TOPL simulation model (full model), and its segment impedance circuit is shown in Figure 4.6.

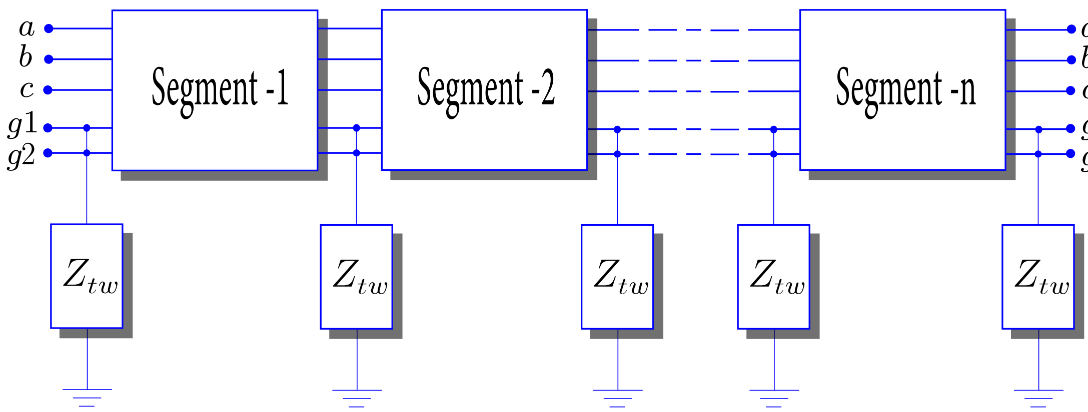

Figure 4.5 Full TOPL simulation model.

The standard suspension tower used in 500kV OPL in Kazakhstan is depicted in Figure 4.7. The structural dimensions of this tower conform to regional transmission requirements. Additional relevant parameters, including conductor and ground wire specifications are provided in the Appendix (Table C.10), and the formulae for calculating OPL capacitance can be found in [71, 73].

To determine the electrical parameters of the 500kV transmission power line, the built-in power line parameter calculation tool in MATLAB&Simulink was utilised [72]. This tool was validated and subsequently employed to generate the capacitance, inductance, and resistance matrices for the given transmission system. During

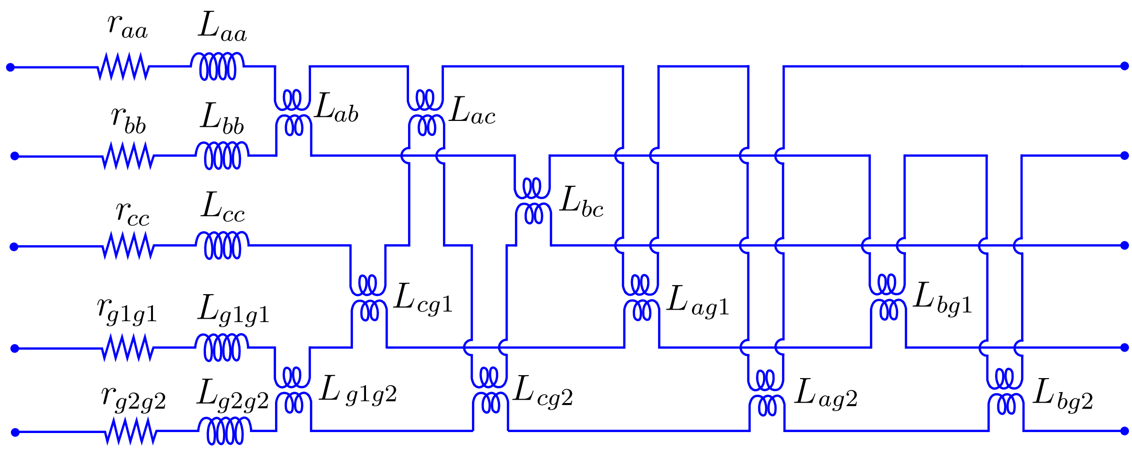

Figure 4.6 Segment impedance circuit of the full TOPL simulation model.

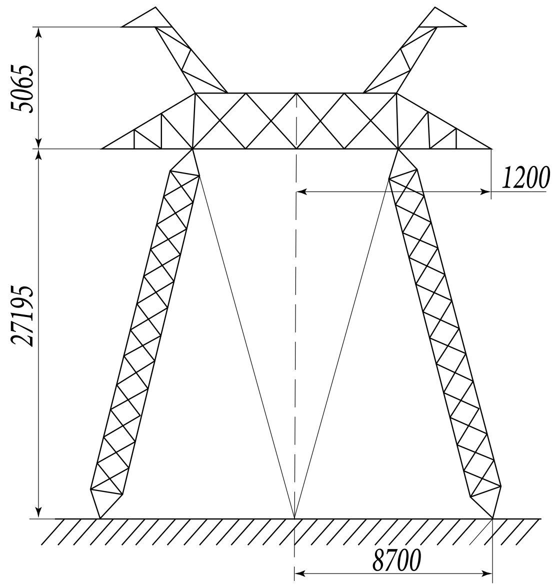

Figure 4.7 Standard suspension tower for a 500kV OPL in Kazakhstan.

validation, it was found that the MATLAB tools in fact employ the short form of Carson's equations. The computed matrices are presented below.

$$\mathbf{C} = \begin{bmatrix} 10.8397 & -2.4062 & -0.8318 & -1.4677 & -0.4428 \\ -2.4062 & 11.2345 & -2.4062 & -0.7883 & -0.7883 \\ -0.8318 & -2.4062 & 10.8397 & -0.4428 & -1.4677 \\ -1.4677 & -0.7883 & -0.4428 & 6.4611 & -0.4017 \\ -0.4428 & -0.7883 & -1.4677 & -0.4017 & 6.4611 \end{bmatrix} \text{nF/km} \tag{4.22}$$

$$\mathbf{L} = \begin{bmatrix} 1.8034 & 0.9475 & 0.8089 & 0.9138 & 0.7564 \\ 0.9475 & 1.8034 & 0.9475 & 0.8344 & 0.8344 \\ 0.8089 & 0.9475 & 1.8034 & 0.7564 & 0.9138 \\ 0.9138 & 0.8344 & 0.7564 & 2.4322 & 0.7503 \\ 0.7564 & 0.8344 & 0.9138 & 0.7503 & 2.4322 \end{bmatrix} \text{ mH/km} \tag{4.23}$$

$$\mathbf{R} = \begin{bmatrix} 0.07623 & 0.04702 & 0.04699 & 0.04655 & 0.04651 \\ 0.04702 & 0.07624 & 0.04702 & 0.04654 & 0.04654 \\ 0.04699 & 0.04702 & 0.07623 & 0.04651 & 0.04655 \\ 0.04655 & 0.04654 & 0.04651 & 0.55512 & 0.04605 \\ 0.04651 & 0.04654 & 0.04655 & 0.04605 & 0.55512 \end{bmatrix} \Omega\text{/km} \tag{4.24}$$

4.4 π-section sequence model of OPL

In accordance with common practice, a power line model requires the application of Kron, as it was mentioned earlier, reduction to the impedance matrix. Accordingly, the resistance and inductance matrices given in Equations 4.24 and 4.23 are reduced to 3×3 form using Kron reduction. For the capacitance matrix, however, it is sufficient to extract the relevant 3×3 submatrix corresponding to the phase conductors.

$$\mathbf{R}_{sym} = \begin{bmatrix} 0.10041 & 0.07000 & 0.06886 \\ 0.07000 & 0.09918 & 0.07000 \\ 0.06886 & 0.07000 & 0.10041 \end{bmatrix} \Omega\text{/km} \tag{4.25}$$

$$\mathbf{L}_{sym} = \begin{bmatrix} 1.4192 & 0.5674 & 0.4323 \\ 0.5674 & 1.4236 & 0.5674 \\ 0.4323 & 0.5674 & 1.4192 \end{bmatrix} \text{ mH/km} \tag{4.26}$$

$$\mathbf{C}_{sym} = \begin{bmatrix} 10.8397 & -2.4062 & -0.8318 \\ -2.4062 & 11.2345 & -2.4062 \\ -0.8318 & -2.4062 & 10.8397 \end{bmatrix} \text{ nF/km} \tag{4.27}$$

Due to fully transposed symmetrical OPL is considered, the π-section sequence model can be represented by the positive- and zero-sequence components developed from $\mathbf{R}_{sym}$, $\mathbf{L}_{sym}$, $\mathbf{C}_{sym}$ matrices:

$$\mathbf{r}^{+o} = \begin{bmatrix} 0.03038 & 0.23924 \end{bmatrix} \quad \Omega/\text{km} \tag{4.28}$$

$$\mathbf{l}^{+o} = \begin{bmatrix} 0.8983 & 2.4654 \end{bmatrix} \quad \text{mH/km} \tag{4.29}$$

$$\mathbf{c}^{+o} = \begin{bmatrix} 12.8527 & 7.2085 \end{bmatrix} \quad \text{nF/km} \tag{4.30}$$

4.5 Simplified π-section model

A transmission-line phase can be represented using a decoupled single-phase π-section circuit, where the mutual inductances, resistances, and capacitances are neglected. This model was proposed by A. Sana and R. Marceau in [2, 9, 23, 24] for power lines AO investigations. Figure 4.8 shows the corresponding circuit, and the parameters can be calculated as follows.

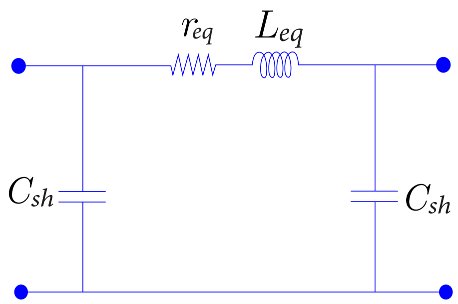

Figure 4.8 π-section circuit of a power line.

$$Z = r_{eq} + j\omega L_{eq}, \qquad Y_{sh} = j\omega C_{sh}$$

Propagation constant and surge impedance:

$$\gamma_{pr} = \sqrt{Z\,Y_{sh}}, \qquad Z_c = \sqrt{\frac{Z}{Y_{sh}}}$$

For half of a 300 km transmission line, $\gamma_{pr} l \approx 0.00861 + j0.16$. The $ABCD$ parameters with hyperbolic (long line) corrections are therefore

$$A = \cosh(\gamma_{pr} l), \qquad B = Z_c \sinh(\gamma_{pr} l),$$

which gives $B \approx 4.52 + j42.15$. Since $Z = B$, the shunt admittance at each end is

$$Y_{\text{sh}} = \Im(\frac{A-1}{B}).$$

The resulting series parameters are

$$r_{\text{eq}} = \Re(B) \approx 4.52\ \Omega, \qquad L_{\text{eq}} = \frac{\Im\{B\}}{\omega} \approx 0.134\ \text{H}.$$

From Y_{sh},

$$Y_{\text{sh}} \approx 3.03 \times 10^{-4}\ \text{S}, \qquad C_{\text{sh}} = \frac{Y_{\text{sh}}}{\omega} \approx 0.966\ \mu\text{F}.$$

4.6 Comparative analysis of the full and π-section OPL models

4.6.1 Comparison of power line models under steady-state operation

To evaluate the characteristics of the power line models, the three representations (the simplified π-section model, the sequence-domain π-section model, and the full model) were connected almost directly to balanced three-phase voltage sources under a high short-circuit ratio, as illustrated in Figure 4.9. The power angle was set to $\delta_v = 13.54°$, and the phase-to-phase voltage magnitude was fixed at $|V_s| = 500$kV. Under these conditions, the sending-end and receiving-end active power values are $P_s = 700$MW and $P_r = 683$MW, respectively.

Figure 4.10 shows the sending-end phase currents, I_{abc}, obtained from the simplified π-section model, the sequence-domain π-section model, and the full model. Overall, the three sets of waveforms exhibit a high degree of overlap, indicating strong agreement between the modelling approaches, as seen in Figure 4.10a. However, the zoomed-in view (Figure 4.10b) reveals that the simplified and sequence-domain π-models are nearly identical, whereas the full model displays slight asymmetry, even after a full transposition cycle applied at one-third and two-thirds of the line length. A similar behaviour is observed in the receiving-end phase currents.

The sequence components of the sending- and receiving-end currents for all three models are summarised in Table 4.1. It is observed that the full model introduces non-zero negative- and zero-sequence components at both ends of the line. Nevertheless, their magnitudes remain below 2%, which complies with the permissible limits specified in the Kazakhstan Grid Code (GC).

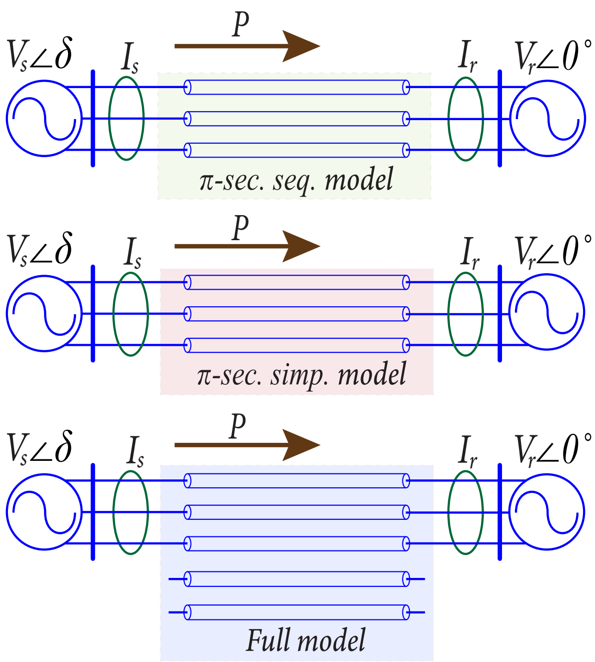

Figure 4.9 Steady-state operation of the different power line models.

Since the full model permits evaluation of the ground-wires' current profile along the line under steady-state conditions, the RMS values of the ground-wire currents, measured at 20km intervals, are presented in Figure 4.11. The corresponding voltage levels along the ground wires remain close to zero. The plot illustrates the persistence and spatial distribution of the induced currents flowing through the ground conductors, which contribute to additional power losses in the system.

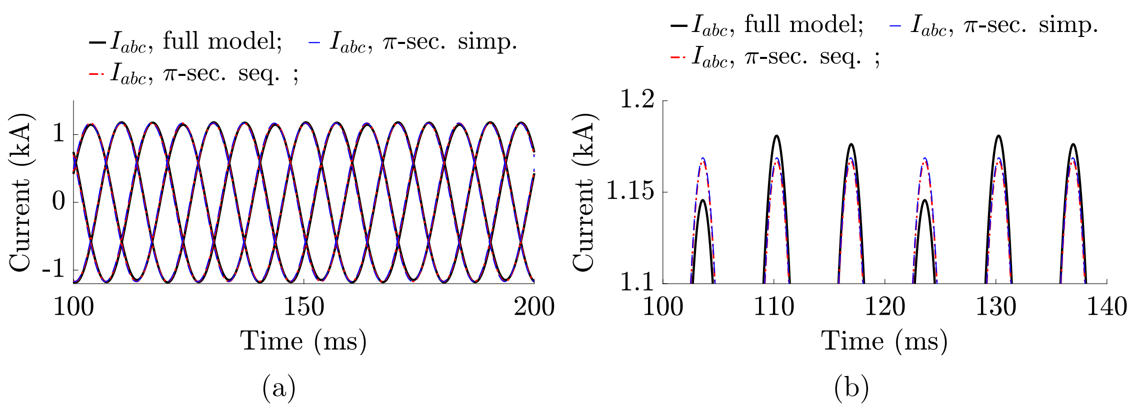

Figure 4.10 Steady-state mode sending-end phase currents of the π-model and full model: (a) complete view, (b) zoomed-in view.

Table 4.1 Sequence-component currents of sending and receiving ends under π-model and full model

		π-sec. simp. model	π-sec. seq. model	full model
$\|I_s\|$, A	+	$1169\angle 25.14°$	$1167\angle 25.16°$	$1168\angle 25.15°$
	−	0	0	$17.24\angle -164.8°$
	0	0	0	$4.9\angle -158.4°$
$\|I_r\|$, A	+	$1116\angle 0.23°$	$1115\angle 0.22°$	$1115\angle 0.22°$
	−	0	0	$17.28\angle -177.8°$
	0	0	0	$4.816\angle -175.8°$

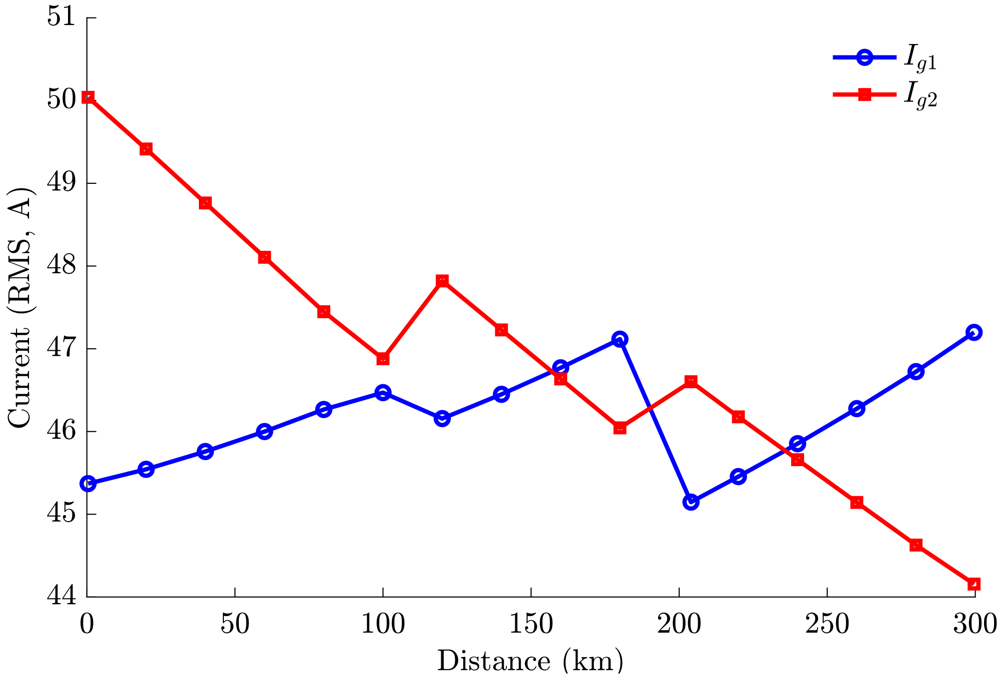

Figure 4.11 Profile of ground wire currents along the transmission line.

4.6.2 Comparison of OPL models in Electromagnetic Transients (EMT) simulations

The increasing interest in EMT-type models—and the shift away from purely phasor-based approaches—is driven by the high penetration of RES in modern power grids, where hidden challenges such as unmodelled interactions have been reported [74]. Consequently, EMT models are preferable for capturing these phenomena.

To assess the OPL models in terms of electromagnetic wave propagation, the a-phase of each model was energised, as shown in Figure 4.12. The S_1 switches were closed at 1/50 s and opened at 4/50 s, thereby connecting a voltage source of $500\,\mathrm{kV}/\sqrt{3}$ to the π-model, full model, and distributed-parameter model [75]. The phase-to-ground voltages at the receiving end were then measured.

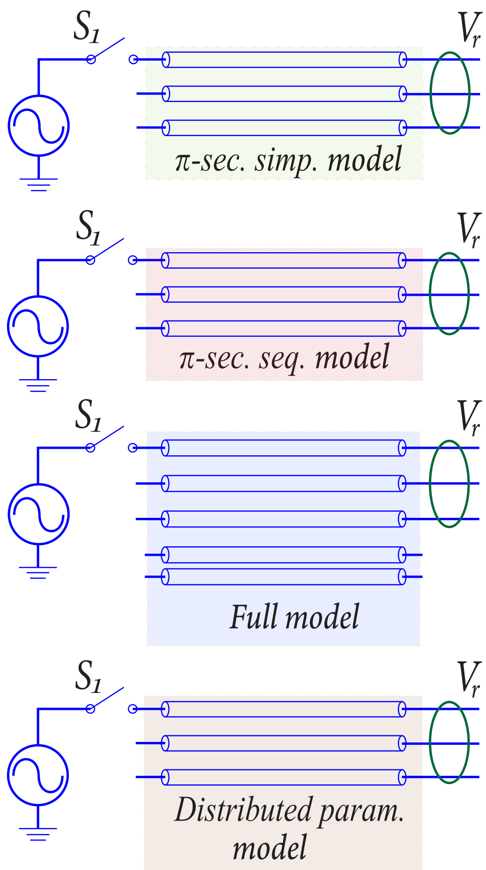

Figure 4.12 One-phase energisation configuration used to excite the different OPL models.

Figure 4.13 presents the receiving-end voltages for the four OPL models, together with zoomed-in views from 5 ms to 25 ms. As phase a is energised, its voltage magnitude is significantly higher than that of the other phases, whose responses remain comparatively similar. However, since the simplified π-section model does not include electromagnetic couplings, only the a-phase is excited in that representation.

In the zoomed-in views (Figures 4.13(b), (d), and (f)), sharp voltage spikes can clearly be observed in the full model and distributed-parameter models, which show a close overlap. In contrast, the π-section sequence model exhibits smoother voltage waveforms. These high-frequency spikes and oscillatory behaviours are characteristic of electromagnetic travelling waves, which are accurately represented by the full and distributed-parameter models. Nevertheless, the accuracy of the π-section sequence model in EMT studies can be improved by increasing the number of line segments used to represent the total line length.

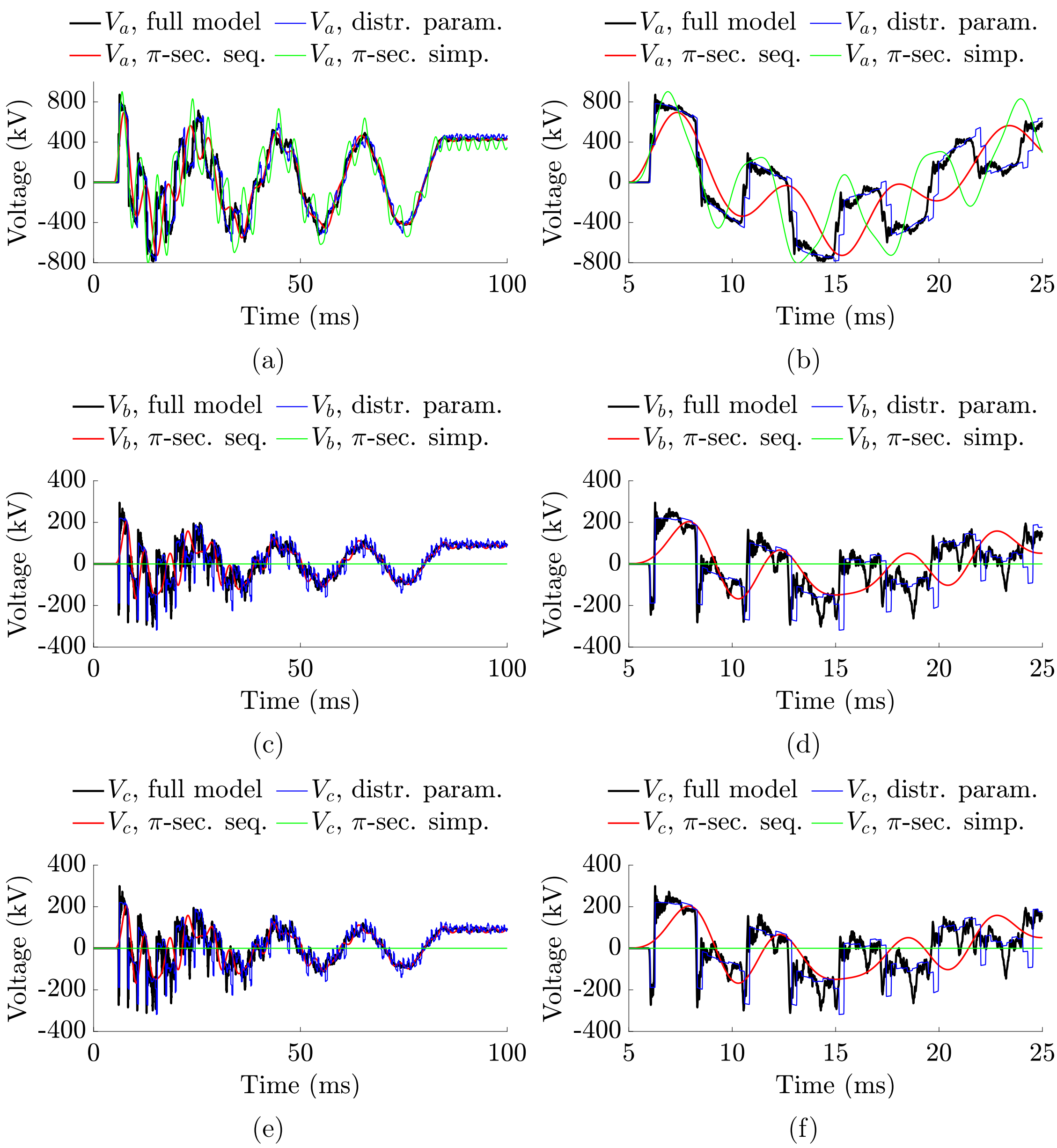

Figure 4.13 Receiving-end voltages for different OPL models. (a), (c), and (e) show the phase voltages V_a, V_b, and V_c, respectively; (b), (d), and (f) present the corresponding zoomed-in views.

4.6.3 AO mimicking to assess OPL model responses

To evaluate the performance of the π-models and full model representations under AO, a test environment—similar to the conditions described in Subsection 4.6.1—was created to mimic AO scenarios. Cases involving one or two open phases were considered, both without a short circuit and with a permanent short circuit applied at various locations along the line. The reference scenario assumes a permanent short circuit located at the midpoint of the transmission line.

To eliminate the influence of the E-STATCOMs, their control systems, and their grid connection, the OPL models were directly connected—under a high short circuit ratio—between two voltage sources. The E-STATCOMs were replaced with three-phase current sources J_s and J_r, as illustrated in Figure 4.14.

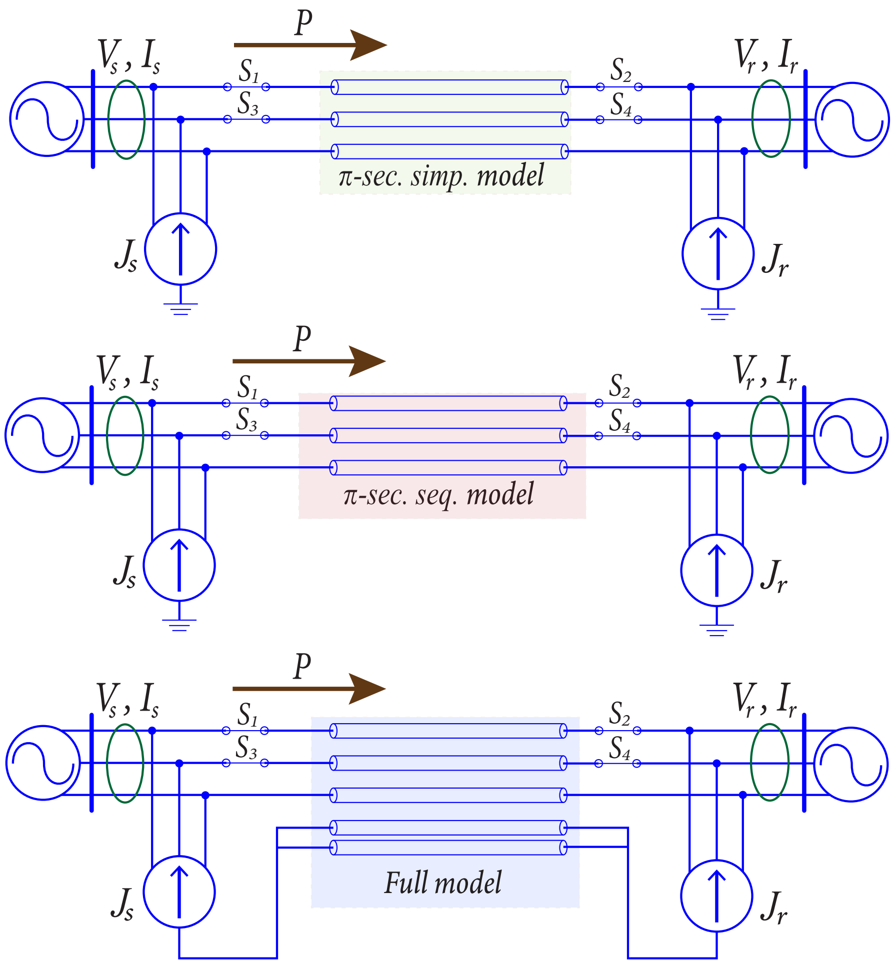

Figure 4.14 Principal circuit used to mimic AO.

Two-phase AO mimicking

The first simulation scenario considered an open a-phase configuration, with circuit breakers S_1 and S_2 in the open position. Sequence component currents were measured at both ends of the OPLs. The injected sequence currents are listed in Table 4.2, while the resulting sending- and receiving-end sequence currents are presented in Table 4.3. The corresponding sending- and receiving-end powers, together with the associated power losses for the π-models and the full model, are summarised in Table 4.4.

The results are broadly consistent across the π-section sequence model and the full model model, showing only minor deviations. In contrast, the simplified π-section model produces noticeably different results due to electromagnetic coupling is not presented in it.

Table 4.2 Sequence-current injections for the three OPL models.

Current sources (CS)		π-sec. simp. model	π-sec. seq. model	full model
$I_{\mathrm{s.cs.a}}$ (A)	$-$	$389.6\,\angle{-154.9}°$	$492.5\,\angle{-157.4}°$	$491.5\,\angle{-157.4}°$
	0	$389.6\,\angle{-154.9}°$	$188.6\,\angle{-141.4}°$	$189.2\,\angle{-141.6}°$
$I_{\mathrm{r.cs.a}}$ (A)	$-$	$-372\,\angle{-179.8}°$	$-477.4\,\angle{-179.7}°$	$-476.4\,\angle{-179.7}°$
	0	$-372\,\angle{-179.8}°$	$-160.2\,\angle{-176.6}°$	$-161\,\angle{-176.7}°$

Table 4.3 Sequence-component currents for the three OPL models after sequence-current injection.

Sequence comp.		π-sec. simp. model	π-sec. seq. model	full model
$\lvert I_s\rvert$ (A)	+	780.6	677	677.3
	$-$	0.708	1.42	1.42
	0	0.708	0.185	1
$\lvert I_r\rvert$ (A)	+	745.4	638.6	639
	$-$	0.822	5.171	4.84
	0	0.822	0.16	1.05

Since the full model model enables direct observation of the opened phase along the line, Figure 4.15 illustrates the distribution of the RMS values of the a-phase current under four configurations: without a short circuit (red line) and with a

Table 4.4 Power values for the three OPL models after sequence-current injection.

Power	π-sec. simp. model	π-sec. seq. model (MW)	full model(MW)
P_s	468.2	403.2	403.4
P_r	456.5	391.1	391.3
ΔP	11.72	12.1	12.1

permanent short circuit applied at 150 km (blue line), 100 km (black line), and 200 km (cyan line).

In the short-circuited cases, the curves show that the zero-sequence current—flowing through the ground wires—is also injected into the a-phase conductor and propagates toward both ends of the line. In contrast, the red curve, corresponding to the case without any electrical connection to grounded elements or other phases, represents only the induced currents resulting from electromagnetic coupling with the energised phases. The higher peak values observed in the blue and cyan curves arise from the short circuits being applied at asymmetric locations along the line.

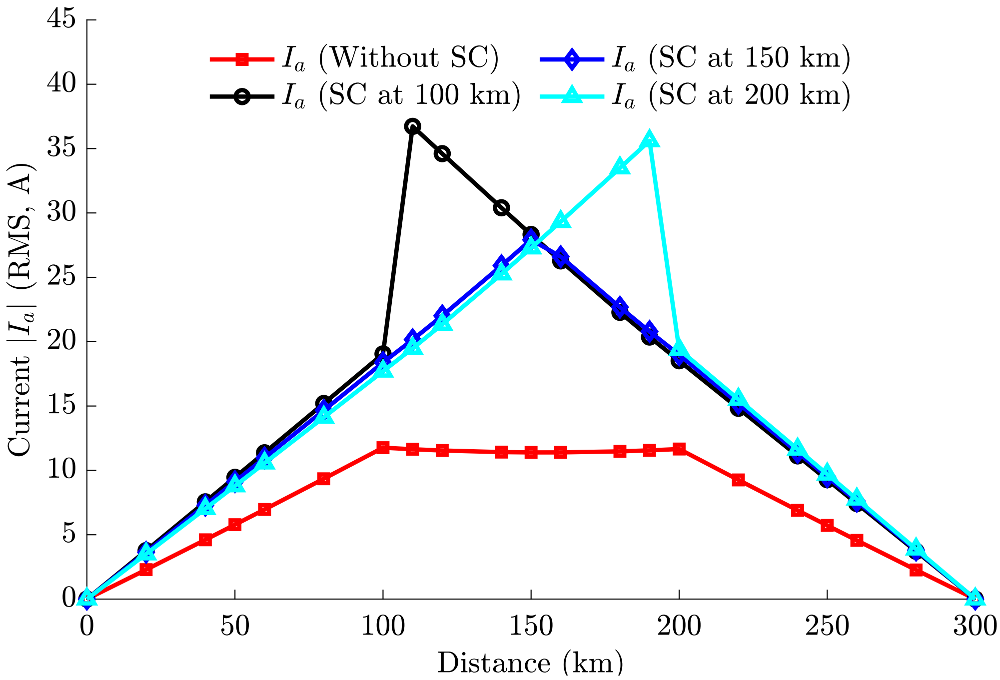

Figure 4.15 RMS values of the a-phase current along the line under four short-circuit scenarios.

Because the interest lies not only in the magnitude of the current flowing in the opened phase but also in its direction, Figure 4.16 presents the corresponding vector diagrams of the a-phase currents along the line for the configurations shown in Figure 4.15. The associated phasor tables are provided in Appendix C.4 and Appendix C.5.

When no short circuit is applied, the vector diagram in Figure 4.16a indicates that the current in the opened a-phase is unidirectional and aligned with the current in the energised phases. In contrast, when AO is implemented with a short circuit located at the midpoint of the line, the vector diagram in Figure 4.16b shows that the injected current divides and propagates toward both ends of the line, consistent with the behaviour observed in the RMS distribution.

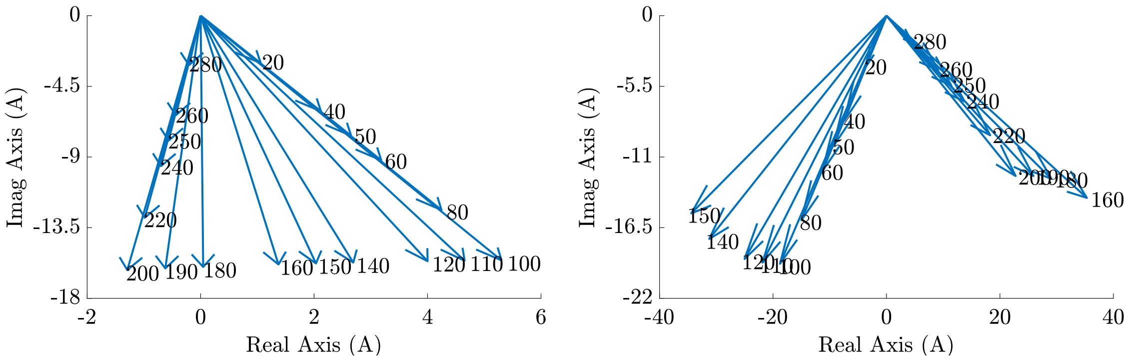

(a) (b)

Figure 4.16 a-phase current vector diagrams during TPAO. Subfigures (a) and (b) correspond to the cases without a short circuit and with a short circuit applied at 150 km, respectively. (*Axes are scaled.)

One of the principal zero-sequence distribution paths is through the towers. Figure 4.17 illustrates the zero-sequence current flowing through the towers at both extremities and at the short-circuit location under TPAO. At other points along the TOPL, the tower currents remain close to zero. Subfigures (a) and (b) exhibit similar behaviour, while Subfigure (c) shows symmetry about the short-circuit point at 150 km. The corresponding phasors are provided in Appendix C.6.

The towers nearest to each terminal carry the highest current magnitudes, exhibiting an exponential spatial decay as the distance from the energising source increases. A complete representation of the zero-sequence current distribution during TPAO, including all relevant conduction paths within the system, is shown in Figure 4.18.

One-phase AO mimicking

The second simulation scenario considered the disconnection of the a- and b-phases, with circuit breakers S_1, S_2, S_3, and S_4 in the open position. Sequence component currents were measured at both ends of the OPLs. The injected sequence currents are listed in Table 4.5, while the corresponding sending- and receiving-end sequence

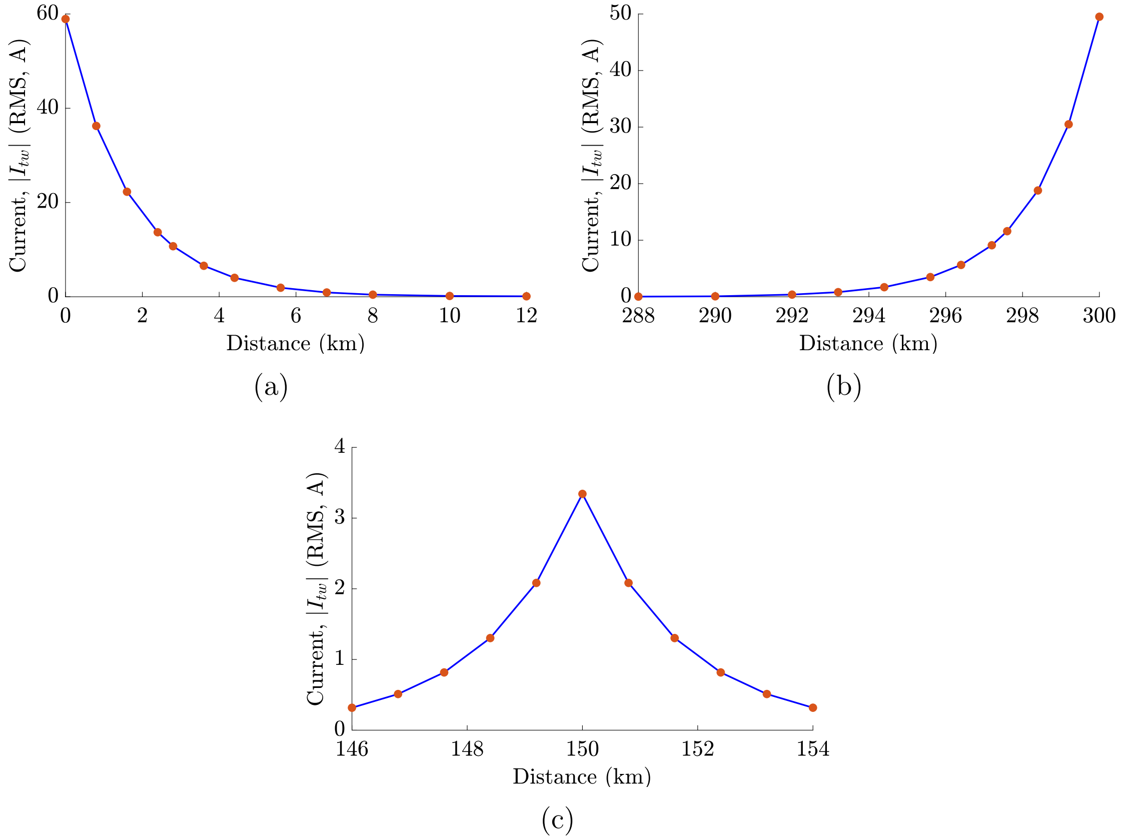

Figure 4.17 Zero-sequence current distribution through towers: (a) near the sending end, (b) near the receiving end, and (c) intermediate section.

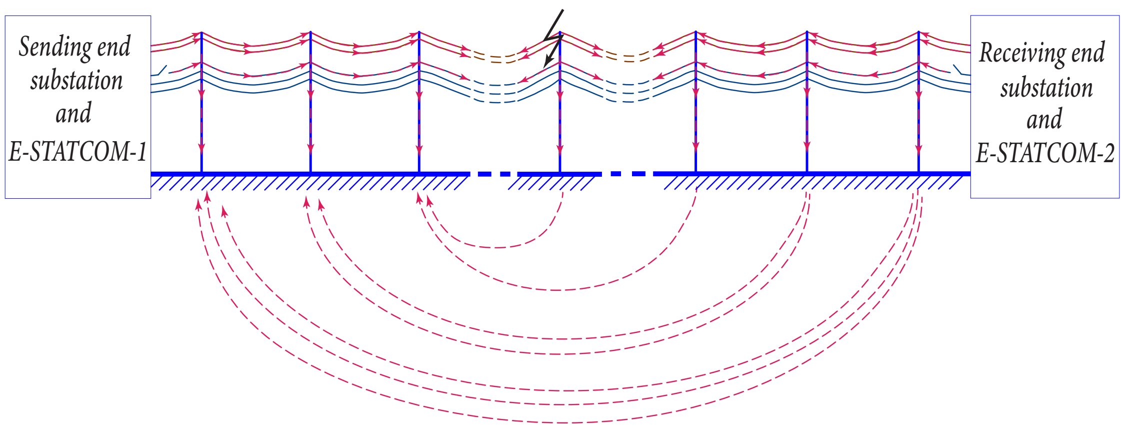

Figure 4.18 Zero-sequence current distribution picture.

currents are presented in Table 4.6. The sending- and receiving-end powers, along with the associated power losses for both the π-model and full model, are summarised in Table 4.7. The results exhibit close agreement between the two models, with only minor deviations.

Table 4.5 Sequence-current injections for the three OPL models.

Current sources (CS)		π-sec. simp. model	π-sec. seq. model	full model
$I_{\text{scs\_a}}$ (A)	−	$389.6\angle{-94.86°}$	$253.2\angle{-85.82°}$	$253.1\angle{-85.68°}$
	0	$389.6\angle 145.1°$	$253.2\angle 154.2°$	$253.1\angle 154.3°$
$I_{\text{rcs\_a}}$ (A)	−	$-372\angle{-119.8°}$	$-225\angle{-117°}$	$-224.6\angle{-116.9°}$
	0	$-372\angle 120.2°$	$-225\angle 123°$	$-224.6\angle 123.1°$

Table 4.6 Sequence-component currents for the three OPL models after sequence-current injection.

Sequence comp.		π-sec. simp. model	π-sec. seq. model	full model
$\lvert I_s \rvert$, A	+	391	255.2	254.4
	−	1.44	3.3	1.55
	0	1.4	3.23	1.51
$\lvert I_r \rvert$, A	+	373.4	225.7	226.2
	−	1.53	2.8	1.59
	0	1.53	2.8	1.59

Table 4.7 Power values for the three OPL models after sequence-current injection.

Power	π-sec. simp. model (MW)	π-sec. seq. model (MW)	full model(MW)
P_{s}	234.57	145.69	145.82
P_{r}	228.6	138.1	138.30
ΔP	5.89	7.58	7.51

As in the case of TPAO mimicking, Figure 4.19 shows the RMS distribution of the a- and b-phase currents along the transmission line under AO with two open phases, evaluated across four configurations: without a short circuit (black and red lines), and with a permanent short circuit applied at 100km (green and blue lines), 150km (cyan and pink lines), and 200km (olive and teal lines).

In the short-circuited cases, the zero-sequence current flowing through the ground wires is coupled into the a- and b-phase conductors and propagates towards both extremities. However, the propagation behaviour is more intricate than in the single-phase open case, likely due to the combined effects of electromagnetic coupling between the transposed conductors and the influence of the ground-return impedance.

In contrast, the two lowest curves correspond to the configuration without any electrical connection to ground or other phases, reflecting purely induced currents arising from mutual coupling with the energised phase.

Figure 4.20 provides the corresponding vector diagrams of the a- and b-phase currents along the line for the same configurations, further illustrating the current propagation patterns. The associated phasor data are detailed in Appendix C.7 and Appendix C.8.

The vector diagram in Figure 4.20a shows the case without a short circuit, where the current in the a-phase flows in the same direction as the energised c-phase. In contrast, the current in the b-phase splits and propagates towards both ends of the line, resulting in a sinusoidal distribution, as reflected by the red curve in Figure 4.19.

As observed in the AO scenario with a single open phase, the currents in the disconnected a- and b-phases also divide and flow toward both extremities when a short circuit is present, as illustrated in the vector diagrams in Figures 4.20c and 4.20d.

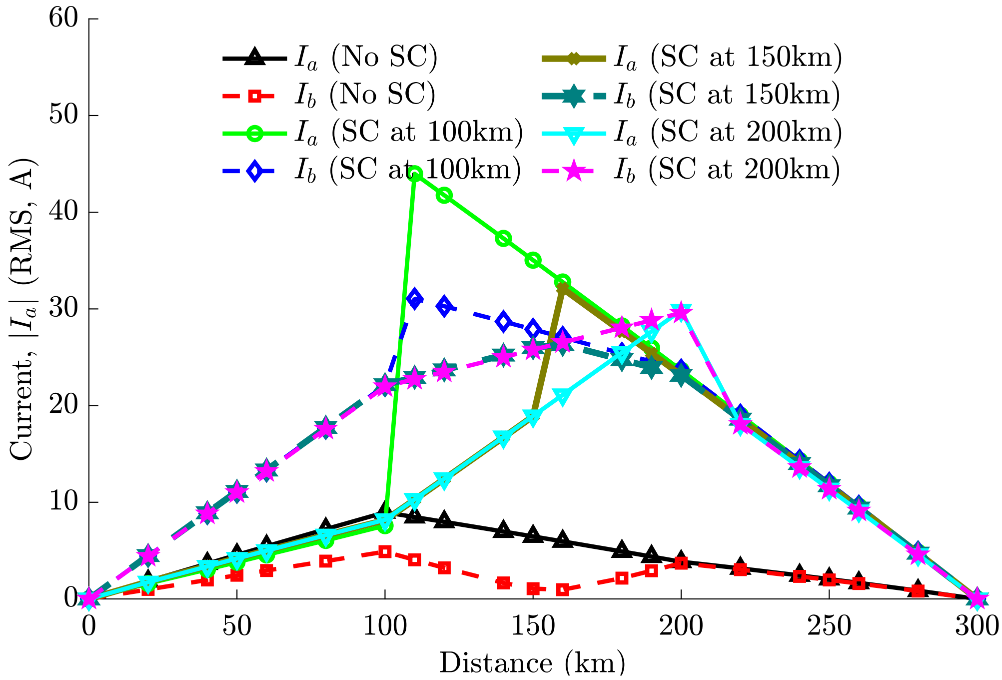

Figure 4.19 RMS values of a, b-phase currents along the line under two scenarios: with permanent short circuit (blue) and without short circuit (red).

Figure 4.21 presents the distribution of the zero-sequence current flowing through the towers at both ends and at the short circuit point of the line during OPAO. The corresponding phasors are provided in Appendix C.9. Similar to the TPAO, the towers closest to the terminals exhibit the highest current magnitudes, with

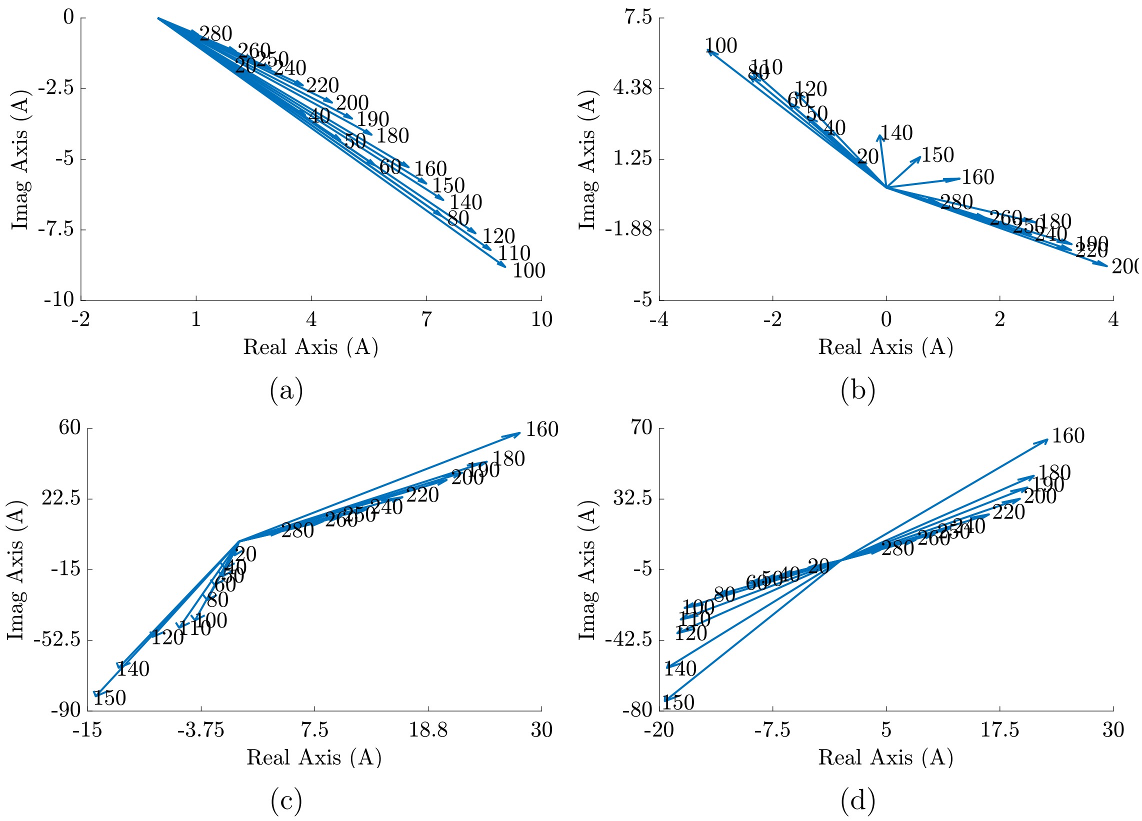

Figure 4.20 *a,b*-phase current vector diagrams during OPAO. Subfigures (a) and (b) correspond to the case without a short circuit, whereas Subfigures (c) and (d) show the *a*- and *b*-phase currents, respectively, when the short circuit is applied at 150 km. (*Axes are scaled.)

a spatially decaying profile observed along the line (Figure 4.18). However, the magnitudes are slightly higher compared with the one-phase scenario.

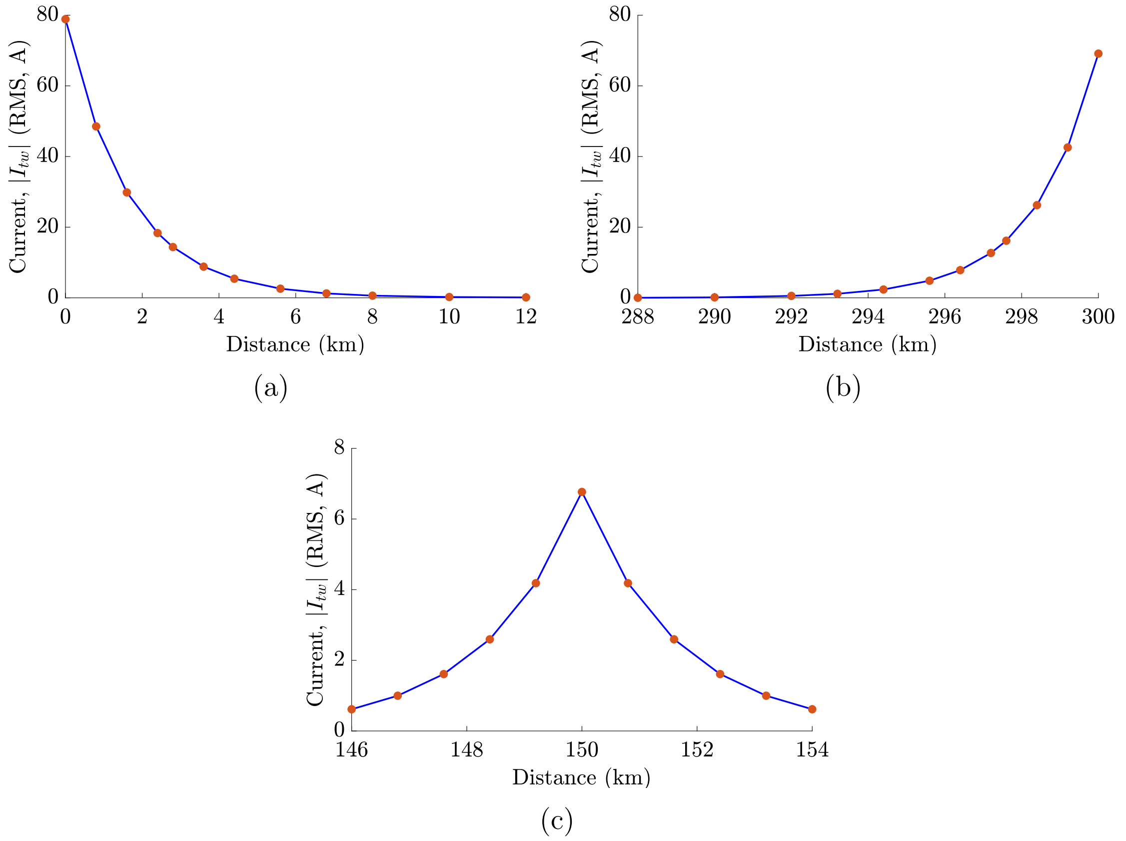

Figure 4.21 Zero-sequence current distribution through towers when two phases are open: (a) near the sending end, and (b) near the receiving end.

4.7 Conclusion

This chapter has presented a comprehensive comparison of the simplified π-section model, the π-section sequence model, and the full-model representation of the OPL with respect to steady-state operation, electromagnetic transients, and asymmetric operation under two-phase and one-phase AO. While the π-section sequence model yields results comparable to those of the full model under steady-state and AO conditions in terms of sequence components and power-flow values, it exhibits notable limitations—most prominently the inability to represent zero-sequence current distribution and reduced accuracy in capturing electromagnetic transients. Conversely, the full model provides a more detailed and physically accurate representation by modelling each segment of the transmission line individually, albeit at the cost of increased computational effort. The simplified π-section model aligns with the other models only in steady-state operation making it suitable for power flow calculations only.

In terms of power delivery, mimicking TPAO retains approximately three-fifths of the pre-fault power, whereas OPAO reduces it to about one-fifth for both the π-section sequence model and the full model. These values are lower than the two-thirds and one-third, respectively, reported by the simplified π-section model as proposed in [24] by R. Marceau *et al.* and later by A. Sana in [27]. This deviation arises from several factors, including electromagnetic coupling between phase conductors, the impedance of the ground wire(s), and ground resistivity. The first of these is explicitly demonstrated in Figures 4.15 and 4.19, where current circulation is observed in the open phase(s) even in the absence of an electrical connection to the ground system (i.e., when no short circuit is applied). The impedance of the ground wire(s) and the ground resistivity are implicitly incorporated into the calculation of the transmission-line impedance and, consequently, into the impedance matrix $\mathbf{Z}$. Under unbalanced operating conditions—such as two-phase and one-phase AO—these factors influence the resulting power flow along the line.

The distribution of zero-sequence current through the towers under AO, as captured by the full model, exhibits wave-like spatial behaviour (Figures 4.17 and 4.21). The highest magnitudes occur at towers located near the OPL extremities, followed by a rapid decay within approximately 10 km (Figure 4.18).

The next chapter examines full model-based AO realised through the use of E-STATCOMs installed at the extremities of the transmission line, controlled according to the approach developed in Chapter 3.

Chapter 5

Asymmetrical Operation of a Full Transmission OPL Model

5.1 Introduction

This chapter investigates and analyses two scenarios of AO in which either one or two phases of the transmission line are open, corresponding to TPAO and OPAO, respectively, and electric hazard safety. In practice, the TPAO scenario, typically resulting from a single-phase-to-ground fault, is more common and advantageous, as it allows for higher power transfer compared with the case where two phases are open. Nevertheless, two-phase-to-ground and phase-to-phase faults represent the second most common fault type in EHV TOPLs. Therefore, owing to the capability of the E-STATCOMs installed at the line extremities to facilitate OPAO, this scenario is also presented and examined in detail.

In this chapter, for the single-phase-to-ground short circuit case, the faulted phase is the a-phase; for the two-phases-to-ground short circuit case, the faulted phases are the a- and b-phases. Nevertheless, the developed AO realisation method is applicable to any faulted phase or combination of phases.

Figure 5.1 illustrates a power line connected to a 500kV grid through the Thévenin grid equivalent, with E–STATCOMs installed at both ends through transformers T_1 and T_2; the impedance and transformer parameters are provided in AppendixC.1 and Appendix C.2. The LV-side ground of each transformer is connected to the DC-link ground, whereas the HV side is bonded to the ground wires. Previous studies on AO [23, 24] implemented current sequence-component suppression devices directly at the voltage sources, which significantly enhances the stability of AO and therefore does not allow validation of the control performance of these devices.

In this thesis, contrary to similar studies done by other authors [10, 24], impedance representing the actual grid connection is inserted between the voltage sources and the transmission line. The δ_v angle was adjusted to 16.1° in order to preserve the active power transfer at 700MW, consistent with the conditions described in Section 4.6.1. Table 5.1 presents the sequence-component current magnitudes at

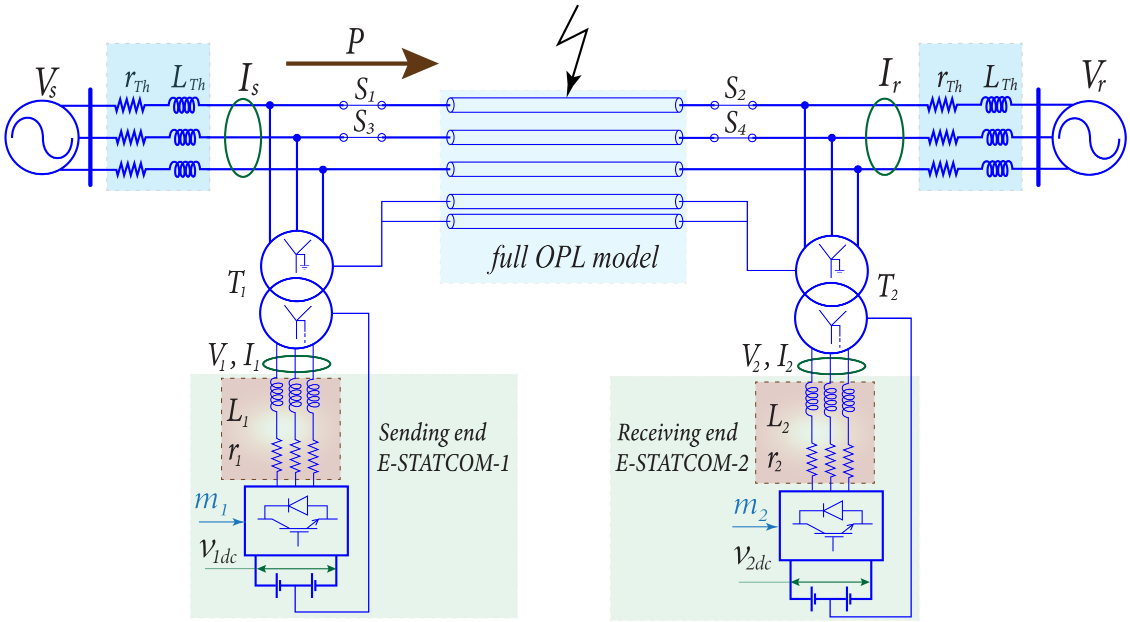

Figure 5.1 EHV OPL with two ground wires equipped with E-STATCOMs at the extremities.

the sending and receiving ends under steady-state conditions (prior to the fault). The negative- and zero-sequence components persist due to the factors discussed in Subsection 4.6.1 of Chapter 4.

Table 5.1 Sequence-component current magnitudes at the sending and receiving ends under steady-state conditions (prior to the fault).

Sequence comp.		full model
$\lvert I_s \rvert$, A	+	1170.64
	–	14.12
	0	4.62
$\lvert I_r \rvert$, A	+	1107.88
	–	15.12
	0	4.53

5.2 Two-phase AO

5.2.1 Two-phase AO without pre-fault power flow restoration

When a single-phase-to-ground short circuit occurs in the middle of the power line, circuit breakers S_1 and S_2 isolate the faulted a-phase. The fault is initiated at 220ms, and its clearance requires four cycles (80ms); consequently, the a-phase is disconnected at 300ms. E-STATCOM-1 and E-STATCOM-2 are subsequently activated at 400ms.

Figure 5.2 illustrates the phase currents at both the sending and receiving ends. Subplots (a) and (c) depict the current waveforms at the respective ends during the interval from 200ms to 400ms, starting from a balanced steady-state condition and progressing through the fault event and its subsequent clearance. Subplots (b) and (d) show the restoration of balanced three-phase currents following the fault. The plots collectively capture the full dynamic response of the system, encompassing the disturbance, its mitigation, and the subsequent recovery.

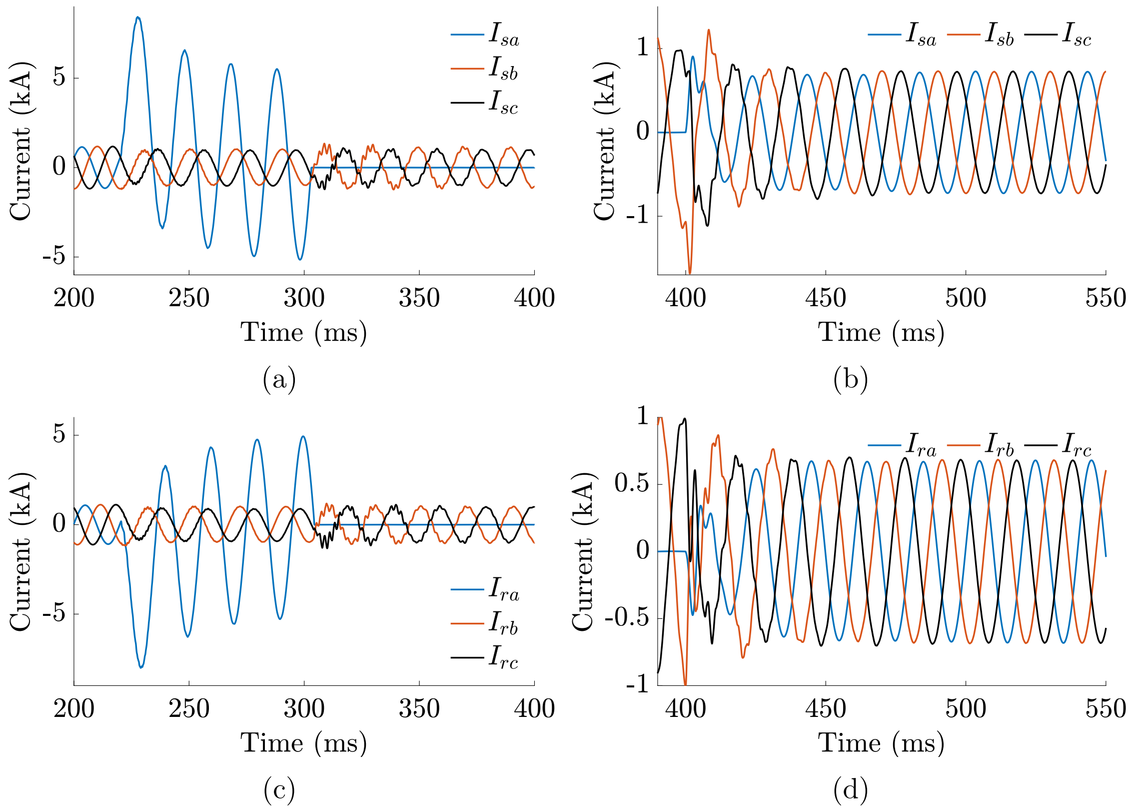

Figure 5.2 Sending- and receiving-end phase currents during the one-phase-to-ground short circuit, fault clearance, and TPAO.

The evolution of the sequence-component currents at the sending and receiving ends is illustrated in Figure 5.3. Subplots 5.3a and 5.3c present the full response from 200 to 600ms, covering the transition from steady-state operation to the fault occurrence, phase opening, and subsequent suppression of the sequence-current components. The corresponding magnified views over the 400–500ms interval are shown in subplots 5.3b and 5.3d, respectively, highlighting the post-opening current suppression dynamics at both line ends.

The positive-sequence component is brought under control relatively quickly, within approximately 40ms. This rapid response is attributed to its rise time being twice as fast as that of the negative- and zero-sequence components (Tables 3.2, 3.3, and 3.4). In contrast, the suppression of the negative- and zero-sequence current components requires around 100ms at both the sending and receiving ends. Once these unbalanced sequence components are fully mitigated, a slight increase in the positive-sequence current is observed, indicating the redistribution of the remaining current after the suppression process.

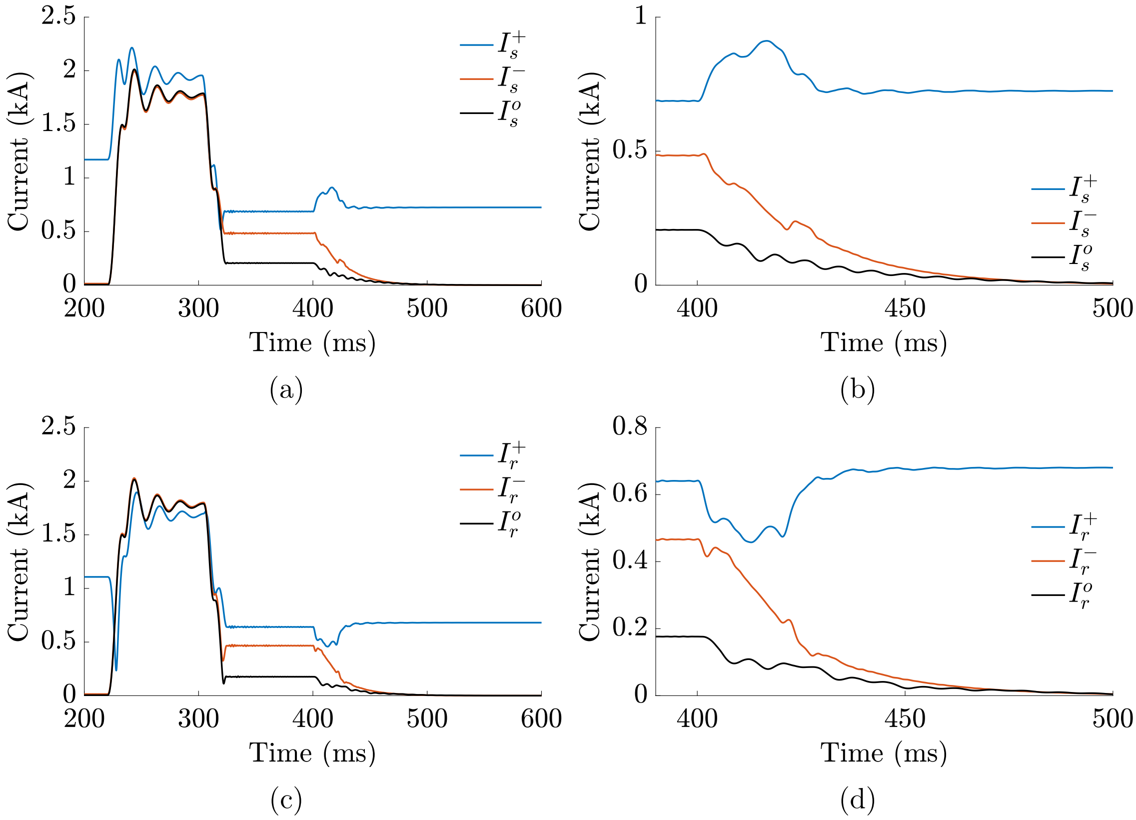

Figure 5.3 Sending- and receiving-end sequence-component currents during fault occurrence, phase opening, and sequence-component suppression.

Table 5.2 summarises the sequence-component current magnitudes at the sending and receiving ends after fault clearance, after sequence-current injection, and for the components supplied by E-STATCOM-1 and E-STATCOM-2. After fault clearance, negative- and zero-sequence currents are present at both ends, indicating the unbalanced operating condition before compensation. Following sequence-current injection, these components are effectively suppressed, with the negative-sequence current reduced from 484.72A to 0.2A at the sending end and from 465.59A to 0.004A at the receiving end. Similarly, the zero-sequence current decreases from 205.97A to 0.05A at the sending end and from 176.28A to 0.04A at the receiving end. The injected E-STATCOM currents mainly correspond to the negative- and zero-sequence components, while the injected positive-sequence current remains negligible. As the positive-sequence current is not injected, the pre-fault power flow is not restored.

Table 5.2 Sequence-component current magnitudes for the TPAO scenario.

Seq. comp. current (A)	After fault clearance	400ms after seq. comp. injection	Seq. comp. injected by E-STATCOM
Sending end			
+	687.73	725.3	1.62
−	484.72	0.2	525.91
0	205.97	0.05	204.06
Receiving end			
+	640.09	680.82	1.64
−	465.59	0.004	509.66
0	176.28	0.04	172.95

Figure 5.4 presents the output phase currents of E-STATCOM-1 and E-STATCOM-2, shown in subfigures 5.4a and 5.4b, respectively. The currents are measured on the high-voltage sides of transformers T_1 and T_2, corresponding to the connection points of the two E-STATCOMs. Since the a-phase is open, the injected current with the largest magnitude also occurs in this phase.

The magnitudes of the negative- and zero-sequence currents, expressed as percentages of the corresponding positive-sequence component at the sending and receiving ends, are summarised in Table 5.3. The table compares two operating conditions: the steady-state balanced condition and the condition one second after sequence-component suppression. The results show that the use of E-STATCOMs at the line extremities effectively suppresses the negative- and zero-sequence components while maintaining TPAO operation. Consequently, the overall sequence-current balance is substantially improved, with the negative-sequence component reduced by more than

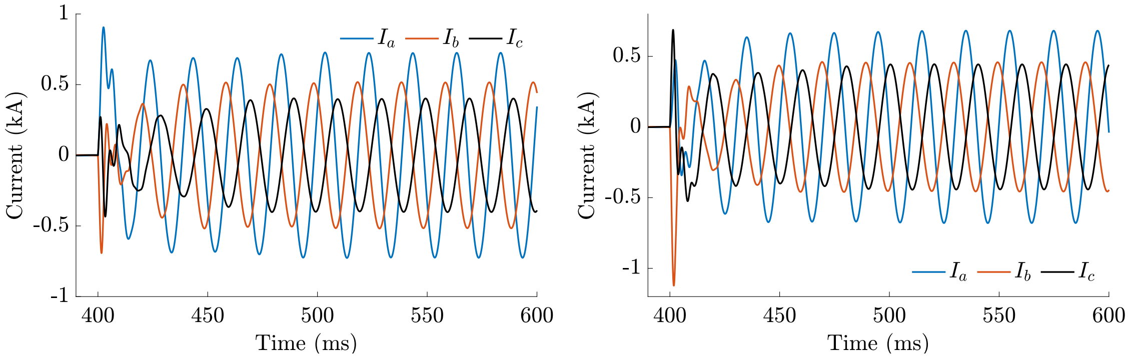

(a) (b)

Figure 5.4 Output phase currents of E-STATCOM-1 and E-STATCOM-2 in the TPAO case.

a factor of two and the zero-sequence component by over two orders of magnitude at the sending end. At the receiving end, the corresponding reductions reach approximately three and two orders of magnitude for the negative- and zero-sequence components, respectively.

Table 5.3 Negative- and zero-sequence current magnitudes relative to the positive-sequence component in the TPAO case.

	Seq. component	Steady-state condition	After seq.-component suppression
Sending end	I_-/I_+	1.21%	0.027%
	I_0/I_+	0.39%	0.0074%
Receiving end	I_-/I_+	1.36%	0.00059 %
	I_0/I_+	0.41%	0.00588%

5.2.2 Two-phase AO with pre-fault power flow restoration

When TPAO is implemented and the E-STATCOMs at both extremities are equipped with adequately sized energy storage systems, such as batteries, the pre-fault power flow can be fully or partially restored. The battery model is described in Subsection 3.1.2, and the corresponding parameters are listed in Appendix C.3. Two identical lithium-ion batteries are employed as the energy storage units for E-STATCOM-1 and E-STATCOM-2.

To enable the restoration of power transfer, positive-sequence current must be injected at both the sending and receiving terminals. As illustrated in Figure 5.1, E-STATCOM-1 at the sending end absorbs active power, whereas E-STATCOM-2 at the receiving end injects active power. Consequently, the external grid experiences a balanced three-phase power flow.

Accordingly, the control reference for the positive-sequence current of E-STATCOM-1 is defined as

$$i_{d1}^{+^*} = -k_{id}^{+}\left(|I_{s.pref}^{+}| - |I_{s.posf}^{+}|\right) \tag{5.1}$$

and for E-STATCOM-2 as

$$i_{d2}^{+^*} = k_{id}^{+}\left(|I_{r.pref}^{+}| - |I_{r.posf}^{+}|\right) \tag{5.2}$$

where the proportional gain k_{id}^{+} is a tunable parameter that can be adjusted according to the SoC of the battery, real-time power flow requirements, and other operational constraints and objectives.

Figure 5.5 presents the positive-sequence component currents at the sending and receiving ends for four different values of k_{id}^{+}, namely 0, 0.25, 0.75, and 1. These currents are shown in subplots (a) and (c), respectively, while the associated SoC profiles of E-STATCOM-1 and E-STATCOM-2 are shown in subplots (b) and (d). As k_{id}^{+} increases, E-STATCOM-1 charges more rapidly, while E-STATCOM-2 discharges at a faster rate. However, since AO is primarily intended for short operational periods, typically less than one hour, the battery capacities can be sized accordingly. An illustration of sequence-component current suppression and positive-sequence current injection for the most demanding case, corresponding to $k_{id}^{+} = 1$, is presented in Figure 5.6. Subplots (a) and (c) show the sending- and receiving-end responses, respectively, from 200 to 600 ms, covering the transition from steady-state operation to fault occurrence, faulted phases opening, sequence-component suppression, and positive-sequence injection. The corresponding magnified views over the 400–500 ms interval are shown in subplots (b) and (d), respectively.

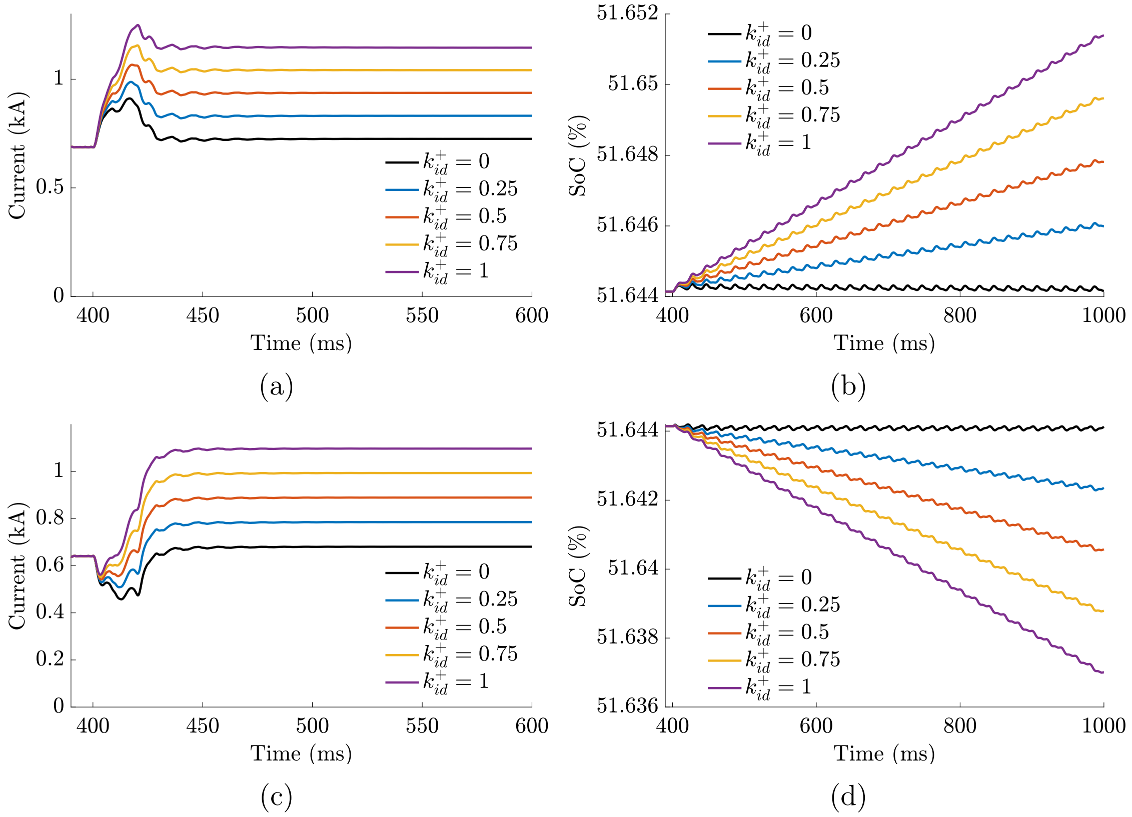

Figure 5.5 Positive-sequence currents and E-STATCOM SoC profiles for different k_{id}^{+} values.

The evolution of the sequence-component currents at the sending and receiving ends is illustrated in Figure 5.3. Subplots 5.3a and 5.3c present the full response from 200 to 600ms, covering the transition from steady-state operation to the fault occurrence, phase opening, and subsequent suppression of the sequence-current components. The corresponding magnified views over the 400–500ms interval are shown in subplots 5.3b and 5.3d, respectively, highlighting the post-opening current suppression dynamics at both line ends.

Figure 5.7 presents the output currents of E-STATCOM-1 and E-STATCOM-2 for $k_{id}^{+} = 1$ under TPAO. The currents are measured at the high-voltage sides of transformers T_1 and T_2 and are shown in subplots (a) and (b), respectively. Since the a-phase is open and the positive-sequence current is injected, the a-phase currents in the figure are the largest. At the sending end, the b- and c-phase currents are in phase, while at the receiving end, these currents are also in phase and nearly equal in magnitude.

Table 5.4 summarises the positive-sequence currents and active power at both the sending and receiving ends for different values of k_{id}^{+}. The reported values correspond to $t = 800$ms. For $k_{id}^{+} = 1$, the positive-sequence current magnitudes

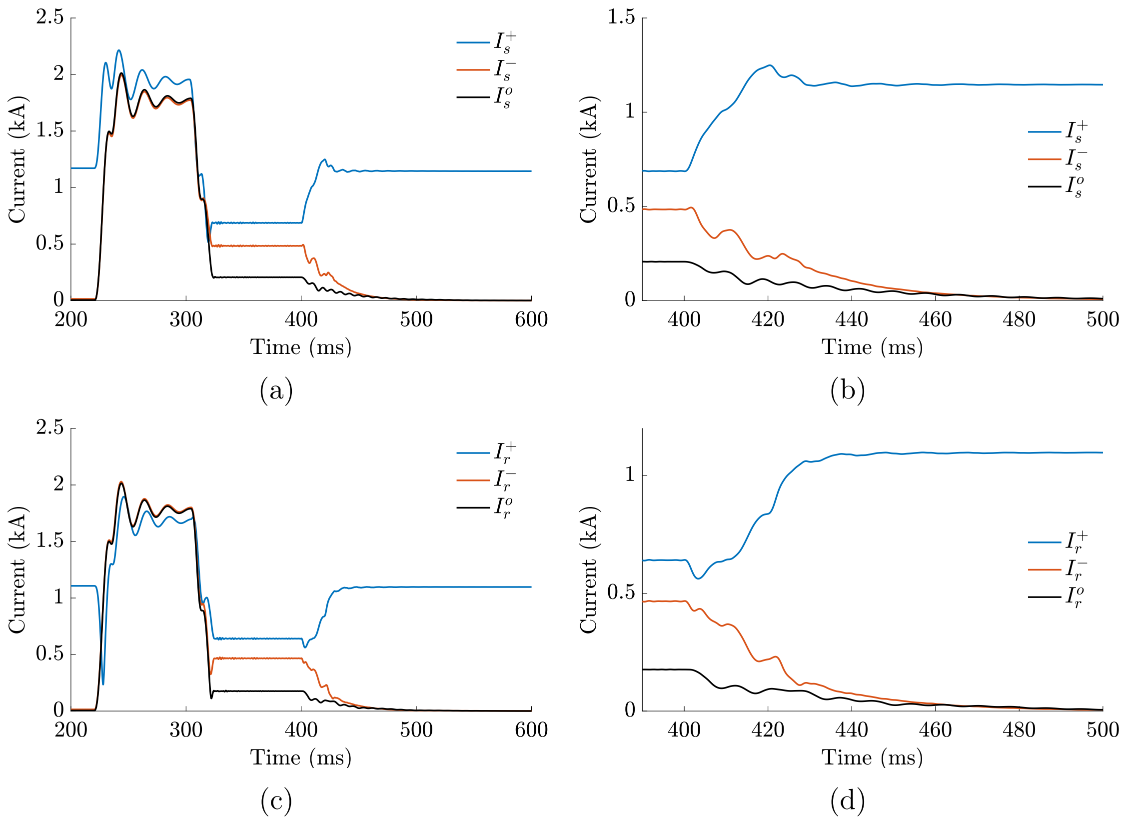

Figure 5.6 Sequence-component current suppression and positive-sequence injection for $k_{id}^{+} = 1$.

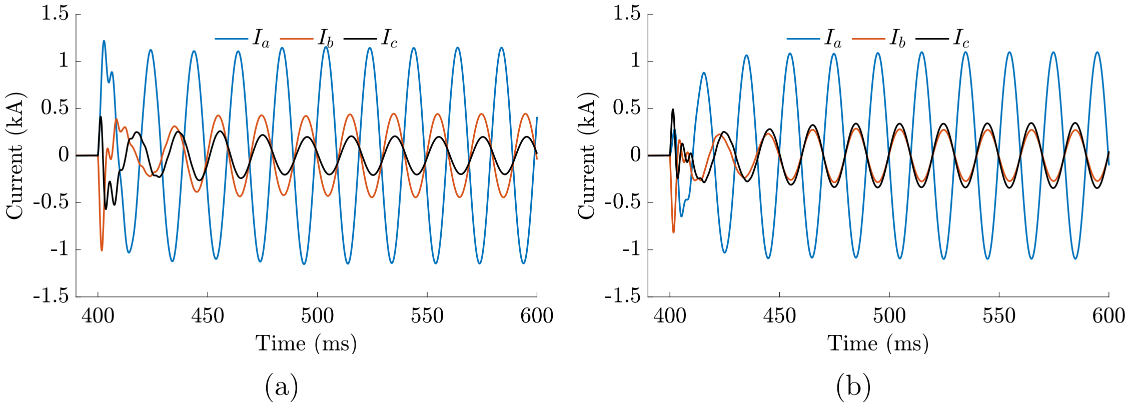

Figure 5.7 Output currents of E-STATCOM-1 and E-STATCOM-2 for $k_{id}^{+} = 1$ under TPAO.

at both terminals closely match the pre-fault values listed in Table 5.1. The small discrepancies—approximately 22A at the sending end and 10A at the receiving end—can be attributed to losses in components such as T_1 and T_2, electromagnetic coupling effects, and the influence of ground resistance.

Table 5.4 Positive-sequence currents and active power in the TPAO case.

Quantity	$k_{id}^{+} = 0$	$k_{id}^{+} = 0.25$	$k_{id}^{+} = 0.5$	$k_{id}^{+} = 0.75$	$k_{id}^{+} = 1$
$\lvert I_s^{+} \rvert$ (A)	725.3	832.08	938.15	1043.55	1148.33
$\lvert I_r^{+} \rvert$ (A)	680.82	785.26	889.67	993.92	1097.96
P_s (MW)	433.4	499.8	566.0	631.8	697.0
P_r (MW)	417.5	481.8	546.0	609.9	673.5

5.3 One-phase AO

5.3.1 One-phase AO without pre-fault power flow restoration

The OPAO case follows the same fault sequence and timing as the TPAO case. However, the two-phase-to-ground short circuit occurs at the midpoint of the transmission line, and circuit breakers S_1, S_2, S_3, and S_4 in Figure 5.1 isolate the faulted a- and b-phases. The fault is initiated at 220ms, the faulted phases are disconnected at 300ms after four cycles of fault clearance, and E-STATCOM-1 and E-STATCOM-2 are activated at 400ms to enable OPAO.

Figure 5.8 presents the phase currents at both the sending and receiving ends during the transition from normal operation to the two-phase-to-ground short circuit, fault clearance, and the subsequent OPAO mode. Subplots (a) and (c) show the currents during the 200–400ms interval, covering the transition from steady-state operation to fault initiation and the subsequent disconnection of the faulted phases. Subplots (b) and (d) show the post-activation response from 400 to 550ms, when OPAO is established. The peak fault currents in the a- and b-phases are substantially higher—approximately 1.5 times greater—than those observed during the single-phase-to-ground short circuit case. In contrast, after sequence-component suppression, the phase currents are lower than in the one-phase scenario, as expected, since only one phase remains energised in this configuration.

The evolution of the sequence-component currents at the sending and receiving ends is illustrated in Figure 5.9. Subplots (a) and (c) show the full response from 200 to 600ms, covering the transition from steady-state operation to fault occurrence, phase opening, and sequence-component suppression. The corresponding magnified views over the 400–550ms interval are provided in subplots (b) and (d), respectively. The suppression of the sequence components exhibits a more oscillatory behaviour compared to the single-phase open case shown in Figure 5.3, although the time required for sequence suppression remains similar—approximately 40ms for the positive-sequence component and 120ms for the negative- and zero-sequence

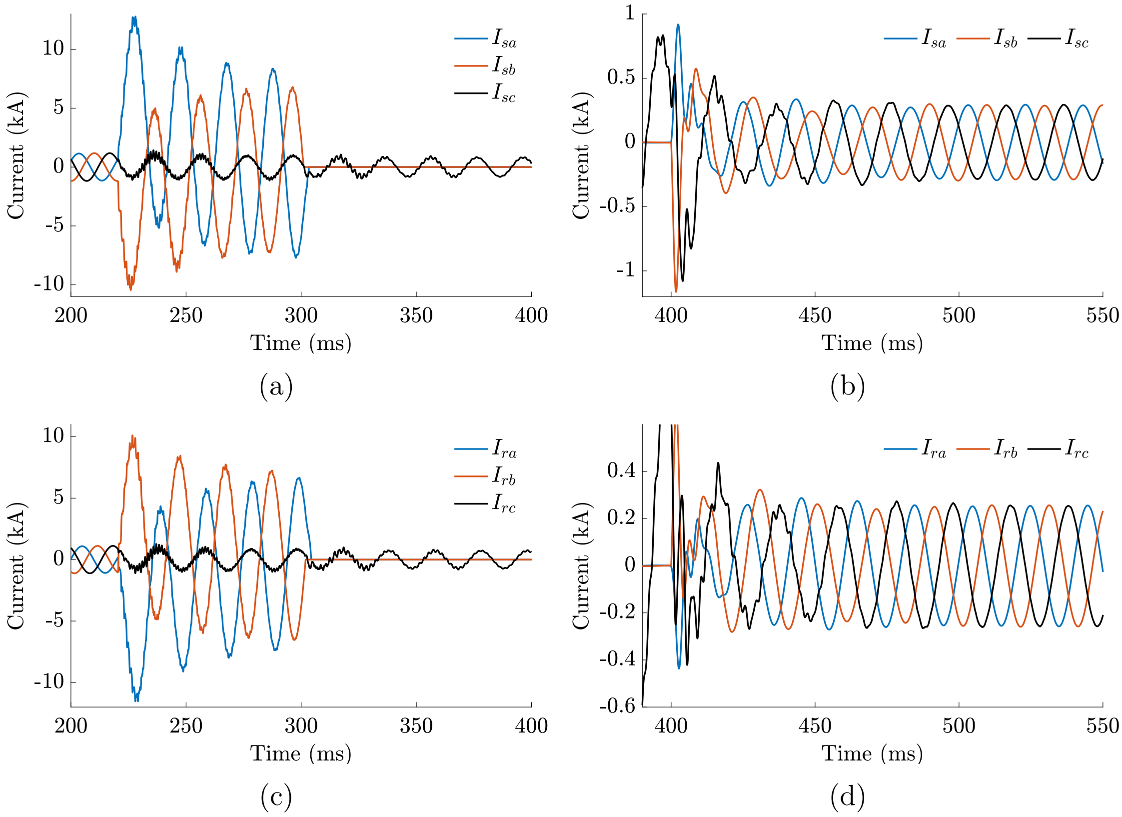

Figure 5.8 Sending- and receiving-end phase currents during the two-phase-to-ground short circuit, fault clearance, and OPAO.

components. A slight increase in the positive-sequence current is observed following the suppression of the negative- and zero-sequence components, as also noted in the single-phase open scenario.

Figure 5.10 presents the output phase currents of E-STATCOM-1 and E-STATCOM-2, shown in subplots (a) and (b), respectively. The currents are measured at the high-voltage sides of transformers T_1 and T_2. In the OPAO case, since the negative- and zero-sequence components are equal, the injected currents at both extremities differ from those in Figure 5.4, exhibiting the highest current in the c-phase.

A comprehensive summary of the sequence-component current magnitudes for the two-phase open scenario is provided in Table 5.5. The table reports the sending- and receiving-end values after fault clearance, before sequence-current injection, and one second after sequence-current injection, together with the injected components supplied by E-STATCOM-1 and E-STATCOM-2. Since no positive-sequence current is injected, the pre-fault power flow is not restored. The suppression of the negative- and zero-sequence current components gives rise to a positive-sequence current of about 20A at both ends. As in the case of AO with one open phase (Section 5.2), the injected currents are higher than the measured ones. This can be attributed to

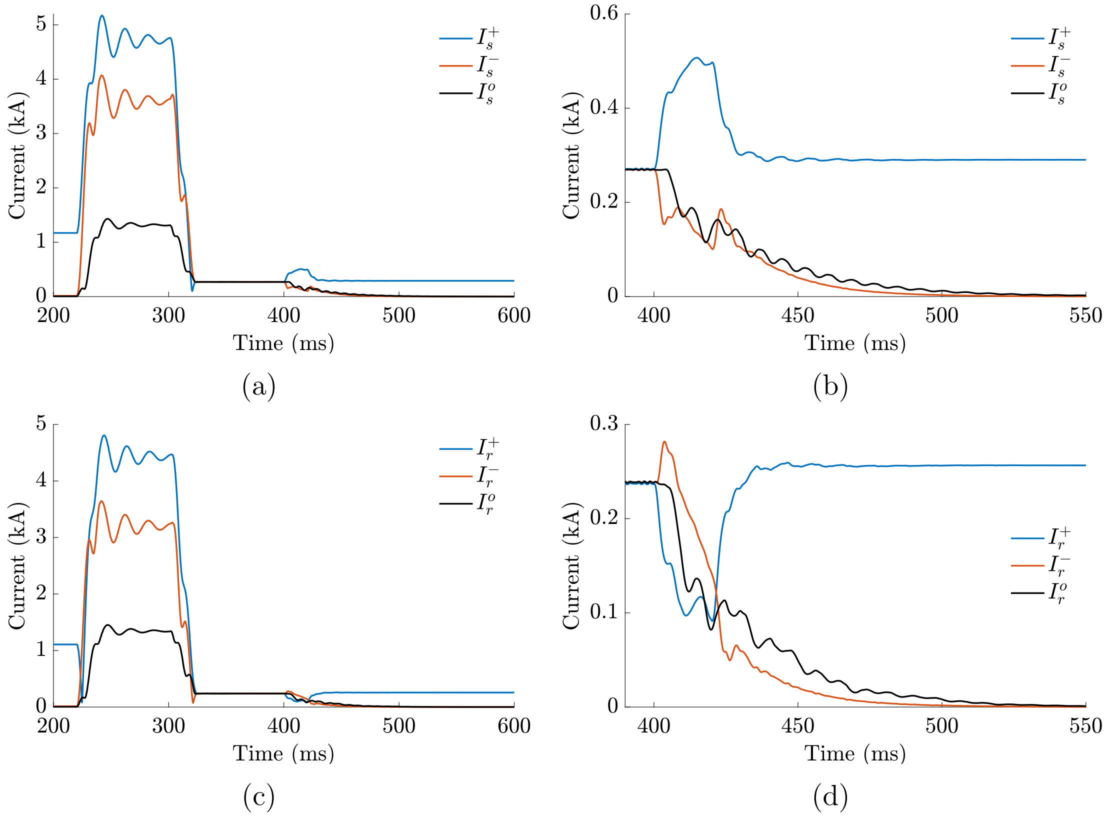

Figure 5.9 Sending- and receiving-end sequence-component currents during fault occurrence, phase opening, and sequence-component suppression.

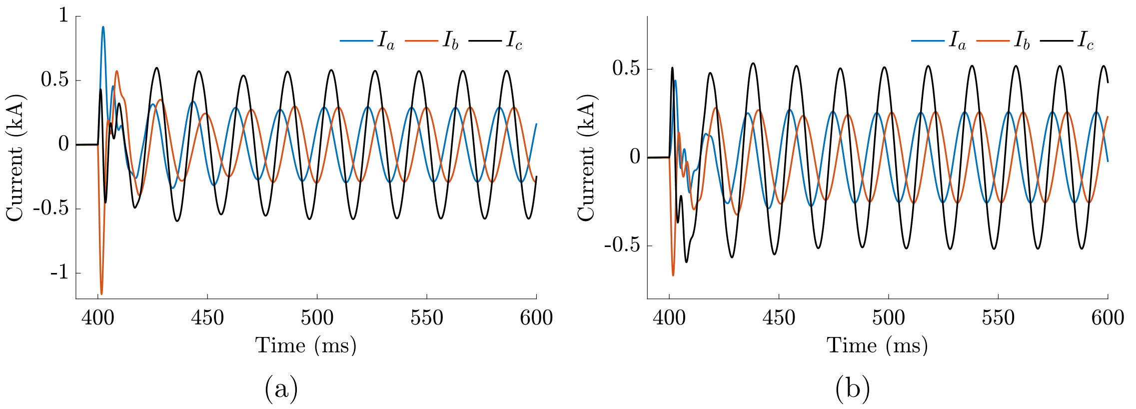

Figure 5.10 Output phase currents of E-STATCOM-1 and E-STATCOM-2 in the OPAO case.

different types of losses, electromagnetic interactions, and the influence of ground resistance.

Similar to Table 5.3, Table 5.6 presents the negative- and zero-sequence current magnitudes as percentages of the positive-sequence component at both ends of the line. The values are reported for the steady-state balanced condition and for the

Table 5.5 Sequence-component current magnitudes for the two-phase AO scenario.

Seq. comp. current (A)	After fault clearance	400ms after seq. injection	Seq. comp. injected by E-STATCOM
Sending end			
+	271.27	290.34	1.62
−	269.73	0.093	288.82
0	269.73	0.07	288.82
Receiving end			
+	236.28	256.59	1.63
−	237.92	0.0012	258.23
0	237.92	0.086	258.23

condition one second after sequence-component suppression. Notably, the third column in both tables is identical, as the steady-state pre-fault condition remains the same for AO with either one or two open phases. After sequence-component suppression, the three-phase currents become more balanced in both scenarios, and the results for negative-sequence suppression are comparable. However, zero-sequence suppression yields significantly higher percentages in the OPAO case than in the TPAO case.

Table 5.6 Negative- and zero-sequence current magnitudes relative to the positive-sequence component in the OPAO case.

	Seq. component	Steady-state condition	After seq.-component suppression
Sending end	I_-/I_+	1.21%	0.032%
	I_0/I_+	0.39%	0.024%
Receiving end	I_-/I_+	1.36%	0.00045%
	I_0/I_+	0.41%	0.033%

5.3.2 One-phase AO with pre-fault power flow restoration

The principles discussed in Subsection 5.2.2, together with the control references defined by Equations 5.1 and 5.2, are equally applicable to the OPAO scenario. As anticipated, the post-fault positive-sequence currents, $|I^+_{s.posf}|$ and $|I^+_{r.posf}|$, are lower compared with the OPAO case (Tables 5.2 and 5.5). This reduction necessitates higher power injection from the batteries of E-STATCOM-1 and E-STATCOM-2 in order to fully, or at least partially, restore the pre-fault power transfer capability.

The OPAO case with pre-fault power flow restoration exhibits behaviour similar to that observed in the TPAO case, as expected. The increased power transfer requires higher power absorption at the sending end and greater power injection at the receiving end. Figure 5.11 presents the positive-sequence component currents at the sending and receiving ends for four different values of k_{id}^{+}, namely 0, 0.25, 0.75, and 1. These currents are shown in subplots (a) and (c), respectively, while the associated SoC profiles of E-STATCOM-1 and E-STATCOM-2 are shown in subplots (b) and (d). As k_{id}^{+} increases, E-STATCOM-1 charges more rapidly, while E-STATCOM-2 discharges at a faster rate.

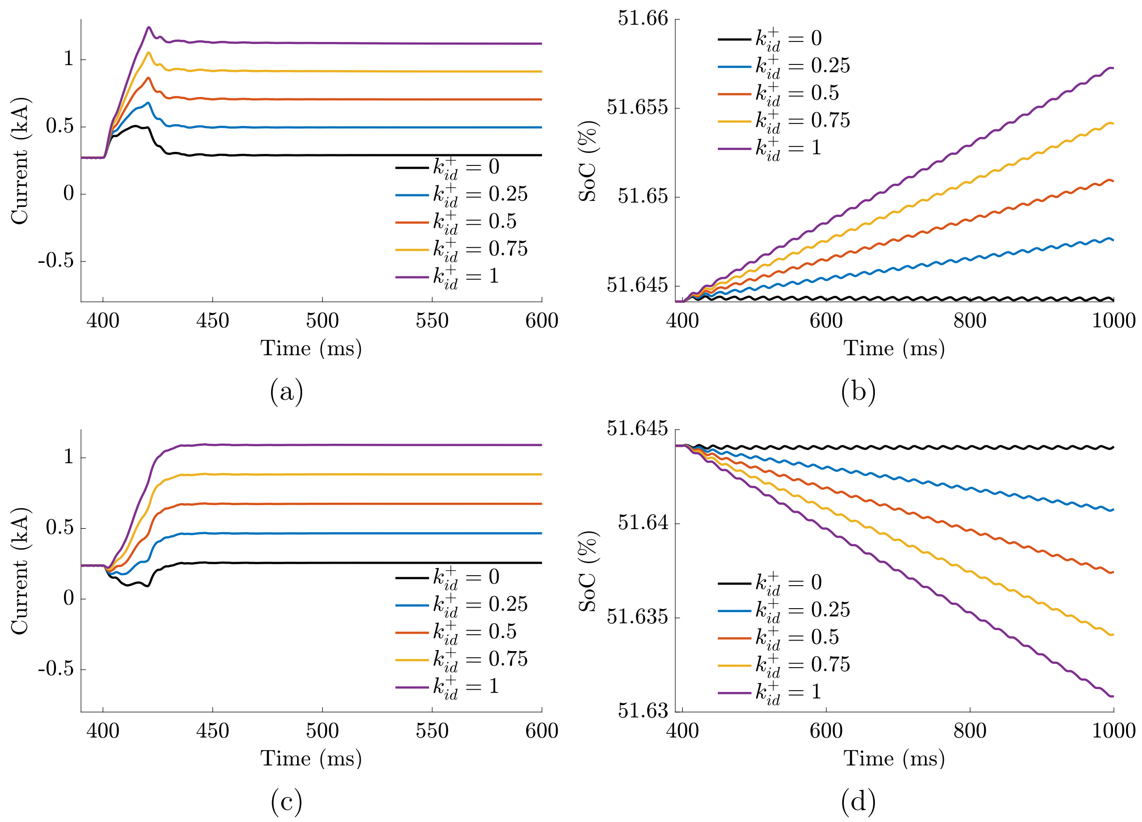

Figure 5.11 Positive-sequence currents and E-STATCOM SoC profiles for different k_{id}^{+} values.

Figure 5.12 illustrates the suppression of the negative- and zero-sequence current components and the injection of the positive-sequence component for the most challenging scenario, corresponding to $k_{id}^{+} = 1$. The sending- and receiving-end responses are shown in subplots (a) and (b), respectively. The suppression of the negative- and zero-sequence current components is similar, in terms of the time required for suppression, to the case with full pre-fault power restoration in TPAO described in Subsection 5.2.2, where the positive-sequence current at the sending end exhibits a small overshoot. However, since the negative-sequence current has a lower magnitude in OPAO, it reaches values close to zero faster than in the TPAO case with full pre-fault power restoration.

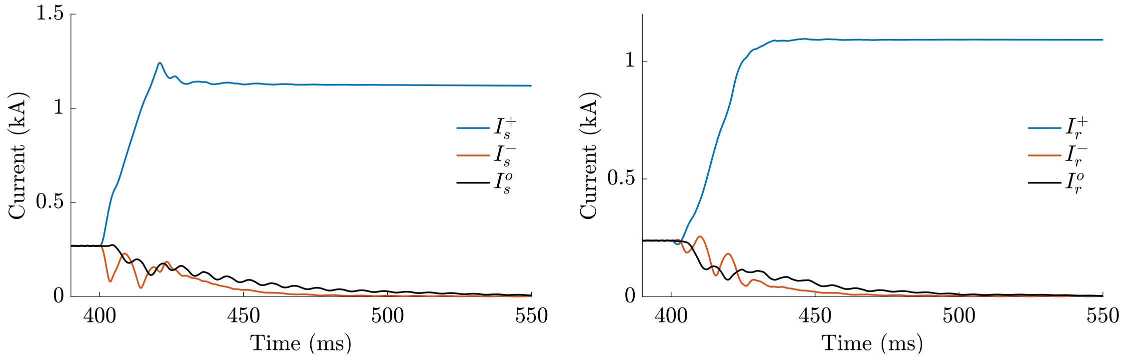

(a) (b)

Figure 5.12 Sequence-component current suppression and positive-sequence injection for $k_{id}^{+} = 1$.

The output currents of E-STATCOM-1 and E-STATCOM-2 for $k_{id}^{+} = 1$ under OPAO are depicted in Figure 5.13. The currents are measured at the high-voltage sides of transformers T_1 and T_2 and are shown in subplots (a) and (b), respectively.

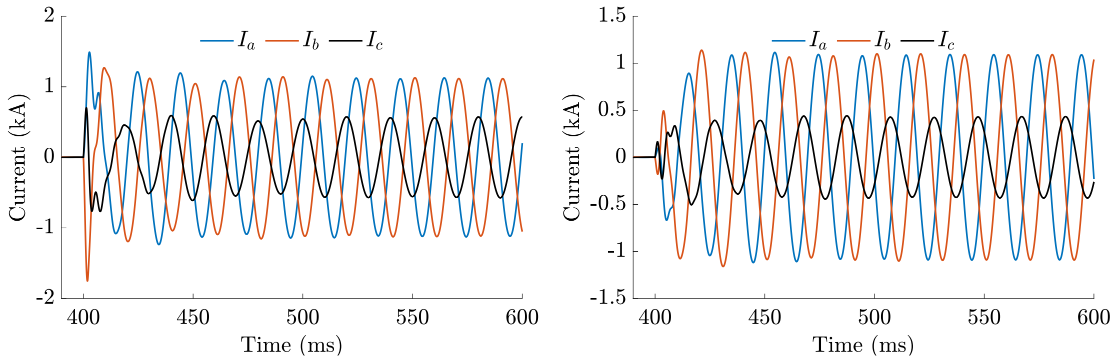

(a) (b)

Figure 5.13 Output currents of E-STATCOM-1 and E-STATCOM-2 for $k_{id}^{+} = 1$ under OPAO.

Table 5.7 summarises the positive-sequence currents and active power at both ends for different k_{id}^{+} coefficients. The reported values were measured 400ms after the activation of E-STATCOM-1 and E-STATCOM-2, corresponding to a time instant of 800ms. For $k_{id}^{+} = 1$, the positive-sequence current magnitudes at both terminals are close to the pre-fault values listed in Table 5.1. The discrepancies, discussed in

Subsection 5.2.2, are approximately doubled due to the presence of two open phases.

Table 5.7 Positive-sequence currents and active power in the OPAO case.

Quantity	$k_{id}^{+} = 0$	$k_{id}^{+} = 0.25$	$k_{id}^{+} = 0.5$	$k_{id}^{+} = 0.75$	$k_{id}^{+} = 1$
$\lvert I_s^+ \rvert$ (A)	290.34	498.07	707.41	916.84	1126.04
$\lvert I_r^+ \rvert$ (A)	256.59	465.62	674.78	883.60	1092.06
P_s (MW)	168.51	300.27	430.83	559.33	684.87
P_r (MW)	156.62	284.95	412.61	538.80	662.73

5.4 Safety considerations

Since all types of TOPL AO considered in this thesis employ ground wires for zero-sequence current flow, the safety aspects of their operation during AO must be carefully addressed. The line modelling work carried out in this thesis allows to review this for the first time. Two main types of ground wire–to–tower connections are commonly used. The first is the conventional configuration, in which the ground wire(s) are directly and electrically connected to the tower tips. The second type involves the use of insulating material between the ground wire(s) and the tower tip.

According to the Russian Federation standard [76], which is also applicable to the Kazakhstan National Power System (NPS), ice accumulation on TOPL ground wire(s) may be melted using DC or AC currents, provided that the ground wire(s) are isolated from the operating power line. The magnitude of these currents is determined according to the formulae provided in the standard. Since, in this case, the ground wire(s) are isolated and the standard permits their connection to AC/DC voltage sources, no significant safety concerns arise under AO conditions.

In this thesis, the first type of connection was investigated, as it involves more complex safety considerations. Since voltage is the main factor determining the electrical hazard, Figure 5.14 illustrates the maximum tower-tip voltages along the line for the entire simulation interval (from 0ms to 1000ms). According to the figure, the highest voltage values are observed at the extremities of the power line.

Figure 5.15 shows the instantaneous tower-tip voltage at 300km during the different stages of operation, including TOPL energisation, the two-phase-to-ground short circuit, fault clearance, and the subsequent operation of E–STATCOMs 1 and 2. The maximum voltage values occur during the short circuit event. Therefore, Figure 5.14 is redrawn to present the maximum voltage distribution along the line, starting from the onset of the E–STATCOM-1 and E–STATCOM-2 operation period (400ms), as illustrated in Figure 5.16. The corresponding phasor values are provided in Appendix C.11. The overall behaviour remains the same, albeit with noticeably reduced voltage magnitudes; the highest values still occur at the TOPL extremities and at the short circuit location. These voltage levels are below 1kV and therefore do not represent high-voltage magnitudes. A further practically favourable observation is that the voltage profile decays exponentially along the line: within less than 10km from either extremity, the tower-tip voltage approaches zero. This characteristic makes the implementation of electrical safety measures—such as installing fences around the terminal towers—both technically justified and economically feasible.

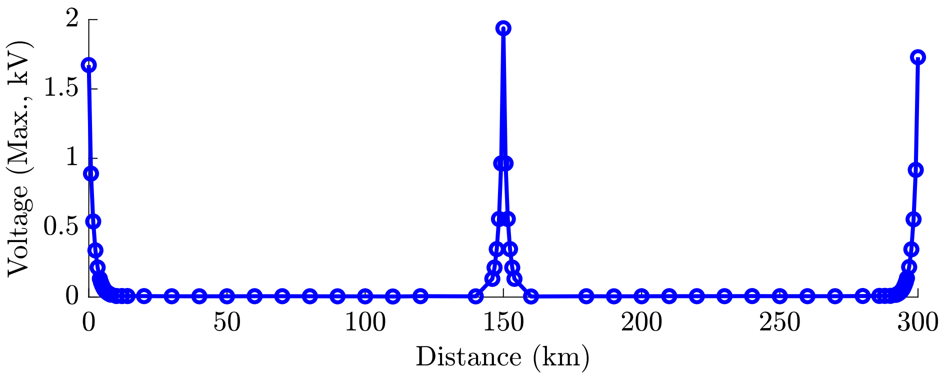

Figure 5.14 Tower-tip maximum voltage versus distance during 0–1000ms interval.

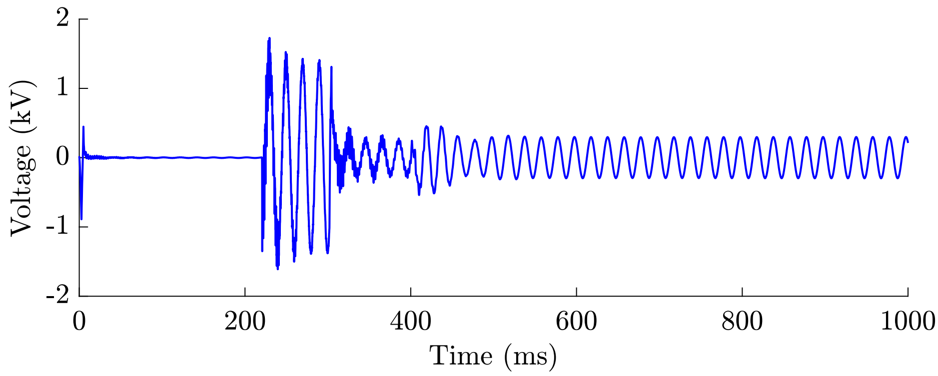

Figure 5.15 Instantaneous value of the tower-tip voltage at 300km.

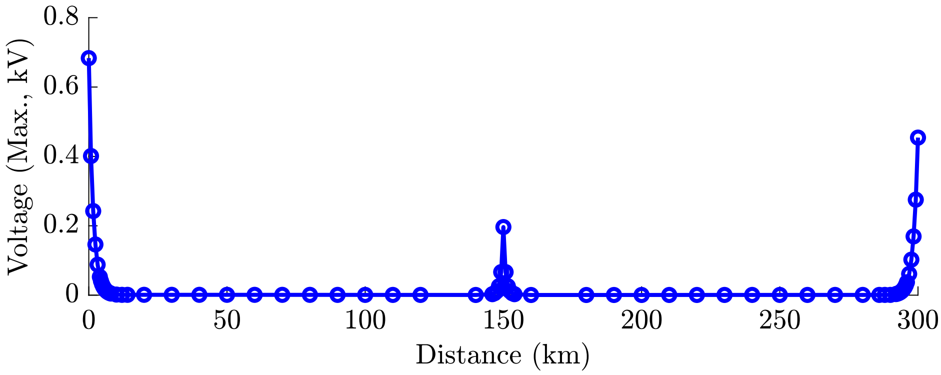

Figure 5.16 Tower-tip maximum voltage versus distance during 400–1000ms interval.

5.5 Conclusion

This chapter has presented the simulation results of the 500kV, 300km transmission line under TPAO and OPAO conditions, both with and without pre-fault power restoration. The 2DF–IMC-based control strategy developed in Chapter 3 demonstrated excellent performance in realising the various types of AO in a long EHV power line.

Without pre-fault power restoration, the active power flow during TPAO and OPAO matches the ratios established in the conclusion of Chapter 4, namely approximately three-fifths and one-fifth of the pre-fault power flow, respectively. Regarding the current sequence components, they are less pronounced during AO than in steady-state operation (Tables 5.1, 5.3, and 5.6).

Overall, the reference-tracking performance across all investigated cases is similar in terms of rise time and transient oscillations. However, a slightly longer time is required to achieve full pre-fault power restoration in OPAO. This is reasonable, as in this scenario only one phase remains operational; therefore, the return current paths are strongly influenced by the ground-wire and earth parameters, and the amount of energy that must be absorbed and injected is approximately four-fifths of the total.

Last but not least, safety considerations were addressed by analysing the voltage profile along the line during AO, as well as the tower-tip voltage at the receiving end in the time domain. Specifically, (i) Figure 5.15 demonstrates that the tower-tip voltage is higher during a two-phases-to-ground fault than during OPAO; and (ii) Figure 5.16 indicates that the resulting voltage levels may be acceptable for the practical realisation of AO in TOPLs.

The next chapter presents the overall thesis conclusions and provides a personal reflection on the research. It also outlines potential research questions that may help complete the broader picture of AO of TOPLs.

Chapter 6

Conclusions and Future Works

6.1 Conclusions

This thesis has investigated the modelling, control, and system-level implications of Asymmetric Operation (AO) of Extra-High-Voltage (EHV) overhead transmission lines. The principal objective was to assess, through detailed simulation studies, whether AO can be treated as a technically credible operating concept for further investigation by transmission system operators, rather than as a purely theoretical idea.

The research questions formulated in Chapter 1 are addressed as follows.

First, this work has shown that the assessment of asymmetric operation requires a physically accurate electromagnetic representation of the transmission line. To this end, a full three-phase distributed-parameter overhead power line simulation model was developed, explicitly accounting for ground wires, tower coupling, and earth return paths. Comparative analyses against conventional π-section models showed that simplified representations may not adequately capture key current distributions, zero-sequence circulation, and transient behaviour under asymmetric conditions. The proposed model therefore provides a more appropriate analytical basis for studying operability, and safety-related indicators during AO.

Second, the thesis has shown that one of the primary technical challenges associated with sustained AO—namely the presence of negative- and zero-sequence currents—can be mitigated through converter-based support. A filterless two-degree-of-freedom internal-model-control (2DF–IMC) strategy was developed for E-STATCOMs, enabling fast and selective suppression of sequence components in simulation. The results demonstrated that both negative- and zero-sequence currents can be substantially reduced within a few fundamental cycles, without reliance on resonant filters or narrow-band signal processing. This indicates an improvement over conventional PI-and PR-based control approaches in the studied cases and suggests that such control structures may be well suited to the fast dynamics of converter-dominated systems.

Third, by combining the proposed line model and control framework, this thesis has demonstrated, in a simulation environment, the sustained asymmetric operation of a representative 500kV, 300km overhead transmission line following single-phase and two-phase fault conditions. The results indicate that AO can maintain controlled power transfer, limit current unbalance, and preserve acceptable voltage profiles at both line terminals under the considered scenarios. Tower-tip voltage analyses further suggest that safety-related constraints may be satisfied when AO is combined with appropriate sequence-current management. These findings address important technical concerns associated with AO, while recognising that additional validation would be required before practical implementation could be considered.

From a scientific perspective, this work extends earlier contributions to power-line asymmetric operation, most notably those of A. Sana. Previous studies established the conceptual basis of AO but relied on simplified network models and did not fully address electromagnetic accuracy, transient performance, or compatibility with modern power-electronic control. In contrast, this thesis provides a more physically grounded modelling framework, a converter-based control strategy for sequence-current mitigation, and a detailed simulation-based validation on a representative EHV transmission corridor. As such, it contributes to the state of the art by clarifying the technical conditions under which AO may be achievable.

From a practical viewpoint, the findings suggest that AO could offer potential resilience benefits in transmission systems with high penetration of inverter-based resources. In particular, AO may reduce the need for full-line tripping following certain asymmetrical faults, support partial power transfer during post-fault conditions, and mitigate the loss of large generation blocks connected along long corridors. These potential benefits are especially relevant in power systems operating with increased reliance on power-electronic interfaces.

However, these benefits must be weighed against the additional cost, complexity, and operational requirements associated with AO. The deployment of E-STATCOMs or other converter-based support devices specifically for AO may require significant capital investment, additional control and communication infrastructure, and more complex protection coordination. Furthermore, the value of AO will depend strongly on system topology, fault statistics, loading conditions, reliability requirements, and the availability of alternative resilience measures such as network reinforcement, redundancy, FACTS devices, or HVDC links. Therefore, AO should not be viewed as a universally applicable solution, but rather as a potential operational option whose technical and economic justification must be assessed on a case-by-case basis.

At the same time, the results of this thesis highlight several challenges that must be addressed before deployment of AO could be considered. These include coordination with protection systems, interactions between multiple converter-interfaced devices under unbalanced operation, and the development of operational procedures compatible with existing grid codes and regulatory requirements. In addition, the economic implications of deploying E-STATCOMs for AO support, as well as their integration with other FACTS and HVDC installations, require further investigation.

In summary, this thesis establishes asymmetric operation of EHV overhead transmission lines as a technically credible concept under the simulated conditions studied. By addressing key modelling, control, and safety-related challenges, it moves AO beyond preliminary conceptual analysis and provides a foundation for further research, experimental validation, techno-economic assessment, and eventual field-oriented evaluation.

6.2 Future Work

While this thesis has provided a simulation-based assessment of AO of EHV overhead transmission lines, several important avenues for future research remain before large-scale deployment or practical adoption can be considered.

Protection systems and fault management

One of the most critical areas for future work concerns the interaction between AO and transmission-line protection schemes. Conventional protection systems are designed under the assumption of symmetrical three-phase operation and may misinterpret sustained unbalanced conditions as persistent faults. Future research should therefore investigate adaptive and AO-aware protection strategies capable of distinguishing intentional asymmetric operation from genuine fault conditions. This includes the behaviour of distance, differential, and ground-fault relays under AO, as well as the coordination between primary protection and backup schemes during transitions between symmetric and asymmetric states.

Grid codes and regulatory frameworks

Another key challenge lies in the compatibility of AO with existing grid codes and regulatory requirements. Current standards typically impose strict limits on voltage unbalance, negative-sequence currents, and zero-sequence injection, without considering controlled AO as a permissible operating mode. Future work should therefore assess how AO could be incorporated into grid codes, either as a temporary post-fault operating state or as an explicitly allowed contingency strategy. This includes defining acceptable unbalance limits, duration thresholds, monitoring requirements, and coordination responsibilities between transmission system operators and converter-interfaced devices.

Techno-economic assessment

A dedicated techno-economic assessment is required to determine whether the benefits of AO justify the additional investment and operational complexity. Future studies should compare AO-supported operation against alternative solutions such as additional transmission capacity, dynamic line rating, network reconfiguration, FACTS devices, HVDC support, or conventional redundancy. Such analysis should include capital cost, operational cost, expected fault occurrence, avoided energy not supplied, reliability improvement, maintenance requirements, and the potential value of enhanced resilience. This would allow AO to be evaluated not only as a technical concept, but also as an economically justified operational strategy.

Extension to low- and medium-voltage networks

Although this thesis has focused on EHV transmission systems, asymmetric operation may also be relevant at lower voltage levels, particularly in converter-dominated distribution networks. Future research could explore the applicability of AO concepts in medium- and low-voltage grids with high penetration of distributed generation, where single-phase connections and inherent asymmetries are already common. The impact of AO on power quality, neutral currents, protection coordination, and customer equipment at these voltage levels warrants detailed investigation.

Active zero-sequence current control

In this thesis, zero-sequence currents are mitigated through suppression strategies based on a three-leg four-wire converter configuration. Future work could move beyond mitigation towards the active and deliberate control of zero-sequence currents. In particular, converter topologies equipped with a dedicated fourth leg or multi-wire interfaces offer the possibility of independently regulating zero-sequence components. This capability could be exploited not only to suppress unwanted currents but also to actively shape current distribution, manage ground return paths, and support novel asymmetric operating modes.

Advanced converter topologies and coordinated control

Further research is also required to assess the role of alternative converter topologies and coordinated multi-device control during AO. This includes the interaction between multiple E-STATCOMs, HVDC converters, and other FACTS devices operating simultaneously under asymmetric conditions. Issues such as control interaction, stability margins, communication requirements, and robustness against measurement noise and parameter uncertainty should be examined, particularly in large interconnected systems.

Experimental validation and field demonstration

Finally, while this thesis has relied on detailed electromagnetic and control-oriented simulations, experimental validation remains an essential next step. Hardware-in-the-loop testing and pilot-scale field demonstrations would provide valuable insight into practical implementation challenges, including measurement noise, converter non-idealities, communication delays, switching constraints, thermal limits, and protection coordination. Such studies would be necessary to build confidence among system operators and to determine whether AO can progress from a simulation-supported concept to an operationally deployable strategy.

In summary, future research should focus not only on refining the technical aspects of asymmetric operation, but also on evaluating its protection, regulatory, operational, and economic implications. Addressing these challenges will be essential for determining whether AO can become a cost-effective resilience-enhancing option in converter-dominated grids.

Bibliography

[1] Minwu Chen, Siyang Liu, Jiuguo Zhu, Chonghao Xie, Hang Tian, and Jianjun Li. Effects and characteristics of ac interference on parallel underground pipelines caused by an ac electrified railway. *Energies*, 11(9), 2018. ISSN 1996-1073. doi: 10.3390/en11092255. URL https://www.mdpi.com/1996-1073/11/9/2255.

[2] A.-R. Sana, R.J. Marceau, C. Todde, D.X. Do, J. Mahseredjian, and G. Joos. The exploitation of asymmetry in electric power transmission networks. In *Conference Proceedings. IEEE Canadian Conference on Electrical and Computer Engineering (Cat. No.98TH8341)*, volume 2, pages 485–488 vol.2, 1998. doi: 10.1109/CCECE.1998.685539.

[3] Amirnaser Yazdani. *Voltage-sourced converters in power systems [internet resource] modeling, control, and applications*. Wiley, Oxford, 2010. ISBN 9780470551561.

[4] MathWorks. Battery — generic battery model (simscape specialized power systems), 2024. URL https://uk.mathworks.com/help/releases/R2024b/sps/powersys/ref/battery.html. Accessed: 2025-08-31.

[5] MathWorks. Three-phase pi section line. https://uk.mathworks.com/help/sps/powersys/ref/threephasepisectionline.html. Accessed: 2024-08-26.

[6] International Energy Agency (IEA). Renewables — energy system, September 2025. URL https://www.iea.org/energy-system/renewables. [online] https://www.iea.org/energy-system/renewables.

[7] Jingyang Fang, Hongchang Li, Yi Tang, and Frede Blaabjerg. On the inertia of future more-electronics power systems. *IEEE Journal of Emerging and Selected Topics in Power Electronics*, 7(4):2130–2146, 2019. doi: 10.1109/JESTPE.2018.2877766.

[8] C Todde, Richard J Marceau, DT McGillis, S Lefebvre, and A-R Sana. An investigation into the compensation of asymmetric systems. In *Engineering Solutions for the Next Millennium. 1999 IEEE Canadian Conference on Electrical and Computer Engineering (Cat. No. 99TH8411)*, volume 2, pages 1187–1190. IEEE, 1999.

[9] A. R. Sana, Richard J. Marceau, D. T. McGillis, C. Todde, and Xuan-Dai Do. On the asymmetrical operation of transmission systems. In *CIGRE Symposium on Working Plant and Systems Harder*, pages 400.011–400.016–400.011–400.016, 1999. URL https://publications.polymtl.ca/28611/. ARRAY(0x5587225ee388).

[10] A.-R. Sana. *Exploitation asymétrique des réseaux de transport d'énergie électrique*. Thèse de doctorat, École Polytechnique de Montréal, 2001. URL https://publications.polymtl.ca/7074/.

[11] David Campos-Gaona, Rafael Peña-Alzola, Jose Luis Monroy-Morales, Martin Ordonez, Olimpo Anaya-Lara, and William E. Leithead. Fast selective harmonic mitigation in multifunctional inverters using internal model controllers and synchronous reference frames. *IEEE Transactions on Industrial Electronics*, 64 (8):6338–6349, 2017. doi: 10.1109/TIE.2017.2682003.

[12] M. Whelan, Steve Rockwell, and Thomas Blalock. Great barrington 1886: Inspiring an industry toward ac power, August 2024. URL https://edisontechcenter.org/GreatBarrington.html. [online] https://edisontechcenter.org/GreatBarrington.html.

[13] Edison Tech Center. Harnessing niagara falls: The adams power station. the most famous of early hydroelectric power stations, August 2024. URL https://edisontechcenter.org/Niagara.htm. [online] https://edisontechcenter.org/Niagara.htm.

[14] Bruce Elwyn Meserve. *Fundamental concepts of algebra*. Courier Corporation, 1982.

[15] Morris Brenna, Federica Foiadelli, and Dario Zaninelli. *Electrical Railway Transportation Systems*. IEEE Press Series on Power Engineering. Wiley, 1 edition, 2018. ISBN 9781119386803.

[16] Balwinder Singh Samra. *An analysis of single wire earth return (SWER) system for rural electrification*. University of Missouri–Rolla, 1972.

[17] Ralph Karhammar, Arun Sanghvi, Eric Fernstrom, Moncef Aissa, Jabesh Arthur, John Tulloch, Ian Davies, Sten Bergman, and Subodh Mathur. Sub-saharan africa: Introducing low-cost methods in electricity distribution networks. *ESMAP Technical Paper*, 104(06), 2006.

[18] Izael Da Silva. The use of single wire earth return (swer) as a potential solution to reduce the cost of rural electrification in uganda. 04 2001.

[19] Benar, P.P. Electric power transmission «two wires – earth» (in Russian). *Elektrichestvo*, (20):13–20, 1933. URL https://www.booksite.ru/elektr/1933/1933_20.pdf. Accessed: 2024-09-18.

[20] N.S. Buryanina, Yu.F. Korolyuk, and E.V. Lesnykh. Using "two wires – earth" power transmission lines. *Proceedings of Irkutsk State Technical University*, 21 (3):91–99, 2017. doi: 10.21285/1814-3520-2017-3-91-99. URL https://journals.istu.edu/vestnik_irgtu/journals/2017/03/articles/09?view=0. (In Russian).

[21] Oskar Edwin Edison. *Regulation of open delta connected transformers*. The University of Nebraska-Lincoln, 1915.

[22] George P Roux. Delta-cross connections of transformers. *Transactions of the American Institute of Electrical Engineers*, 34(2):2141–2155, 1915.

[23] R. Marceau, D. McGillis, and A. Sana. The role of asymmetric operation in enhancing the flexibility of power system operation. In *CCECE 2003 - Canadian Conference on Electrical and Computer Engineering. Toward a Caring and Humane Technology (Cat. No.03CH37436)*, volume 1, pages 509–514 vol.1, 2003. doi: 10.1109/CCECE.2003.1226448.

[24] R.J. Marceau, D.T. McGillis, and A.R. Sana. *Asymmetric Operation of AC Power Transmission Systems: The Key to Optimizing Power System Reliability and Economics*. Presses internationales Polytechnique, 2006. ISBN 9782553014031. URL https://books.google.co.uk/books?id=sPJL7srlQaUC.

[25] Ahmed Zobaa, Mario Mañana Canteli, and Ramesh Bansal, editors. *Power Quality: Monitoring, Analysis and Enhancement*. IntechOpen, London, September 2011. ISBN 9789533073309. doi: 10.5772/1425. URL https://doi.org/10.5772/1425.

[26] R. A. Otto, T. H. Putman, and L. Gyugyi. Principles and applications of static, thyristor-controlled shunt compensators. *IEEE Transactions on Power Apparatus and Systems*, PAS-97(5):1935–1945, 1978. doi: 10.1109/TPAS.1978.354690.

[27] A-R Sana, D McGillis, RJ Marccau, Xuan-Dai Do, and Guy Olivier. Asymmetrical operation of corridor with one single line. In *2000 Canadian Conference on Electrical and Computer Engineering. Conference Proceedings. Navigating to a New Era (Cat. No. 00TH8492)*, volume 2, pages 936–940. IEEE, 2000.

[28] Ansar Berdygozhin, Benjamin Pepper, and David Campos-Gaona. Asymmetric operation of power lines by using e-statcom and internal model controllers. In *2024 IEEE 15th International Symposium on Power Electronics for Distributed Generation Systems (PEDG)*, pages 1–6, 2024. doi: 10.1109/PEDG61800.2024.10667369.

[29] HVDC Ground Electrode Overview. Technical report, Electric Power Research Institute (EPRI), Palo Alto, CA (United States), 2010. URL https://www.epri.com/research/products/1020116.

[30] R. J. Holt, J. Dabkowski, and R. L. Hauth. HVDC Power Transmission Electrode Siting and Design. Technical report, New England Power Service Company, 25 Research Drive, Westborough, 1997.

[31] Durgesh Singh Yadav, Bhavna Jaiswal, Meenu Gautam, and Madhoolika Agrawal. *Soil acidification and its impact on plants*. Springer, 2020.

[32] General Guidelines for HVDC Electrode Design. Tech. Brochure WG B4.61, CIGRÉ, 2017.

[33] R. Mohamedi, S. Lefebvre, A-O. Ba, and A. Houle. Comparative study of the symmetric and asymmetric approaches to increase power transfer capacity of a corridor. In *2007 iREP Symposium - Bulk Power System Dynamics and Control - VII. Revitalizing Operational Reliability*, pages 1–7, 2007. doi: 10.1109/IREP.2007.4410512.

[34] R. M Mathur. *Thyristor-based FACTS controllers for electrical transmission systems / [internet resource]*. IEEE Press series on power engineering. IEEE, Piscataway, New Jersey, 2002. ISBN 9780470546680.

[35] R. Mohamedi, S. Lefebvre, A-O. Ba, and A. Houle. Increasing the transfer capacity of a corridor through power flow control. In *2007 IEEE Canada Electrical Power Conference*, pages 507–513, 2007. doi: 10.1109/EPC.2007.4520384.

[36] Guy Roméo Mougnol Assala, Jean-Jacques Mandeng, Charles Hubert Kom, and Jean Mbihi. Grid-tied pv system-based power compensation of a grid equipped with dual interphase power controllers (ipc) 240 with three branches: case of a short transmission line. *Energy Systems*, pages 1–21, 2023.

[37] Kengne Chatue Charlène Steva, Mengata Mengounou Ghislain, Koko Koko Joseph, Batassou Guilzia Jeannot, and Nneme Nneme Leandre. Contribution to asymmetrical compensation through parallel controllers of facts (statcom)—ipc 240 dual for a power transmission line. *World Journal of Engineering and Technology*, 11(1):20–40, 2022.

[38] N. N. Belyakov, V. L. Volchek, V. V. Ilyinichin, S. B. Losev, Yu. I. Lyskov, V. N. Novella, V. S. Rashkes, V. M. Strelkov, G. G. Fokin, and M. I. Khoroshev. Application of single-phase autoreclosing in a complex ehv network containing 1200 kv transmission lines. In *Protection and Automation (B5) Committee Session Materials*, pages 34–207, 1990. [online] https://www.e-cigre.org/publications/detail/34-207-1990-application-of-single-phase-autoreclosing-in-a-complex-ehv-network-containing-1.html (accessed: 2024-08-28).

[39] Kazakhstan Government. Concept on transition towards green economy until 2050, 2013. URL https://policy.asiapacificenergy.org/node/133#:~:text=KAZAKHSTAN%3A%20Concept%20on%20Transition%20towards%20Green%20Economy%20until%202050&text=The%20Concept%20aims%20to%20increase,the%20energy%20security%20of%20Kazakhstan. Accessed: 2024-08-28.

[40] Piotr Pruski and Stefan Paszek. Analysis of transient waveforms in a power system at asymmetrical short-circuits. *Prz. Elektrotech*, 2:26–29, 2020.

[41] L. Asiminoaei, F. Blaabjerg, and S. Hansen. Evaluation of harmonic detection methods for active power filter applications. In *Twentieth Annual IEEE Applied Power Electronics Conference and Exposition, 2005. APEC 2005.*, volume 1, pages 635–641 Vol. 1, 2005. doi: 10.1109/APEC.2005.1453014.

[42] Sergio Alejandro Gonzalez, Rogelio Garcia-Retegui, and Mario Benedetti. Harmonic computation technique suitable for active power filters. *IEEE Transactions on Industrial Electronics*, 54(5):2791–2796, 2007. doi: 10.1109/TIE.2007.894789.

[43] Lucian Asiminoael, Frede Blaabjerg, and Steffan Hansen. Detection is key - harmonic detection methods for active power filter applications. *IEEE Industry Applications Magazine*, 13(4):22–33, 2007. doi: 10.1109/MIA.2007.4283506.

[44] Eda Uz-Logoglu, Ozgul Salor, and Muammer Ermis. Real-time detection of interharmonics and harmonics of ac electric arc furnaces on gpu framework. In *2017 IEEE Industry Applications Society Annual Meeting*, pages 1–8, 2017. doi: 10.1109/IAS.2017.8101814.

[45] R. Teodorescu, F. Blaabjerg, U. Borup, and M. Liserre. A new control structure for grid-connected lcl pv inverters with zero steady-state error and selective harmonic compensation. In *Nineteenth Annual IEEE Applied Power Electronics Conference and Exposition, 2004. APEC '04.*, volume 1, pages 580–586 Vol.1, 2004. doi: 10.1109/APEC.2004.1295865.

[46] P. Rodríguez, R. Teodorescu, I. Candela, A. V. Timbus, M. Liserre, and F. Blaabjerg. New positive-sequence voltage detector for grid synchronization of power converters under faulty grid conditions. In *2006 37th IEEE Power Electronics Specialists Conference*, pages 1–7, 2006. doi: 10.1109/pesc.2006.1712059.

[47] Hirofumi Akagi. *Instantaneous power theory and applications to power conditioning*. IEEE Press series on power engineering. Wiley ; IEEE Press, Hoboken, N.J. : Piscataway, N.J., 2007. ISBN 9780470107614.

[48] P.C. Loh, Y. Tang, F. Blaabjerg, and P. Wang. Mixed-frame and stationary-frame repetitive control schemes for compensating typical load and grid harmonics. *IET power electronics*, 4(2):218–226, 2011. ISSN 1755-4535.

[49] Alejandro G. Yepes, Jano Malvar, Ana Vidal, Oscar López, and Jesús Doval-Gandoy. Current harmonics compensation based on multiresonant control in synchronous frames for symmetrical n-phase machines. *IEEE Transactions on Industrial Electronics*, 62(5):2708–2720, 2015. doi: 10.1109/TIE.2014.2365155.

[50] R. Teodorescu, F. Blaabjerg, M. Liserre, and P.C. Loh. Proportional-resonant controllers and filters for grid-connected voltage-source converters. *IEE proceedings. Electric power applications*, 153(5):750–762, 2006. ISSN 1350-2352.

[51] H. Nazifi and A. Radan. Current control assisted and non-ideal proportional-resonant voltage controller for four-leg three-phase inverters with time-variant loads. In *2013 4th Power Electronics, Drive Systems and Technologies Conference*, pages 355–360, NEW YORK, 2013. IEEE, IEEE. ISBN 9781467344814.

[52] Sandeep Sharma, Saket Gupta, Mohd Zuhaib, Vijay Bhuria, Hasmat Malik, Abdulaziz Almutairi, Asyraf Afthanorhan, and Mohammad Asef Hossaini. A comprehensive review on statcom: Paradigm of modeling, control, stability, optimal location, integration, application, and installation. *IEEE Access*, 12: 2701–2729, 2024. doi: 10.1109/ACCESS.2023.3345216.

[53] Tobias Engelbrecht, Andrew Isaacs, Sergey Kynev, Julia Matevosyan, Bernd Niemann, Andrew J. Owens, Biswajit Singh, and Andrea Grondona. Statcom technology evolution for tomorrow's grid: E-statcom, statcom with supercapacitor-based active power capability. *IEEE Power and Energy Magazine*, 21(2):30–39, 2023. doi: 10.1109/MPE.2022.3230969.

[54] Abhishek Malhotra, Benedikt Battke, Martin Beuse, Annegret Stephan, and Tobias Schmidt. Use cases for stationary battery technologies: A review of the literature and existing projects. *Renewable and Sustainable Energy Reviews*, 56: 705–721, 2016. ISSN 1364-0321. doi: https://doi.org/10.1016/j.rser.2015.11.085. URL https://www.sciencedirect.com/science/article/pii/S1364032115013520.

[55] Daiwon Choi, Nimat Shamim, Alasdair Crawford, Qian Huang, Charlie K. Vartanian, Vilayanur V. Viswanathan, Matthew D. Paiss, Md Jan E. Alam,

David M. Reed, and Vince L. Sprenkle. Li-ion battery technology for grid application. *Journal of Power Sources*, 511:230419, 2021. ISSN 0378-7753. doi: https://doi.org/10.1016/j.jpowsour.2021.230419. URL https://www.sciencedirect.com/science/article/pii/S0378775321009253.

[56] Olivier Tremblay and Louis-A. Dessaint. Experimental validation of a battery dynamic model for ev applications. *World Electric Vehicle Journal*, 3(2):289–298, 2009. ISSN 2032-6653. doi: 10.3390/wevj3020289. URL https://www.mdpi.com/2032-6653/3/2/289.

[57] Rolf Ottersten. *On Control of Back-to-Back Converters and Sensorless Induction Machine Drives*. Phd thesis, Chalmers University of Technology, Göteborg, Sweden, 2003.

[58] Manfred Morari. *Robust process control*. Prentice Hall, Englewood Cliffs, N.J., 1989. ISBN 9780137821532.

[59] Ansar Berdygozhin and David Campos-Gaona. Asymmetric operation of power networks, state of the art, challenges, and opportunities. *Energies*, 17(20), 2024. ISSN 1996-1073. doi: 10.3390/en17205021. URL https://www.mdpi.com/1996-1073/17/20/5021.

[60] R. Verma and D. Mukhedkar. Ground fault current distribution in sub-station, tower and ground wire. *IEEE Transactions on Power Apparatus and Systems*, PAS-98(3):724–730, 1979. doi: 10.1109/TPAS.1979.319276.

[61] Conrad F. Desieno, Peter P. Marchenko, and Gregory S. Vassell. General equations for fault currents in transmission line ground wires. *IEEE Transactions on Power Apparatus and Systems*, PAS-89(8):1891–1900, 1970. doi: 10.1109/TPAS.1970.292773.

[62] H. B. Gooi and S. A. Sebo. Distribution of ground fault currents along transmission lines – an improved algorithm. *IEEE Transactions on Power Apparatus and Systems*, PAS-104(3):663–670, 1985. doi: 10.1109/TPAS.1985.319002.

[63] F. Dawalibi and G. B. Niles. Measurements and computation of fault current distribution on overhead transmission lines. *IEEE Power Engineering Review*, PER-4(3):33–34, 1984. doi: 10.1109/MPER.1984.5525534.

[64] John R. Carson. Wave propagation in overhead wires with ground return. *The Bell System Technical Journal*, 5(4):539–554, 1926. doi: 10.1002/j.1538-7305.1926.tb00122.x.

[65] R. Rudenberg. *Transient Performance of Electric Power Systems*. McGraw-Hill Book Company, 1950.

[66] A. Deri, G. Tevan, A. Semlyen, and A. Castanheira. The complex ground return plane a simplified model for homogeneous and multi-layer earth return. *IEEE Transactions on Power Apparatus and Systems*, PAS-100(8):3686–3693, 1981. doi: 10.1109/TPAS.1981.317011.

[67] Anastázia MARGITOVÁ, Martin KANÁLIK, and Michal KOLCUN. Impact of ground wires on the series impedance, voltage and current conditions of overhead power lines. *Acta electrotechnica et informatica*, 19(1):11–18, 2019. ISSN 1335-8243.

[68] Darren Woodhouse. On the theoretical basis of carson's equations. In *2012 IEEE International Conference on Power System Technology (POWERCON)*, pages 1–6, 2012. doi: 10.1109/PowerCon.2012.6401356.

[69] W.H. Wise. Propagation of high-frequency currents in ground return circuits. *Proceedings of the Institute of Radio Engineers*, 22(4):522–527, 1934. doi: 10.1109/JRPROC.1934.225868.

[70] W. H. Kersting and R. K. Green. The application of carson's equation to the steady-state analysis of distribution feeders. In *2011 IEEE/PES Power Systems Conference and Exposition*, pages 1–6, 2011. doi: 10.1109/PSCE.2011.5772579.

[71] John J Grainger. *Power system analysis*. McGraw-Hill series in electrical and computer engineering. McGraw-Hill, New York, 1994. ISBN 0070612935.

[72] MathWorks. Line parameter calculator - simscape electrical, 2024. URL https://uk.mathworks.com/help/releases/R2024b/sps/powersys/ref/lineparametercalculator-app.html. Accessed: 2025-06-11.

[73] J. Duncan Glover. *Power system analysis & design*. Cengage, Boston, MA, seventh edition, si.. edition, 2023. ISBN 9780357676196.

[74] Muhammad Sharjeel Javaid, Balarko Chaudhuri, Fei Teng, and Zohaib Akhtar. Emt — rms modeling trade-off for ibr-driven sub-synchronous oscillations. *IEEE Transactions on Power Systems*, pages 1–12, 2025. doi: 10.1109/TPWRS.2025.3588893.

[75] MathWorks. Distributed parameters line. MATLAB Help Center (Simscape Electrical / Specialized Power Systems) Documentation. URL https://www.mathworks.com/help/sps/powersys/ref/distributedparametersline.html. Accessed: 2026-01-19.

[76] Системы плавки гололеда на проводах и грозозащитных тросах линий электропередачи. ГОСТ Р 59965–2021, 2022. Издание официальное.

Appendix A

Generic Three-Phase Power-Line Model

When electromagnetic transients are not of interest, the power line may be represented using a sequence-domain π-section model. The corresponding equivalent circuit is shown in Fig. A.1, and the parameter relationships are given by (A.1)–(A.6).

$$r_{aa} = \frac{2r^{+} + r^{o}}{3}, \tag{A.1}$$

$$L_{aa} = \frac{2L^{+} + L^{o}}{3}, \tag{A.2}$$

$$r_{ab} = \frac{r^{o} - r^{+}}{3}, \tag{A.3}$$

$$L_{ab} = \frac{L^{o} - L^{+}}{3}, \tag{A.4}$$

$$C = C^{+}, \tag{A.5}$$

$$C_{gr} = \frac{3\,C^{+}C^{o}}{C^{+} - C^{o}}. \tag{A.6}$$

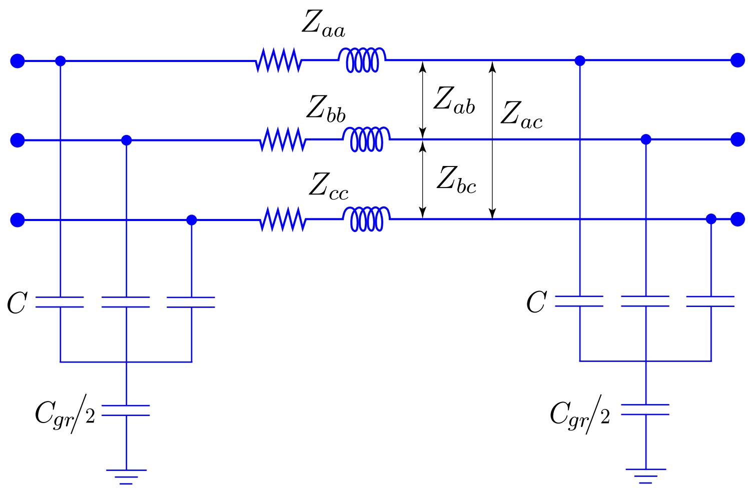

Figure A.1 Power-line model in the sequence domain [5].

Appendix B

Sequence components Clarke and Park transformations

If the positive-sequence dq transformation matrix is defined as

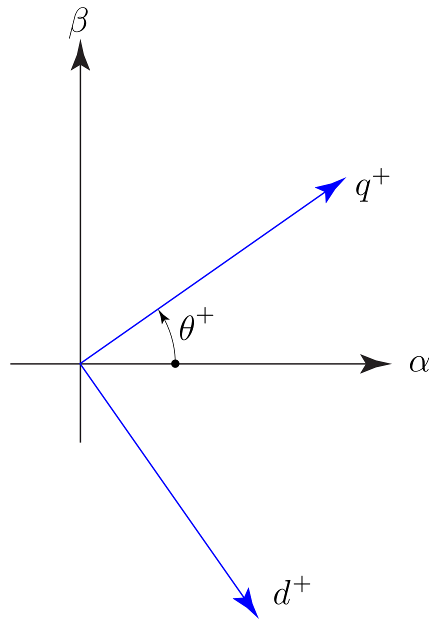

Figure B.1 Transformation between the $\alpha\beta$ reference frame and the positive-sequence dq synchronous reference frame.

$$T_{abc^+ \to \alpha\beta} = \tfrac{2}{3} \begin{bmatrix} 1 & -1/2 & -1/2 \\ 0 & \sqrt{3}/2 & -\sqrt{3}/2 \end{bmatrix} \tag{*}$$

$$T_{\alpha\beta\rightarrow dq^+} = \begin{bmatrix} \sin(\theta) & -\cos(\theta) \\ \cos(\theta) & \sin(\theta) \end{bmatrix} \tag{*}$$

$$T_{abc\rightarrow dq^+} = \frac{2}{3}\begin{bmatrix} \sin(\theta) & \sin\left(\theta - \frac{2\pi}{3}\right) & \sin\left(\theta + \frac{2\pi}{3}\right) \\ \cos(\theta) & \cos\left(\theta - \frac{2\pi}{3}\right) & \cos\left(\theta + \frac{2\pi}{3}\right) \end{bmatrix}, \quad \text{and} \quad \dot{\theta} = \omega t, \tag{*}$$

$$\begin{aligned} \mathbf{x}_{dq^+} &= T_{abc\rightarrow dq^+}\,\mathbf{x}_{abc}, & \mathbf{x}_{abc} &= T_{dq^+\rightarrow abc}\,\mathbf{x}_{dq^+}, \\ \mathbf{I} &= T_{abc\rightarrow dq^+}\,T_{dq^+\rightarrow abc}, & [T_{abc\rightarrow dq^+}]^{-1} &= T_{dq^+\rightarrow abc}. \end{aligned} \tag{B.1}$$

Where, $\mathbf{I}$ - unity matrix, $\theta = \omega t$. For the dq^- reference frame rotating in the opposite direction, with the angular position denoted by θ^- to track the negative-sequence current, the transformation matrix is expressed as

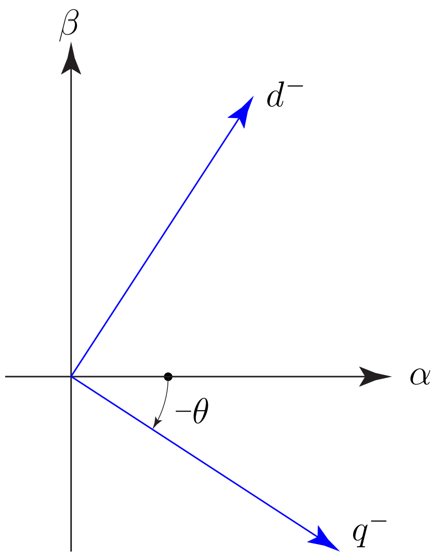

Figure B.2 Transformation between the $\alpha\beta$ reference frame and the negative-sequence dq synchronous reference frame.

$$T_{abc^-\rightarrow\alpha\beta^-} = \frac{2}{3}\begin{bmatrix} 1 & -1/2 & -1/2 \\ 0 & -\sqrt{3}/2 & \sqrt{3}/2 \end{bmatrix} \tag{*}$$

$$T_{\alpha\beta^- \to dq^-} = \begin{bmatrix} \sin(\theta) & -\cos(\theta) \\ \\ \cos(\theta) & \sin(\theta) \end{bmatrix} \tag{*}$$

$$T_{abc \to dq^-} = \frac{2}{3} \begin{bmatrix} -\sin(\omega_s t) & -\sin\Big(\omega_s t + \frac{2\pi}{3}\Big) & -\sin\Big(\omega_s t - \frac{2\pi}{3}\Big) \\ \cos(\omega_s t) & \cos\Big(\omega_s t + \frac{2\pi}{3}\Big) & \cos\Big(\omega_s t - \frac{2\pi}{3}\Big) \end{bmatrix}. \tag{**}$$

$$\begin{aligned} \mathbf{x}_{dq^-} &= T_{abc \to dq^-} \, \mathbf{x}_{abc}, \qquad \mathbf{x}_{abc} = T_{dq^- \to abc} \, \mathbf{x}_{dq^-}, \\ \mathbf{I} &= T_{abc \to dq^-} \, T_{dq^- \to abc}, \qquad [T_{abc \to dq^-}]^{-1} = T_{dq^- \to abc}. \end{aligned} \tag{B.2}$$

Appendix C

Tables

Table C.1 Thévenin equivalent impedance and grid parameters for the 500 kV non-ideal grid

Parameter	**Value**
Grid Short-Circuit Power (S_{sc})	30 GVA
Nominal Grid Voltage	500 kV
Thévenin equivalent resistance (r_{Th})	1.667 Ω
Thévenin equivalent inductance (L_{Th})	26.526 mH

Table C.2 T_1 and T_2 transformer parameters

Parameter	**Value**
Power rating (MVA)	500
HV/LV ratio (kV)	500/20
k_{tr}	25
R_m, L_m (pu)	500, ∞
HV and LV sides	
R, L (pu)	0.002, 0.08

E-STATCOM Parameters

Table of Phasors

Table C.3 E-STATCOM parameters used in the simulation model

$\|S\|$ [MVA]	Battery Type	Capacity [kAh]	$V_{dc}/2$ [kV]	L_f [pu]	r_f [pu]
300	Lithium-ion	12	25	1×10^{-1}	1×10^{-3}

Table C.4 Phasors of I_a at various distances (TPAO, No SC)

Distance [km]	$\|I_a\|$ [A]	$\angle I_a$ [deg]
0	0.00	0.00
20	2.29	−69.98
40	4.61	−70.10
60	6.96	−70.23
80	9.35	−70.37
100	11.77	−70.51
120	11.55	−74.92
140	11.42	−79.51
150	11.39	−81.86
160	11.40	−84.21
180	11.48	−88.94
200	11.66	−93.59
220	9.26	−93.41
240	6.89	−93.21
250	5.72	−93.10
260	4.56	−93
280	2.26	−92.76
300	0.00	148.24

Table C.5 Phasors of I_a at various distances (TPAO, SC at 150km)

Distance [km]	$\lvert \boldsymbol{I_a} \rvert$ **[A]**	$\angle \boldsymbol{I_a}$ **[deg]**
0	0.00	0.00
20	3.63	−136.20
40	7.29	−135.96
60	10.97	−135.73
80	14.66	−135.50
100	18.38	−135.28
120	22.01	−142.59
140	25.90	−147.71
150	27.91	−149.7
160	26.60	−19.17
180	22.67	−24.09
190	20.79	−27.27
200	18.98	−31.09
220	15.19	−30.79
240	11.4	−30.49
250	9.5	−30.34
260	7.6	−30.19
280	3.8	−29.89
300	0.00	148.16

Table C.6 Phasor values of I_{tw} at selected distances (TPAO, SC at 150km)

Distance [km]	$\lvert \boldsymbol{I_{tw}} \rvert$ **[A]**	$\angle \boldsymbol{I_{tw}}$ **[deg]**
0.00	58.93	−42.78
0.80	36.25	−58.38
1.60	22.29	−73.97
2.40	13.69	−89.56
2.80	10.72	−97.37
3.60	6.57	−113.02
4.40	4.02	−128.79
5.60	1.91	−152.96
6.80	0.91	−178.50
8.00	0.44	153.31
10.00	0.17	101.07
12.00	0.10	62.73
$\vdots$	≈ 0	–
146.80	0.51	−0.08
147.60	0.82	12.34
148.40	1.30	26.15
149.20	2.08	40.84
150.00	3.34	56.07
150.80	2.08	40.84
151.60	1.30	26.14
152.40	0.82	12.32
153.20	0.51	−0.11

Distance [km]	$\|\boldsymbol{I_{tw}}\|$ **[A]**	$\angle \boldsymbol{I_{tw}}$ **[deg]**
154.00	0.32	−10.41
⋮	≈ 0	–
288.00	0.03	49.02
290.00	0.08	−62.63
292.00	0.38	−43.67
293.20	0.81	−25.01
294.40	1.69	−4.04
295.60	3.48	18.26
296.40	5.63	33.55
297.20	9.11	49.01
297.60	11.59	56.79
298.40	18.80	72.39
299.20	30.50	88.02
300.00	49.52	103.67

Table C.7 Phasors of I_a and I_b at various distances (OPAO, No SC)

Distance [km]	$\|\boldsymbol{I_a}\|$ **[A]**	$\angle \boldsymbol{I_a}$ **[deg]**	$\|\boldsymbol{I_b}\|$ **[A]**	$\angle \boldsymbol{I_b}$ **[deg]**
0.00	0.00	0.00	0.00	0.00
20.00	1.84	−40.35	0.98	112.47
40.00	3.66	−41.15	1.96	113.85
50.00	4.56	−41.55	2.45	114.54
60.00	5.45	−41.95	2.94	115.23
80.00	7.22	−42.74	3.91	116.61
100.00	8.96	−43.52	4.89	117.98

Distance [km]	$\|\boldsymbol{I}_a\|$ **[A]**	$\angle \boldsymbol{I}_a$ **[deg]**	$\|\boldsymbol{I}_b\|$ **[A]**	$\angle \boldsymbol{I}_b$ **[deg]**
110.00	8.47	−42.73	4.05	115.30
120.00	7.98	−41.91	3.22	111.44
140.00	6.98	−40.17	1.66	93.74
150.00	6.47	−39.22	1.06	67.48
160.00	5.95	−38.19	0.96	18.41
180.00	4.91	−35.80	2.15	−29.52
190.00	4.38	−34.34	2.92	−36.76
200.00	3.85	−32.59	3.70	−41.11
220.00	3.16	−31.43	3.03	−39.68
240.00	2.44	−30.36	2.33	−38.36
250.00	2.06	−29.86	1.97	−37.74
260.00	1.67	−29.38	1.59	−37.13
280.00	0.86	−28.49	0.82	−36.00
300.00	0.00	25.53	0.00	24.27

Table C.8 Phasor values of I_a and I_b at various distances (OPAO, SC at 150km)

Distance [km]	$\|\boldsymbol{I}_a\|$ **[A]**	$\angle \boldsymbol{I}_a$ **[deg]**	$\|\boldsymbol{I}_b\|$ **[A]**	$\angle \boldsymbol{I}_b$ **[deg]**
0.00	0.00	0.00	0.00	0.00
20.00	1.56	108.71	4.41	123.37
40.00	3.10	109.73	8.81	123.68
50.00	3.87	110.26	11.02	123.84
60.00	4.64	110.78	13.22	124.00
80.00	6.18	111.83	17.62	124.30
100.00	7.71	112.88	22.02	124.61

Distance [km]	$\|\boldsymbol{I}_a\|$ **[A]**	$\angle\boldsymbol{I}_a$ **[deg]**	$\|\boldsymbol{I}_b\|$ **[A]**	$\angle\boldsymbol{I}_b$ **[deg]**
110.00	9.88	115.59	22.78	124.52
120.00	12.06	117.38	23.54	124.47
140.00	16.44	119.65	25.07	124.48
150.00	18.64	120.44	25.83	124.52
160.00	32.02	-51.27	26.25	-51.66
180.00	27.56	-50.99	24.68	-51.64
190.00	25.32	-50.84	23.88	-51.66
200.00	23.07	-50.69	23.08	-51.72
220.00	18.53	-50.44	18.53	-51.46
240.00	13.96	-50.19	13.96	-51.20
250.00	11.65	-50.08	11.65	-51.08
260.00	9.34	-49.96	9.34	-50.96
280.00	4.69	-49.72	4.69	-50.71
300.00	0.00	-75.54	0.00	-78.55

Table C.9 Phasor values of I_{tw} at selected distances (OPAO)

Distance [km]	$\|\boldsymbol{I}_{tw}\|$ **[A]**	$\angle\boldsymbol{I}_{tw}$ **[deg]**
0.00	78.89	-106.90
0.80	48.53	-122.51
1.60	29.84	-138.13
2.40	18.33	-153.75
2.80	14.37	-161.57
3.60	8.81	-177.27
4.40	5.40	166.92

Distance [km]	$\lvert \boldsymbol{I_{tw}} \rvert$ **[A]**	$\angle \boldsymbol{I_{tw}}$ **[deg]**
5.60	2.59	142.74
6.80	1.24	117.50
8.00	0.61	90.50
10.00	0.23	43.31
12.00	0.12	8.61
⋮	≈ 0	–
146.00	0.61	-76.14
146.80	1.00	-63.26
147.60	1.61	-49.29
148.40	2.59	-34.59
149.20	4.18	-19.43
150.00	6.76	-4.01
150.80	4.18	-19.43
151.60	2.59	-34.60
152.40	1.61	-49.30
153.20	1.00	-63.29
154.00	0.62	-76.18
⋮	≈ 0	–
288.00	0.01	-71.72
290.00	0.13	-133.00
292.00	0.54	-107.04
293.20	1.14	-86.91
294.40	2.35	-65.09
295.60	4.84	-42.34

Distance [km]	$\lvert I_{tw} \rvert$ [A]	$\angle I_{tw}$ [deg]
296.40	7.83	-26.90
297.20	12.69	-11.35
297.60	16.16	-3.55
298.40	26.22	12.08
299.20	42.56	27.72
300.00	69.13	43.36

Table C.10 Conductor parameters used in the simulation model

No.	D_{out}[cm]	T/D_{out}	r_{dc} [Ω/km]	μ_r	N_c	D_b[cm]
1	2.5200	0.3530	0.0870	1	3	46.1880
2	1.1780	0.2009	0.5090	1	1	0

Table C.11 Phasor values of V_{tw} along the line (OPAO, $k_{id}^{+} = 1$, SC at 150 km)

Distance [km]	$\lvert V_{tw} \rvert$ [V]	$\angle V_{tw}$ [deg]
0.00	725.74	180
0.80	408.88	180
1.60	251.57	180
2.40	153.38	180
3.20	92.90	180
4.00	56.20	180
4.40	43.65	180
4.80	33.92	180
5.20	26.28	180

Distance [km]	$\lvert \boldsymbol{V_{tw}} \rvert$ **[V]**	$\angle \boldsymbol{V_{tw}}$ **[deg]**
5.60	20.46	180
6.00	15.87	180
6.40	12.35	180
6.80	9.55	180
7.20	7.45	180
7.60	5.93	0
8.00	4.70	0
10.00	1.75	0
⋮	≈ 0	–
146.00	3.02	180
146.80	5.66	0
147.60	11.59	0
148.40	25.88	0
149.20	66.55	0
150.00	196.37	0
150.80	66.55	0
151.60	25.88	0
152.40	11.58	0
153.20	5.67	0
154.00	3.02	180
⋮	≈ 0	–
290.00	1.33	180
292.00	4.26	180
292.40	5.46	180

Distance [km]	$\lvert \boldsymbol{V_{tw}} \rvert$ **[V]**	$\angle \boldsymbol{V_{tw}}$ **[deg]**
292.80	6.94	180
293.20	8.77	180
293.60	11.06	180
294.00	13.83	180
294.40	17.53	180
294.80	22.16	180
295.20	27.94	180
295.60	35.03	180
296.00	44.15	180
296.80	70.82	180
297.60	116.31	180
298.40	191.33	180
299.20	313.80	180
300.00	539.52	180